Phenomenological and Semi-phenomenological Models of Nano-particles Freezing

A Thesis Submitted to the
College of Graduate Studies and Research
in Partial Fulfillment of the Requirements
for the degree of Master of Science
in the Department of Chemistry
University of Saskatchewan
Saskatoon

By
Cletus Asuquo

Permission to Use

In presenting this thesis in partial fulfilment of the requirements for a Postgraduate degree from the University of Saskatchewan, I agree that the Libraries of this University may make it freely available for inspection. I further agree that permission for copying of this thesis in any manner, in whole or in part, for scholarly purposes may be granted by the professor or professors who supervised my thesis work or, in their absence, by the Head of the Department or the Dean of the College in which my thesis work was done. It is understood that any copying or publication or use of this thesis or parts thereof for financial gain shall not be allowed without my written permission. It is also understood that due recognition shall be given to me and to the University of Saskatchewan in any scholarly use which may be made of any material in my thesis.

Requests for permission to copy or to make other use of material in this thesis in whole or part should be addressed to:

Head of the Department of Chemistry
110 Science Place
University of Saskatchewan
Saskatoon, Saskatchewan
Canada
S7N 5C9

Abstract

Studies of nucleation in freezing nanoparticles usually assume that the embryo of the solid phase is completely wet by the liquid and forms in the core of the droplet. However, recent experiments and computer simulations have suggested that some nanoparticles start nucleating at the liquid-vapor interface of the drop in a pseudoheterogeneous process. The goal of the present work is to propose phenomenological models suitable for the study of surface nucleation in nanoparticle systems that can be used to understand the contributions of the various surface phenomena, such as surface and line tensions, to the nucleation barrier.

The nucleation barrier for the freezing of a 276 atom gold cluster is calculated using Monte Carlo simulation techniques while previous simulation studies of a 456 atom gold cluster are extended in order to find the probability that the embryo forms in the surface or core of the nanoparticle. These calculations confirm that the crystal embryo forms at the liquid-vapor interface. Geometric studies measuring the liquid-solid and solid-vapor surface areas of the embryo suggest that it changes shape as it becomes larger and grows in towards the core of the droplet.

Three phenomenological models that are based on the capillarity approximation and can account for surface nucleation are proposed. These models highlight the importance of accounting for the surface curvature contributions related to the Tolman length and the presence of the three phase contact line in calculating the nucleation free energy barrier. In some cases, the models are able to reproduce the qualitative properties of the free energy barriers obtain from simulation but numerical fits of the models generally result in estimates of the solid-liquid surface tension that are lower than the values expected on the basis of partial wetting in the bulk.

Finally, a semi-phenomenological model approach to nucleation is proposed where the usual phenomenological expression for the free energy barrier is retained, but where the geometric prefactors are obtained from molecular simulation of the embryo. This method is applied to nucleation in the gold cluster and to the freezing of a bulk Lennard-Jones liquid.

Acknowledgements

My utmost thanks go to Dr. R. K. Bowles for offering me a position in his group. I really appreciate him for his scientific and non-scientific advice, his patience in mentoring. I wish to thank members of my academic advisory committee for their dedication to see this thesis come true.

I would like to thank all members of Dr. Bowles group, past and present, especially Dr. S. S. Ashwin, Levent Inci and Eduardo Mendez for their friendship, brilliant ideas and useful discussions.

I thank Akwa Ibom State University of Technology (AKUTECH), for sponsoring my graduate studies.

Special thanks go my parent and siblings for their love and support till this stage of my studies.

To many whose names have not been mentioned yet have been of immense assistance to me during my M.Sc, I say thank you so much.

This thesis is dedicated to my teachers past and present, and to all my students.

Contents

List of Tables

List of Figures

List of Symbols

n	Embryo size
n*	Critical embryo size
n_{max}	Largest embryo sizein a cluster
ν_s	Volume per solidlike atom
ν_l	Volume per liquidlike atom
ρ	Density of embryo
N	Total number of atoms in a cluster
μ	Chemical potential
$\Delta\mu$	Change in chemical potential
J	Rate of nucleation
k_B	Boltzmann constant
T_m	Melting temperature
n_0	Umbrella center
κ	Umbrella constant
ϕ	Umbrella bias potential
ΔG	Change in Gibbs free energy
ΔG^*	Height of free energy barrier
r_{cut}	Cut-off radius for Voronoi construction
r_c	Probe radius for cone algorithm
r_b	Neighboring distance
C_{min}	Minimum dot product threshold
$C_x N_T$	Threshold ratio of connection per neighbor
q_i	Six dimensional Q6 for particle i
c_{ij}	Dot product between particles i and j
A_{ab}	Surface area between phases a and b
L_{svl}	Length of three phase contact line
σ_{ab}	Surface tension between phases a and b (with units energy per area)
τ	Line tension (with units energy per length)
δ	Tolman length (surface curvature correction)
α	Contact angle
α_{min}	Contact angle at minimum free energy barrier
d	Distance between embryo and center of mass of cluster
d_{min}	Minimum distance between embryo and center of mass of cluster
d_{max}	Maximum distance between embryo and center of mass of cluster
V	Vector for the Voronoi vertices

Chapter 1

Introduction

The study of nanoparticles is increasing enormously due to the scientific and technological potentials of nanosystems. The enhancement of many physical, chemical and mechanical properties of materials with the reduction in their size is the center of nanoscience. The production of these nano-materials demands accurate control over the processes involved in their production such as condensation and crystallization. A major method of production of nanoparticles begins with a crucial mechanism of formation of an embryo or nucleus[1] of the new phase within the metastable phase[2]. This fundamental mechanism is termed nucleation[2, 3]. The properties of the nanoparticles, for example, catalytic, optical, semiconducting, and superconducting properties and the processes involving them, such as the freezing of nitric acid, HNO_3, into nitric acid trihydrate, NAT, and nitric acid dihydrate, NAD[4] in the atmosphere, are greatly affected by the rate of nucleation during their formation.

The properties of a bulk uniform phase are translationally invariant so that the work of forming an embryo of a new phase within the metastable mother phase is independent of the embryo's location. However, the presence of a liquid-vapour interface in a liquid droplet introduces a non-uniform density distribution which can dramatically affect how a crystal nuclei may form. For example, Tabazadeh et al[4] found that the agreement between data from a number of different studies of freezing rates of nitric acid dihydrate (NAD) and nitic acid trihydrate (NAT), improved dramatically when the model included the possibility that freezing was initiated at the surface of the drop, rather than in the core. They also showed, using a simple capillarity based model[5], that nucleation initiated at the liquid-vapor interface exhibited a lower free energy barrier compared to core (volume) based nucleation which was sufficient to lead to changes in the nucleation rate of several

orders of magnitude. Recent studies of freezing in gold nanoparticles[6, 7] show that nucleation occurs at the surface. Nanoparticles of SeF6 show a strong tendency for surface nucleation at deep supercooling[8], but Lennard-lones liquid particles[9, 10] appear to freeze from the core.

The main goal of the current thesis is to use simple phenomenological models and a semi-phenomenological model to study surface nucleation and its content is organized as follows:

In the first chapter, we discuss the fundamentals of phase transitions and nucleation theories. We begin this chapter with the discussion of the stability criteria for thermodynamic systems. The different approaches to nucleation are discussed in section 1.2. These include the kinetic, thermodynamic, phenomenological and molecular approaches to nucleation. In section 1.3, we discuss the different forms of nucleation encountered in nature with some of their industrial applications, while freezing in nanosystems is the subject of section 1.4. Section 1.5 introduces the phenomenon of surface nucleation as observed in some nanoclusters and the chapter is concluded with the scope of the thesis.

In Chapter 2, the free energy barriers to nucleation of gold nanoparticles are calculated using Monte Carlo simulations techniques. Chapter 3 describes simple phenomenological models used to study surface nucleation while a semi-phenomenological model is proposed for the study of nucleation in gold nanoparticles and Lennard-Jones bulk liquid in Chapter 4. Chapter 5 discusses the performances of the different phenomenological and the semi-phenomenological models with respect to the nanoclusters studied.

1.1 Stability, Metastability and Phase Transition

The thermodynamic stability of a system can be examined by considering how the thermodynamic state functions, such as entropy and internal energy, respond to variations away from a given state point. A thermodynamic system is said to be isolated when it cannot interact with its environment, so it is unable to exchange mass, heat or do work with the surrounding. The second law of thermodynamics postulates that the entropy increases for any spontaneous process in an isolated

system. The entropy must then be at a maximum when the system is at equilibrium and all spontaneous processes have stopped. This can be expressed symbolically as,

$$[\Delta S]_{U,V,N} \leq 0, \tag{1.1}$$

where S, U, V and N are the entropy, internal energy, volume and number of moles (mass) of the system respectively. In terms of the internal energy of the system, the above condition becomes,

$$[\Delta U]_{S,V,N} \geq 0. \tag{1.2}$$

Expanding the L.H.S of eqn. 1.2 in terms of a Taylor expansion gives the variational changes in the internal energy as,

$$\left[\delta U + \frac{1}{2!}\delta^2 U + \frac{1}{3!}\delta^3 + ...\right]_{S,V,N} \geq 0. \tag{1.3}$$

A stable equilibrium exists with a vanishing linear term and a postive second order term when considering all variations at constant S,V,N:

$$\delta U|_{S,V,N} = 0, \qquad \delta^2 U|_{S,V,N} > 0. \tag{1.4}$$

The limit of stability is reached when both terms equal zero and the system is said to be in a an unstable equilibrium, *i.e.*

$$\delta U\ |_{S,V,N} = 0, \qquad \delta^2 U\ |_{S,V,N} = 0. \tag{1.5}$$

Therefore, the equilibrium criterion is defined by the first order term which must be equal to zero, while the positiveness of the second order differential defines the stability criterion. For a system in stable equilibrium, a small fluctuation will return the system back to the minimum in internal energy whereas for an unstable system, any small fluctuation drives the system away from the equilibrium position. In terms of the intensive and extensive thermodynmic variables, we write the internal energy (fundamental equation) of a fluid at constant temperature, T, pressure, p, and chemical potential, μ, from Gibbs-Duhem relations as

$$dU = TdS - pdV + \mu dN. \tag{1.6}$$

For an n-component mixture, eqn. 1.6 becomes

$$dU = TdS - pdV + \sum_{j=1}^{n} \mu_j dN_j. \tag{1.7}$$

Since the internal energy and the entropy are not easily controlled experimental variables, there is a need for an alternative way of stating the stability criteria of the system. These are:

$$[\Delta F]_{T,V,N} \geq 0, \tag{1.8}$$

$$[\Delta G]_{T,p,N} \geq 0, \tag{1.9}$$

where the F is the Helmholtz free energy defined as

$$F = U - TS, \tag{1.10}$$

and G, the Gibbs free energy is

$$G = U - TS + pV. \tag{1.11}$$

The inequalities 1.1, 1.2, 1.8 and 1.9 are basically equivalent[11] as they all refer to the fact that any spontaneous process undergone by a closed system is accompanied by an increase in the entropy of the system.

Equations 1.6 and 1.7 can be cast as

$$dU = \sum_{j=1}^{n+2} Y_j dX_j, \tag{1.12}$$

where X represents the natural independent variables of entropy, volume, and number of molecules, *i.e*, $X = \{S, V, N\}$, and Y the corresponding conjugate intensive variables, *i.e*, $Y = \{T, -p, \mu_i (i = 1, 2...n)\}$. By taking partial derivatives, the conjugate intensive variables can be obtained,

$$Y_j = \left(\frac{\partial U}{\partial X_j}\right)_{X_1, X_2..., X_{j-1}, X_{j+1}...X_{n+2}}. \tag{1.13}$$

The expression on the right of eqn. 1.4 can be written as

$$\left(\frac{\partial Y_{n+1}}{\partial X_{n+1}}\right)_{Y_1, Y_2..., Y_n, X_{n+2}} > 0. \tag{1.14}$$

A system that satisfies eqn. 1.14 is considered to be stable. Once the limit of stability is reach or exceeded, we have

$$\left(\frac{\partial Y_{n+1}}{\partial X_{n+1}}\right)_{Y_1, Y_2..., Y_n, X_{n+2}} = 0, \tag{1.15}$$

and the system undergoes a phase transition in order to lower its free energy.

The stability criteria described here were obtained by considering small variations around an equilibrium point. The global stability of a system is determined by considering the relative free energy of various phases. The phase with the lowest Gibbs free energy at a given T,P,N, is the most stable phase. See fig. 1.1. Below the equilibrium transition (freezing and condensation) temperature, though the homogenous phase still exist, it is no longer the most stable state [11], and the system is said to be in metastable equilibrium. This phase is only stable to local fluctuation and corresponds to a local minimum in the free energy that is separated from the global minimum by a barrier [7]. This metastable phase is illustrated by the arms AD, BF, and FC in fig. 1.1.

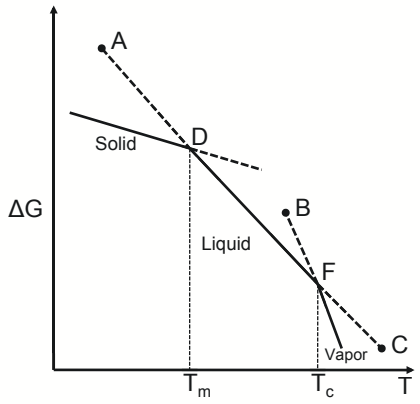

Figure 1.1: A diagram showing the free energy as a function of temperature and depicting regions of metastability.

Large fluctuations cause the metastable phase to overcome a barrier (nucleation barrier) and goes to the more stable state - global minimum, by freezing, condensation or evaporation. In fig. 1.1, A, B and C correspond to different spinodals, where the thermodynamic stability requirement of positive isothermal compressibility is first violated, i.e $\kappa = -1/V \left(\frac{dV}{dP}\right)_T < 0$. Beyond these points, there is no barrier separating the local and global minima. Points B and C have been observed experimentally[12], but the existence of A which corresponds to the spinodal in the low temperature region for liquids is still an open question. Though a metastable liquid may persist for sometime, there is always a finite lifetime of a metastable

phase. The rate at which the metastable system transforms to the more stable solid phase is determined by nucleation kinetics.

1.2 Nucleation

1.2.1 Kinetics

Kinetically, to describe the appearance of an embryo in a new phase, we consider it as the addition of two monomers to form a dimer[11]. Continuous addition and removal to this dimer results in fluctuations . As a molecule or atom is added, the embryo grows, but it then shrinks when a molecule or atom is lost. Therefore, the description of the change in the population of an embryo of a given size, n, at time, t may be written as

$$\frac{\partial f(n,t)}{\partial t} = \beta_{n-1} f(n-1,t) + \alpha_{n+1} f(n+1,t) - \beta_n f(n,t) - \alpha_n f(n,t), \tag{1.16}$$

where $f(n,t)$ is the number density of embryos having n-monomers at time t, while β_n and α_n are the rates at which $n-sized$ embryo gains or looses monomers respectively. This can be rewritten as

$$\frac{\partial f(n,t)}{\partial t} = J(n+1,t) - J(n,t), \tag{1.17}$$

where

$$J(n) = \beta_n f(n,t) - \alpha_{n+1} f(n+1,t), \tag{1.18}$$

represents the resultant rate at which embryos of size n become embryos of size $n+1$ at time t.

The value of the constant β_n for the attachment of a monomer is often obtained through kinetic theory of gases, but the value of the rate constant for the detachment, α_n, is not easily obtained independently. By using the *constrained equilibrium hypothesis* which states that the embryos evolving from the metastable phase cannot grow beyond a certain limiting size, and assuming microscopic reversibility at equilibrium, the net rate must be zero and eqn. 1.18 becomes

$$J(n) = \beta_n f_{eq}(n) - \alpha_{n+1} f_{eq}(n+1) = 0, \tag{1.19}$$

where the equilibrium distribution of $n - sized$ embryos, $f_{eq}(n)$, has replaced the non-equilibrium distribution. Solving for α_{n+1} in eqn. 1.19 gives

$$\alpha_{n+1} = \frac{f_{eq}(n)\beta_n}{f_{eq}(n+1)}. \tag{1.20}$$

Putting this back in eqn. 1.18 yields

$$J(n) = \beta_n f_{eq}(n) \left[\frac{f(n,t)}{f_{eq}(n)} - \frac{f(n+1,t)}{f_{eq}(n+1)} \right]. \tag{1.21}$$

Classical Nucleation Theory (CNT), assumes steady state conditions, where the distributions of clusters of different sizes is independent of time. This results in $\partial f(n,t)/\partial t = 0$, and the flux is not dependent on the cluster size, $i.e, J(n) = J$. Performing a recurrent summation over all embryo sizes present, eqn. 1.21, the total steady state nucleation rate is

$$J = N_{tot} \left[\sum_{n_{min}}^{n_{max}} \frac{1}{\beta_n f_{eq}(n)} \right]^{-1}, \tag{1.22}$$

where N_{tot} is the total number density of embryos and the limits of the sum are taken from the smallest embryo size, n_{min} to the the largest embryo in the cluster, n_{max}, and are such that for $n \geq n_{min}$, $f(n) = f_{eq}(n)$ and for $n > n_{max}$, $f(n) = 0$.

The equilibrium embryo size distribution, $f_{eq}(n)$, is obtained directly from the theory of thermodynamic fluctuation[11],

$$f_{eq}(n) = f_{eq}(0) \exp\left(\frac{-\Delta G(n)}{k_B T} \right), \tag{1.23}$$

where $G(n)$ is the free energy required to form an $n - sized$ embryo from monomers, k_B is the Boltzmann constant and T is the temperature. Replacing the summation in eqn. 1.22 by an integral and using eqn. 1.23 yields

$$J \simeq N_{tot} \left[\int_{n=n_{min}}^{n_{max}} \frac{1}{\beta_n f_{eq}(1)} \exp\left(\frac{\Delta G(n)}{k_B T} \right) dn \right]^{-1}. \tag{1.24}$$

When the free energy barrier is high, eqn. 1.24 may be approximated by the steepest descent approximation in which the major contribution to the integral comes from values centered around the location of the critical size of the embryo, n^*, which occurs at the maximum. Approximating the free energy around the location of the

critical embryo, we obtain

$$\Delta G(n) \approx \Delta G(n^*) + \frac{1}{2}\frac{d^2\Delta G(n)}{dn^2}\mid_{n^*}(n-n^*)^2. \tag{1.25}$$

The nucleation rate can now be written as,

$$J \approx \beta_{n*} f_{eq}(1)\exp\left(\frac{\Delta G(n^*)}{k_B T}\right)\left[\int_0^\infty \exp(\frac{\frac{1}{2}\frac{d^2\Delta G(n)}{dn^2}\mid_{n^*}(n-n^*)^2}{2k_B T})dn\right]^{-1}. \tag{1.26}$$

Evaluating the integral in eqn. 1.26 yields the Zeldovich factor[13],

$$Z = \sqrt{\frac{\frac{-\partial^2\Delta G}{\partial n^2}\mid_{n^*}}{2\pi k_B T}}, \tag{1.27}$$

and this results in the final form of the nucleation rate being given as

$$J_{CNT} = \beta_{n^*} Z N_{tot}\exp\left(-\frac{\Delta G(n^*)}{k_B T}\right). \tag{1.28}$$

Due to lack of the knowledge of α_n and under the assumption of detailed balance, the calculation of the nucleation rate turns into a thermodynamics problem of calculating the equilibrium embryo distribution. In calculating the nucleation rate given by eqn. 1.28, two basic assumptions of CNT were invoked. First, that the steady state is quickly reached. Though this is basically true, in some cases involving crystallization of complex systems the lag time in reaching a steady state can be as large as the time for the measurement[11]. Secondly, the need for high barrier means that CNT is useful only in the region where the system is mildly metastable and may become unreliable with increase in the degree of metastability where the barrier is lower. Due to the limitation of CNT revealed by experiments, there is a search for suitable models which can explain free energies and thus nucleation rate with a high precision.

1.2.2 Thermodynamics

The initial detailed description of the phenomenon of nucleation was given by Gibbs[14]. His description has that the nuclei formed in the volume of a metastable phase have the same properties as the bulk phase of the new stable phase that is being formed and possess a sharp interface between the stable and metastable phases. This method

treats microscopic nuclei with macroscopic thermodynamic variables and this is referred to as the capillarity approximation. In what follows, we obtain the expression for the Gibbs free energy of forming the nuclei assuming that the capillarity approximation is valid.

Considering the formation of a liquid embryo in the bulk of a vapor phase, the surface free energy of the liquid is equal to the bulk surface tension, which is the free energy cost of creating the liquid-vapor interface. This surface tension is isotropic and leads to a spherical equilibrium shape of the small liquid embryo. The thermodynamics of an embryo formation can be derived using the Gibbs droplet model[11, 15, 16], in which the energy cost of creating an interface in a cluster has been included in the internal energy expression as shown in section 1.1. The minimum work of formation of an $n - sized$ embryo in an isothermal process is given as:

$$\Delta G_{min} = \sigma A + (P - P')\nu' + n[\mu'(T, P') - \mu(T, P)], \tag{1.29}$$

where σ is the surface tension, A is the interfacial area between the embryo and the mother phase, $P - P'$ is the difference in pressures between the bulk phase pressure P and the pressure inside the embryo P', ν' is the volume per particle of the liquid embryo, μ' and μ are the chemical potentials in the liquid and vapor phases respectively.

For a liquid droplet away from the critical point, which may be considered as incompressible, we can write:

$$\mu'(T, P') - \mu'(T, P) = \nu'(P' - P). \tag{1.30}$$

Here, ν' is the volume per molecule in the liquid phase. Eqn. 1.29 becomes

$$\begin{aligned} \Delta G_{min} &= \sigma A + n\left[\mu'(T, P) - \mu(T, P)\right] \\ &= \sigma A + n\Delta\mu, \end{aligned} \tag{1.31}$$

where $\Delta\mu$ is the change in chemical potential between the stable phase and the metastable phase. Eqn. 1.31 is the free energy as a function of size, $i.e$

$$\Delta G(n) = \sigma A + n\Delta\mu, \tag{1.32}$$

According to the capillarity approximation, the evolving liquid embryo is spherical, therefore the area, $A = 4\pi r^2$, and eqn. 1.32 becomes,

$$\Delta G(r) = n\Delta\mu + 4\pi r^2\sigma. \tag{1.33}$$

Therefore, to express this free energy with respect to the radius of the embryo, r, we use the relationship between density, ρ, volume, V and the number of molecules, n, inside the embryo, $n = \rho V$ and the free energy becomes,

$$\Delta G(r) = \frac{4}{3}\pi r^3\rho\Delta\mu + 4\pi r^2\sigma. \tag{1.34}$$

Thus in the simplest case of a droplet formation in vapor, ΔG consists of two opposing terms: a volume term $\frac{4}{3}\pi r^3\rho\Delta\mu$, which is negative and favors the formation of the stable liquid phase and a positive surface term which opposes the formation of the new phase, (see fig. 1.2).

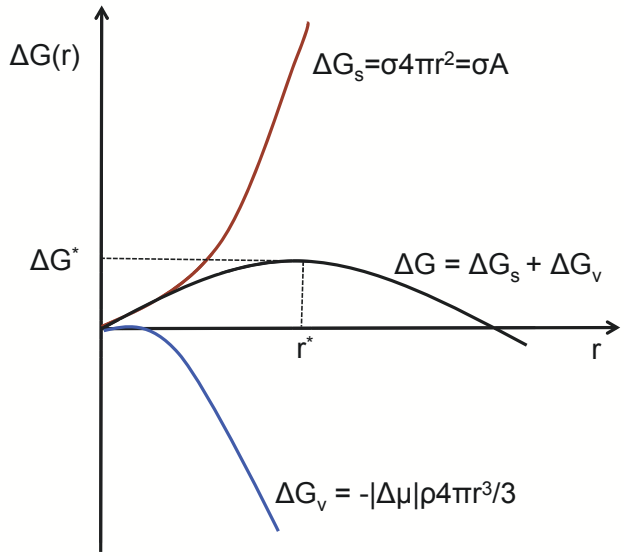

Figure 1.2: Contributions of the surface and volume terms to the Gibbs free energy as a function of droplet radius. r^* is the critical radius beyond which the embryo grows indefinitely.

The critical free energy, ΔG_{crit}, is the maximum free energy change, and the embryo size corresponding to this maximum energy is the critcal size n^* which is obtained from the condition, $\frac{\partial\Delta G(n)}{\partial n} = 0$. In terms of the embryo radius, the critical radius, r^*, is obtained from $\frac{\partial\Delta G(r)}{\partial r} = 0$. Embryos smaller than the critical size

disintegrate into the metastable phase, while those larger than the critical size grow spontaneously to form the new stable phase due to the reduction in the free energy as shown in fig. 1.3. The critical embryo size is therefore at an unstable equilibrium.

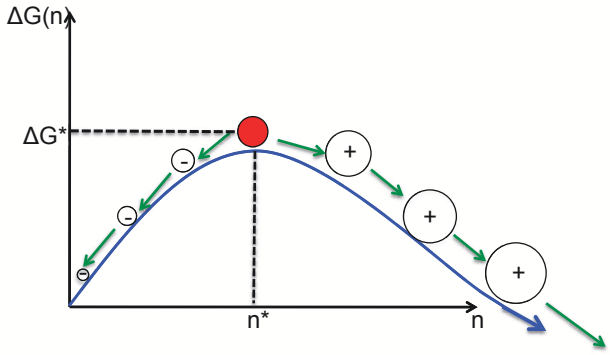

Figure 1.3: A vapor-liquid transition in the bulk phase showing a decomposition of embryos smaller than n^*, while embryo larger than n^* grow spontaneously.

1.2.3 Phenomenological Approach to Nucleation

Phenomenological theories pursue the expression for the work of formation of a cluster based on the capillarity approximation. For a crystal nuclei evolving from the liquid phase, the surface tensions are not necessarily isotropic, and eqn. 1.31 takes the form:

$$\Delta G_{min} = \sum_i \sigma_i A_i(n_i) + n\Delta\mu, \tag{1.35}$$

where A_i is the surface area of the different facets making the crystal and σ_i is the surface free energy per unit area of the facets. The above expression (eqn. 1.35) is a general expression for homogeneous nucleation in the bulk phase,(see fig. 1.4a). For a heterogeneous or "pseudoheterogeneous"[5] nucleation, we consider the crytallization taking place at an interface and therefore the need for additional free energy terms. An example is when the embryo forms at the liquid-vapor interface(see fig. 1.4b), where eqn. 1.35 becomes:

$$\Delta G_{min} = \sum_i \sigma_i^{cl} A_i^{cl} + A^{cv}\left(\sigma^{cv} - \sigma^{lv}\right) - n\Delta\mu, \tag{1.36}$$

where σ_i^{cl} is the crystal-vapor free energy per unit area for the facet i, with the surface area A_i^{cl}, σ^{cv} and σ^{lv} are the crystal-vapor and liquid-vapor surface free

energy respectively.

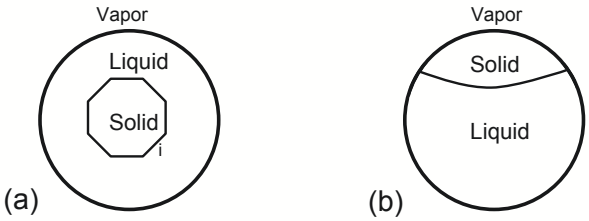

Figure 1.4: A diagram showing different positions at which the embryo can grow during a homogeneous nucleation.

The equilibrium shape of a solid embryo can be determined using Wulff's construction[17]. This approach minimizes the free energy by changing the shape of the crystallite and replacing the surfaces associated with high energy facets with low energy facets. But in practice it is easier to assume that the evolving crystal is spherically symmetric for most systems. This assumption is one of the assumptions of the capillarity approximation. The validity of this assumption is based on the idea that a sphere has the smallest surface area per unit volume, but this can be questionable when considering packing effects at a microscopic level. Recent work on sodium chloride, $NaCl$, have highlighted the need to deal with facets effects in some cases[18], nonetheless, these facet effects are not considered in the present work.

In terms of the number of atoms present in the embryo or the radius of the embryo, the work of formation of the embryo can be written:

$$\Delta G(n) = an^{2/3} - bn, \qquad \Delta G(r) = cr^2 - dr^3 \tag{1.37}$$

where a, b, c, d are constants, $n^{2/3}$ is the surface term and n is the volume contribution to the free energy, r^2 is the surface contribution in terms of the radius while r^3 is the volume term. When the free energy is at maximum, $i.e$ $\frac{\partial \Delta G}{\partial n} \mid_{n^*} = 0$,the critical size, n^*, is given as:

$$n^* = \left(\frac{2a}{3b}\right)^3 = \frac{32\pi}{3}\left[\frac{(\nu')^{2/3}\sigma}{-\Delta\mu}\right]^3, \tag{1.38}$$

where the expression on the right of eqn. 1.38 is for a spherical embryo. In terms of the r, the critical radius is:

$$r^* = \frac{2c}{3d} = \frac{2\sigma\nu'}{-\Delta\mu}. \tag{1.39}$$

The free energy barrier for the formation of $n^* - sized$ embryo, that is spherical is given by

$$\Delta G^* = \frac{4a^3}{27b^3} = \frac{16\pi}{3}\left[\frac{\nu'\sigma^3}{-\Delta\mu}\right]^2. \tag{1.40}$$

The free energy barrier of formation of the critical embryo decreases as $(-\Delta\mu)^2$ while the critical size n^* decreases as $(-\Delta\mu)^3$ showing that as the degree of metastability increases, the critical embryo gets smaller and the barrier gets lower.

Whether the model is homogeneous or heterogeneous, the system must overcome a free energy barrier forming the critical nucleus after which the crystal grows spontaneously.

1.2.4 Molecular Approach to Nucleation

Molecular theories of nucleation are bottom to top approaches which aim at obtaining the nucleation rate starting from the potential energy of interaction between molecules. One approach employs molecular simulation to evaluate the properties of isolated clusters, such as the free energy change during the formation of the cluster, which is used in the estimation of the rate of nucleation[1, 19]. A second approach involves the direct calculation of the rate constant using the variational transition state theory[20] to calculate the relevant dynamical quantities rather than relying on equilibrium properties of the cluster.

A common feature for both of these approaches is the need to define an embryo base on the local environment of the atoms or molecules involved. The method introduced by Hill[21] identifies a cluster as a group of atoms or molecule whose total energy is negative. This cluster criteria is difficult to implement in practice. The Lee-Barker-Abraham(LBA) cluster[22] consists of n-molecules confined in a rigid sphere of volume, ν, with its center coinciding with the center of mass of the associated molecules. Though the cluster defined by this cluster criterion is stable for intermediate cluster sizes, there is no clear justification for the choice of the volume defining the spherical cell. Stillinger[23] proposed a broad and more widely used definition of a cluster in terms of the conectivity of the atoms /molecules involved. By his definition, two molecules are connected if the distance between them is less than some given maximum distance, r_c. The cluster is then defined by the group of

molecules within a distance r_c of at least one other molecule. In the case of freezing, the initial step is to identify liquid-like and solid-like atoms. Then all the solid-like atoms that are close enough to each other are grouped into a distinct $n - sized$ embryo. Though the criteria for identifying solid-like particles is somewhat arbitrary, they are designed to capture the idea that the local environment around a solid-like atom is ordered and structurally correlated with its neighbors. Steinhardt *et al*[24] introduced an empirical order parameter as a function of spherical harmonics $Y_{lm}(\theta(\hat{r}), \phi(\hat{r}))$ which uses the idea of sensing the symmetry of bond orientation irrespective of the bond lengths. Examples of such an order parameter are Q_4, Q_6, Q_8. The detailed derivation of Q_6 which we use in our calculation is given is section 2.3.2. The properties of the system determines the choice of the order parameter as each parameter has a characteristic signature value that is dependent of the structure. Table 1.1 summarizes the signature values for some periodic crystals. The embryo criteria used in the present work are detailed in section 2.2.2.

Table 1.1: Characteristic values of q_4, q_6, q_8 and the number of connection per cell for system having a BCC, FCC, HCP or Icosahedral structure. Taken from ref.[25]).

Structure	N_{nb}	Q_4	Q_6	Q_8	c_{ij}
ICO(Bulk)	12	0	0.199	-	0.50
ICO(Surface)	6	0	0.207	-	0.50
FCC	12	0.19	0.57	0.40	0.70
BCC	12	0.08	0.54	0.38	-
HCP	12	0.10	0.48	0.32	0.70
SC	6	0.76	0.35	0.72	-
SC	10	0.40	0.02	0.60	-
LIQ	12	0.02	0.03	0.02	0.30

Following the first molecular approach, once an $n - sized$ embryo has been identified, the work required to form the embryo, $W = \Delta G(n)$, is calculated from the probability of its appearance. Landau[13] gave a relationship between the probability of finding a system in a state defined by an order parameter q, and the free

energy as:

$$P(q) = C \exp(-\Delta G(q)/k_B T), \tag{1.41}$$

where $P(q)$ is the probability distribution of the system at the state defined by q, $G(q)$ is the corresponding free energy and C is a constant of proportionality. The change in the free energy (work of formation) in going from state q to q' is

$$\frac{W(q \rightarrow q')}{k_B T} = \frac{G(q) - G(q')}{k_B T} = \ln[\frac{P(q)}{P(q')}]. \tag{1.42}$$

The basic connection between the probability of the appearance of a given state, which in our case is the embryo size and its free energy is given by eqn. 1.41. This forms the basis for a molecular approach to nucleation.

Wolde *et al*[27] defined an intensive Gibbs free energy as

$$\frac{N_{eq}(n)}{N} \approx \frac{P_n}{N} \approx \exp\left(\frac{-\Delta G(n)}{k_B T}\right), \tag{1.43}$$

where $N_{eq}(n)$ is the average number of $n - sized$ embryo, N is the number of atoms or molecules in the entire system, $\Delta G = G(n) - G(0)$ is the free energy change associated with formation of an $n - sized$ embryo within the liquid phase and P_n is the probability of appearance of the embryo of size n. P_n can be obtained from Monte Carlo simulation techniques. It was shown by Reiss *et al*[19] that the approximation on the left of eqn. 1.43 holds only in the case where the formation of embryo is a rare event. They established that

$$P_n = p_n(1) + p_n(2) + p_n(3) + ... \approx p_n(1), \tag{1.44}$$

where $p_n(i)$ is the probability of observing exactly i embryos of size n. If the formation of different embryos is independent, then $p_n(i) = [p_n(1)]^i$, and the higher order terms in eqn. 1.44 can be ignored if the embryo are rare, i.e $P_n(n) << 1$. For similar reasons, the average number of $n - sized$ embryo is

$$N_{eq}(n) = 1p_n(1) + 2p_n(2) + 3p_n(3) + ..., \tag{1.45}$$

and here also, the higher order terms disappear for rare embryos resulting in $N_{eq}(n) \approx P_n$.

Calculating P_n by standard computer simulation seems impossible since their appearance is rare. Therefore, there is a need for an effective computer simulation

technique that captures this event with a good enough statistics to calculate $\Delta G(n)$ accurately. Section 2.1 introduces the biased Monte Carlo and parallel tempering techniques which is used in this work. This molecular approach to calculating free energy of forming a critical embryo through eqn. 1.43 is a well established approach and has been used in many systems including crystallization of hard sphere colloids[26], condensation of argon vapor[27] and crystallization of molten sodium chloride[18].

The major challenge with the molecular approach is the need for a suitable order parameter and cluster criteria. The definition of an embryo is intuitive and requires *a priori* assumptions that may not be correct[25].

1.3 Nucleation in Nature

There are two types of nucleation, homogeneous nucleation and heterogeneous nucleation. Homogeneous nucleation occurs in the bulk of a pure substance and is less common since its occurence is highly dependent on the degree of metastability of the substance. Heterogeneous nucleation takes place in the presence of surfaces, impurities or boundaries. These surfaces and impurities serve as preferential sites for the formation of the new phase with lower energy barrier, thus making heterogeneous nucleation more common in nature than homogeneous nucleation. Nucleation apppears in many forms in nature. Condensation, crystallization and cavitation occuring in simple systems, mixtures and alloys are all good examples of nucleation processes.

Condensation is the formation of liquid droplet from a supercooled or supersaturated vapor caused by fluctuations in density. The nucleation of water droplets or ice crystals in the atmosphere constitute the fundamentals of weather forecasting[28] and the formation of clouds in the presence of aerosols is one of the causes of global warming[28]. By inducing nucleation in the atmosphere, through cloud seeding, precipitation such as rain or snow can be forced to occur.

Crystallization which is the formation of solid crystals from a supersaturated homogeneous solution has many biological and industrial applications. The functionality of protein molecules is dependent on their structure. During protein folding(or protein crystallization), the shape or structure of the critical nucleus influences the

the formation of the secondary and tertiary structure of the protein and hence its functionality[29]. Protein crystallization or aggregation is thought to be a major cause of certain health conditions or diseases such as sickle cell anemia, cataract in the eye[28] and the formation of kidney stones(*uric acid crystals*). In the pharmaceutical industry, the appropriate choice of crystal structure of drugs, which is controlled at the nucleation stage, determines their delivery, bio-availability and effectiveness[28]. Bypassing or controlling ice nucleation is desirable in the area of cryogenics for the preservation of embryos and human tissue[30]. The properties of advance materials such as polymers, ceramics and semi-conductors are also controlled during crystallization.

Cavitation is the formation of vapor bubbles in a flowing liquid under rapid pressure change. This form of nucleation which is mostly heterogeneous, has detrimental consequences in hydraulic systems. Bubbles in the liquid sometimes implode during cavitaion in the liquid-vapor phase transition causing a surge in the pressure which is propagated in the liquid. Cavitation causes erosion in the walls of hydraulic systems[28] such as blades of dam turbines or ship propellers and also reduces the efficiency of these systems. Understanding cavitation nucleation is a major step to evade these negative consequences. Useful applications of cavitaion include ultrasonic machining of tools, ultrasound cleansing and the fabrication of emulsion and droplet.

Understanding the rate and mechanism of nucleation has been the focus of a major research effort in recent years. This is because the rate and mechanism of nucleation from which new materials are formed determines the properties of the materials formed. Therefore controlling the properties of these materials hinges on controlling the rate of nucleation.

1.4 Freezing in Nanoparticles

Computational studies, with the objective of finding the lowest energy structure, have helped in the understanding of the structural transformations during phase transition in nano-systems. Nam *et al*[31, 6] observed that the freezing of gold nanoparticles starts with the ordering of the surface and that the structures with

a fivefold symmetry, such as Icosahedra (Ih) were the most prevalent. They also observed that as the cluster size increases, truncated octahedral ($t-Oh$) and their variants become more prevalent. These different structures have also been observed experimentally in samples of gold clusters synthesized by different methods and analyzed by high electron transmission spectroscopy[32, 33] and high-resolution electron microscopy[34].

Fig. 1.5 left shows the relative energies of different structures with respect to the cub-octahedral arrangement, while the right of fig. 1.5 compares the energies of a series of icosahedral structures.

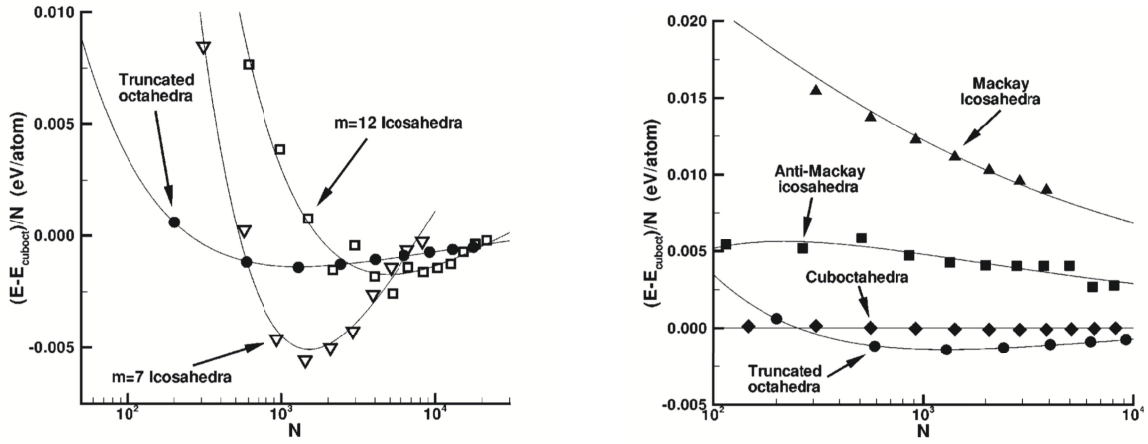

Figure 1.5: Relative energies with respect to cub-octahedral shapes (left) and comparison of total energies per atom for cub-octahedral shapes (right), taken from ref.[36].

Contrary to experimental observations[32, 33, 34], theoretical studies suggest that the Ih structures seen in gold nanoclusters in the range of 100-1000 atoms are energetically metastable[35] with respect to the octahedra structures[36]. The Ih structures are expected to be metastable at large sizes due to the accumulation of energy strain. Some of the Ih structures are formed at some determinate number of atoms known as magic numbers, $i.e$, the plot of total energies against cluster sizes are not perfectly uniform.

It should be noticed that the different structures of a given size have different numbers of surface atoms, therefore surface phenomena may play some important role in the freezing of nanoparticles. The freezing transition observed in molecular dynamics simulations of gold clusters of size about 3000 atoms, for example, show

that different cooling conditions lead to a spontaneous formation of various crystal structures (Ih, Dh, and $t-Oh$) with Ih being the most prevalent structures[37]. Nam *et al*[31] showed that for clusters larger than 450 atoms, $t-Oh$ clusters are more prevalent with other structures still appearing despite the fact that the FCC structure is the most stable structure for the particle sizes under consideration. During a real-time microscopic studies[38], it was observed that there are structural changes in gold clusters from a single crystalline form to a twinned crystalline form of Ih or Dh during freezing. Such observations emphasize the fact that aside from thermodynamics, kinetic factors play an important role in determining the crystalline structure into which a cluster freezes.

1.5 Surface versus Bulk Nucleation

Computer simulations and experimental analyses have shown that surface phenomena play an important role in the freezing of nanoparticles. In a recent study, the nucleation rates for the freezing of water droplets containing HNO_3 in the stratosphere were compared with the rate from the model provided by the classical nucleation theory, where nucleation is believed to start from the bulk(cf. fig. 1.4a). There was a better correlation between experiment and the model suggesting surface nucleation[4]. The freezing of aqueous HNO_3 droplets into nitric acid trihydrate (NAT) and nitric acid dihydrate (NAD)[4], and the differential thermal analysis during the crystallization of molten tin[39] all suggest surface nucleation. A Monte Carlo simulations for the freezing of a 456-atom gold cluster by Mendez *et al*[7] showed that 60% of the solidlike atoms are on the solid-vapor interface for embryo sizes less than 20 atoms, and about 50% for embryo sizes greater than 20 atoms, showing freezing begins at the surface for this system.

Djikaev *et al*[5] used a phenomenological model involving thermodynamic data consistent with capillarity approximation to study "pseudoheterogeneous" nucleation, which involves the solid nucleus forming at the soft 'liquid-vapor' interface (cf. fig. 1.4b). They show that surface nucleation is favored when

$$\sigma_{sv} - \sigma_{lv} < \sigma_{sl}, \tag{1.46}$$

where σ_{sv}, σ_{lv} and σ_{sl} are the solid-vapor, liquid-vapor and solid-liquid surface free energy per unit area respectively. This corresponds to the condition for the liquid phase to partially wet its crystal. For surface nucleation to occur, the interfacial areas and their corresponding surface free energy have some effects on the height and shape of the free energy barrier to nucleation.

1.6 Scope of the Thesis

The purpose of this thesis is to understand the role of surface phenomena on the shape and height of free energy barriers to freezing in nanoparticles. Phenomena such as surface tensions and their corresponding surface areas, line tension, the length of the three phase contact line, the contact angle and finite size effects of the different surface tensions are considered. Our main goal is to develop different phenomenological models depicting surface nucleation to study the effects of these phenomena. A semi-phenomenological model, which uses the basic form of the free energy expression but with geometric factors obtained directly from simulations, is also developed.

In Chapter 2, we use Monte Carlo methods to calculate the free energy barriers to nucleation for 276 atom gold cluster as a function of embryo size. To probe more into surface nucleation, we also calculate the free energy barriers as a function of both size and the distance of the embryo from the center of mass of the whole cluster.

Using the capillarity approximation, we develop three different phenomenological models to study surface nucleation in Chapter 3. The spherical cap model is characterized as a function of embryo size only, whereas the modified spherical cap model also make use of the contact angle in addition to the size. We use the sphere-sphere model as a function of size and distance to study the most favorable position of the nucleating embryo. These models with different corrections applied to them will be fitted to the free energy barriers from Chapter 2.

A major drawback of phenomenological models is that the calculation of the surface areas and other geometric coefficients is based on some idealized geometry. In Chapter 4, we develop a model that calculates these geometric coefficients directly from simulation and is independent of any formal geometry. We use this model to

study surface nucleation as observed in gold nanoparticles, and also crystal nucleation from the Lennard-Jones bulk liquid.

Finally, we summarize the suitability and compare the performances of our different models in Chapter 5. We also discuss some of our findings which constitute the basis for future work.

Chapter 2

Free Energy Barriers to Nucleation

2.1 Introduction

Experimentally, the studies of the liquid-solid phase transition is a formidable challenge due to the difficulty in identifying the critical fluctuations in density and order coupled with the fast rate at which nucleation takes place. However, a recent study using a combination of neutron scattering experiment and Monte Carlo simulations has shown it is possible to determine the critical embryo size using neutron scattering structure factors[40]. Computer simulations provide a useful method since they permit the study of nucleation at the molecular level. Monte Carlo and molecular dynamics simulations techniques are useful in calculating energy barriers to nucleation. In this Chapter, we use Monte Carlo methods to calculate the free energy barrier to freezing for a 276 atom gold cluster. We also calculate the free energy of 456 atom cluster as a function of size and the distance of the embryo from the center of mass of the cluster.

Section 2.2 provides an overview of the MC techniques used in our calculation. Section 2.3 provides the details of the MC implementation used to calculate the free energy barriers, including a description of the interatomic potential and embryo criteria. Our results and discussion are presented is section 2.4.

2.2 Monte Carlo Methods

2.2.1 Importance Sampling

An Importance sampling technique estimates a property of a system by preferentially sampling regions of the distribution with a large Boltzmann factor. A classic

example is the Metropolis sampling[41] in which configurations are generated from the previous state using a transition probability that depends on the difference in energy between the initial and the final states.

Let us introduce the canonical partition function Z, which characterizes the NVT ensemble,

$$Z_{NVT} = \frac{1}{h^{3N}N!}\int\int \exp(-\beta H(\mathbf{p}^N, \mathbf{r}^N))d\mathbf{p}^N, d\mathbf{r}^N, \tag{2.1}$$

where $\beta = \frac{1}{k_B T}$, h is Planck's constant, $\mathbf{p}^N$ are the generalized momenta and $\mathbf{r}^N$ are the generalized positions representing the phase space. H is the classic Hamiltonian of the system defined as the sum of the kinetic energy, E_k, and the potential energy, U, of the system. The probability of the system being in a particular state is given as:

$$\Pi(\mathbf{p}^N, \mathbf{r}^N) = \frac{\exp(-\beta H(\mathbf{p}^N, \mathbf{r}^N))}{\int\int \exp(-\beta H(\mathbf{p}^N, \mathbf{r}^N))d\mathbf{p}^N d\mathbf{r}^N}. \tag{2.2}$$

Therefore, the expectation value of a thermodynamic quantity, A can be written as:

$$\langle A \rangle = \int\int \Pi(\mathbf{p}^N, \mathbf{r}^N)A(\mathbf{p}^N, \mathbf{r}^N)d\mathbf{p}^N d\mathbf{r}^N. \tag{2.3}$$

Eqn. 2.3 is an integral over all momenta and positions which depends on $3N$ variables for an N particle system. A useful way to evaluate this integral is by way of Monte Carlo simulations using Metropolis sampling. We hereby give an outline of the scheme.

- The energy of the initial configuration $U_{old}(\mathbf{r})$ is evaluated.
- A particle is selected at random from this configuration and given a random displacement(see fig. 2.1), the choice is based on a random number $rand$, between 0 and 1. $\mathbf{r}_{new} \rightarrow \mathbf{r}_{old} + \delta(rand - 0.5)$. The choice of δ may be varied throughout the simulation to ensure that the sampling is optimal.
- The energy of the new configurations $U_{new}(\mathbf{r})$ is calculated.
- The probability of acceptance P_acc is evaluated as $P_{acc} = \exp(-\Delta E/k_B T)$, where $\Delta E = U_{new} - U_{old}$.
- The move is accepted if $P_{acc} > 1$, otherwise a random number $rand$, between 0 and 1, is generated and the move is accepted if $rand \leq P_{acc}$.

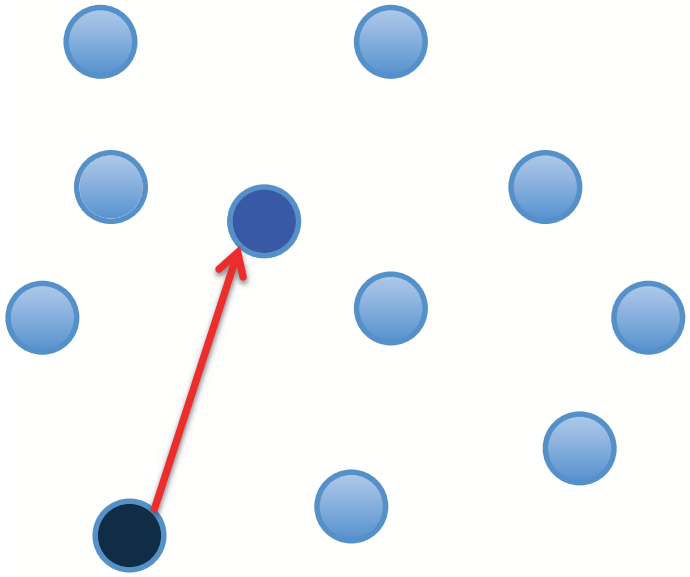

Figure 2.1: Monte Carlo move during a sampling process.

- If the new configuration is rejected, the old is used and $U_{new} = U_{old}$.
- Then the property of interest A is calculated.

From the above, the integral of eqn. 2.3 can be calculated as the ensemble average of the property $A(\mathbf{r}^N)$ measured at every configuration;

$$\langle A \rangle_{NVT} = \frac{1}{N_{MC}} \sum_{i=1}^{N_{MC}} A(\mathbf{p}^N, \mathbf{r}^N) \ , \tag{2.4}$$

where N_{MC} is the total number of attempted displacements and $A(\mathbf{r}^N)$ is a thermodynamic property associated with the configuration $\mathbf{r}^N$. The errors inherent in the evaluation of eqn. 2.4, can be reduced by increasing the number of sampled configurations. The errors are proportional to the reciprocal of the square root of the number of measurement of a given property A_i, i.e $error \propto (N_{MC})^{-1/2}$.

2.2.2 Thermodynamic Potentials from Statistical Mechanics

The thermodynamic properties of a system can be calculated from the molecular level, through the use of statistical mechanics, by relating the partition function, Z, and its dervatives to thermodynamics potentials such as the Helmholtz free energy,

F, the internal energy, U, or entropy, S. For example,

$$\begin{aligned} F &= U - TS = -k_B T \ln Z \\ &= constant + k_B T \ln \int\int \Pi(\mathbf{p}^N, \mathbf{r}^N) \exp(-\beta H(\mathbf{p}^N, \mathbf{r}^N)) d\mathbf{p}^N d\mathbf{r}^N \\ &= constant + k_B T \ln \left\langle \exp(-\beta H(\mathbf{p}^N, \mathbf{r}^N)) \right\rangle. \end{aligned} \tag{2.5}$$

The internal energy of the system is given as:

$$\begin{aligned} U &= k_B T^2 \left(\frac{\partial \ln Z}{\partial T} \right)_{N,V} \\ &= \int\int \exp(-H(\mathbf{r}^N)) \Pi(\mathbf{p}^N, \mathbf{r}^N) d\mathbf{p}^N d\mathbf{r}^N \\ &= \left\langle H(\mathbf{p}^N, \mathbf{r}^N) \right\rangle. \end{aligned} \tag{2.6}$$

The entropy can be expressed as

$$\begin{aligned} S &= k_B \ln Z + k_B T \left(\frac{\partial \ln Z}{\partial T} \right)_{N,V} \\ &= constant - k_B \int\int \Pi(\mathbf{p}^N, \mathbf{r}^N) \ln \Pi(\mathbf{p}^N, \mathbf{r}^N) d\mathbf{p}^N d\mathbf{r}^N \\ &= constant - k_B \left\langle \ln \Pi(\mathbf{p}^N, \mathbf{r}^N) \right\rangle. \end{aligned} \tag{2.7}$$

Other thermodynamic variables can be obtained in a simlar manner.

2.2.3 Umbrella Sampling

The umbrella sampling scheme, first introduced by Torrie and Valleau[42] and applied to nucleation by Frenkel and Smit[43], is a method of sampling systems where important contributions to the ensemble average are from configurations with small Boltzmann factors and where Metropolis sampling will be inefficient. In the case of a critical nucleus which appears at the top of the free energy barrier, sampling with ordinary Metropolis method would result in poor statistical measurements. The umbrella sampling method involves weighting the probability density with an arbitrary potential which forces the system to sample in regions of interest with higher probability.

In the canonical ensemble, the average, <>, of a thermodynamic quantity A is written as:

$$< A >_{NVT} = \frac{\int d\mathbf{r}^N A(\mathbf{r}^N) \exp(-\beta U(\mathbf{r}^N))}{\int d\mathbf{r}^N \exp(-\beta U(\mathbf{r}^N))}$$

$$
\begin{aligned}
&= \frac{\int d\mathbf{r}^N A(\mathbf{r}^N) W(\mathbf{r}^N)^{-1} \exp(-\beta U(\mathbf{r}^N)) W(\mathbf{r}^N)}{\int d\mathbf{r}^N \exp(-\beta U(\mathbf{r}^N)) W(\mathbf{r}^N)^{-1} W(\mathbf{r}^N)} \\
&= \frac{\left\langle A/W(\mathbf{r}^N) \right\rangle_W}{\langle W(\mathbf{r}^N)^{-1} \rangle},
\end{aligned}
\tag{2.8}
$$

where $W(\mathbf{r}N)$ is the weighting function. For liquid-solid nucleation, we wish to integrate eqn. 2.8 numerically with respect to $A(\mathbf{r}^N)$, which in our case is the distribution of the embryos of size n, (N_n), within a cluster of N atoms. The average now becomes:

$$
\langle N_n \rangle_{NVT} \approx \frac{\sum_i^M N_n(\mathbf{r}^N)/W(\mathbf{r}^N)}{\sum_i^M W(\mathbf{r}^N)^{-1}}. \tag{2.9}
$$

The weighting function is defined as $W(\mathbf{r}^N) = \exp(-\beta\omega(\mathbf{r}^N)$, where $\omega(\mathbf{r}^N)$ is a bias potential chosen in order to control the size of the largest embryo in the system. The bias potential used in this work has a harmonic form,

$$
\omega[n(\mathbf{r}^N)] = \frac{1}{2} k_n \left[n(\mathbf{r}^N) - n_0 \right]^2, \tag{2.10}
$$

that is centered around the embryo with largest embryo size n_0, where $n(\mathbf{r}^N)$ is the embryo size as a function of atomic position. The constant, k_n, restricts the range of embryo size that is being sampled, while n_0 is the umbrella center which determines embryo sizes that are sampled most.

2.2.4 Parallel Tempering

Condensed phase systems possess complex potential energy surfaces with many potential energy minima that are separated by high energy barriers. At low temperatures, such systems become trapped in an individual potential energy basin and become non-ergodic. Traditional Metropolis methods would be grossly inefficient in this case since its local moves do not allow the system to explore all of the configurational space[44].

The parallel tempering algorithm solves this problem by supplementing the local Metropolis move with a swap move that exchange configurations in different

regions. This is implemented by extending the partition function to sample many configurations with different temperatures at the same time. In this way, the barriers between the local minima are overcome by swapping configurations between different thermodynamic states as shown in fig. 2.2.

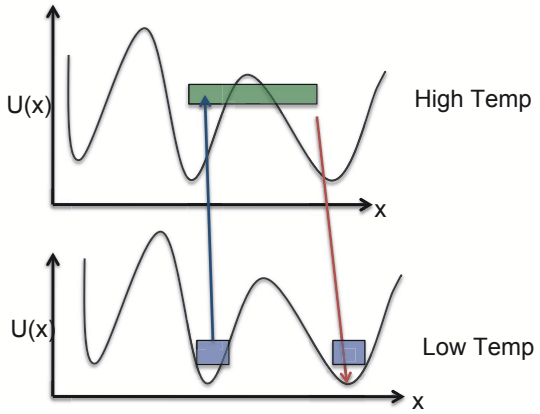

Figure 2.2: The interchange of configuration at the low temperature to a high temperature allowing the system to overcome potential energy barriers before returning to a lower temperature at some later time.

We define a system i with temperature T_i. A collection of k systems of this nature, in order of increasing temperature, $T_1 < T_2 < T_3 ..... T_k$, form a system whose partition function Z_{ext} is defined as the product of the individual partition function in NVT_i ensembles,

$$Z_{ext} = \prod_{i=1}^{N} Z_{NVT_i} = \prod_{i=1}^{N} \frac{1}{\Lambda_i^{3N} N!} \int ... \int d\mathbf{r}^N \exp\left[-\beta_i U(\mathbf{r}_i^N)\right], \tag{2.11}$$

where $\mathbf{r}_i^N$ is the positions of N particles in system i. Although it may be sufficient, in principle, to sample all individual ensembles, it is also possible to introduce a MC move that swap configurations between two ensembles with a probability that obeys the condition of detailed balance(cf. Appendix B).

The basic idea is to recognize that a valid equilibrium configuration at one temperature is also a valid configuration at another temperature, only with a different acceptance probability. For a configuration of a system i denoted as $\mathbf{i} = \mathbf{r}^N$, the detailed balance condition may be cast as:

$$\frac{acc\left[(\mathbf{i},\beta_i),(\mathbf{j},\beta_j) \rightarrow (\mathbf{j},\beta_i),(\mathbf{i},\beta_j)\right]}{acc\left[(\mathbf{i},\beta_j),(\mathbf{j},\beta_i) \rightarrow (\mathbf{i},\beta_i),(\mathbf{j},\beta_j)\right]} = \frac{\exp\left[-\beta_i U(\mathbf{j}) - \beta_j U(\mathbf{i})\right]}{\exp\left[-\beta_i U(\mathbf{i}) - \beta_j U(\mathbf{j})\right]}$$

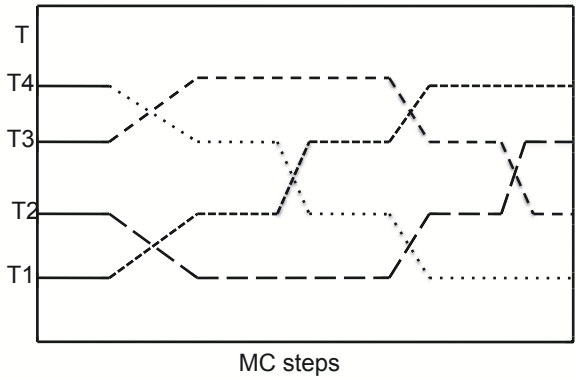

Figure 2.3: Exchange of temperature in parallel tempering as the simulation progress .

$$= \quad exp(\beta_i - \beta_j)\left[U(\mathbf{i}) - U(\mathbf{j})\right]. \qquad (2.12)$$

Computationally, the swapping the parameters between the processors is less expensive compared to swapping the configurations because swapping the entire configurations will take more CPU time. In summary, a chain of MC moves for every configuration at a fixed temperature is accepted based on

$$P_{acc}(o \rightarrow n) = min\left[1, exp(-\beta(U(n) - U(o)))\right] \ , \qquad (2.13)$$

while swapping between i and j configurations at different temperatures is made according to

$$P_{acc}(i \rightarrow j) = min\left[1, exp(-(\beta_j - \beta_i)(U(i) - U(j))\right]. \qquad (2.14)$$

This scheme is most useful for cases with many local minima, therfore swapping between states with higher energy and that of lower energy, will allow for sampling of all the states with greater efficiency.

2.3 Molecular Simulation Calculation of Free Energy Barrier to Nucleation

2.3.1 Molecular Potential

The use of a simple pair potential in describing interactions at the atomic level has been successful, especially for noble gases and simple molecules where the Lennard-Jones potential is one of the main interaction potentials used due to its simplicity[45].

But as the complexity of the atomic interaction increases, the atoms are no longer weakly bonded, therefore the nature of the chemical bond on every atom and its particular chemical environment must be accounted for.

For our studies, we use the Embedded Atom Method (EAM) potential introduced by Baskes *et al*[46]. The EAM potential is built on the insight gained through density functional theory(DFT) which uses the local electron density to deduce the energy of the system. This approach assumes that the total electron density of a metal is approximated by a linear superposition of the density from individual atoms. The electronic density in the vicinity of each atom is expressed as the sum of the density contributed by the atom plus a constant background density. The total energy of a particle is given as:

$$E_i = F_i(\rho_i) + 1/2 \sum_{j(i \neq j)}^{N_{nb}(i)} V_{i,j}(r_{ij}). \tag{2.15}$$

Here $V_{ij}(r_{ij}) = \frac{1}{4\pi\epsilon_0} Z_i^a(r_{ij}) Z_j^a(r_{ij})/r_{ij}$ is the pair potential between atom i and its neighbor j, Z is the screened nuclear charge of atom a and r_{ij} is the inter-atomic distance for atomic pair. The electron density ρ for atom i is given as

$$\rho_i = \sum_{j(i \neq j)} \rho_j^a(r_{ij}). \tag{2.16}$$

The values of the parameters used in the calculation of electron density, $\rho_j^a(r_{ij})$, the pair potential, V_{ij}, and the embedded atomic potential functional $F_i(\rho_i)$ are obtained by fitting experimental data to information such as lattice parameters, elastic constants, cohesive energies, vacancy formation energy etc.

It should be noted that the sum in eqn. 2.15 runs over the neighbors of atom i which are defined as those atoms within the cutoff radius r_c. This means that the local environment of any particle is well described, therefore, this potential allows for the accurate description of surfaces and defects.

2.3.2 Solid Embryo Criteria

In order to calculate the free energy with respect to the size of the embryo, we need to identify an $n - sized$ solid embryo evolving from the liquid phase. This, we need to do in such a way that our simulation method does not prefer a certain crystal structure (such as FCC, BCC or Ih) over the others. Another basic requirement is

the choice of the order parameter must be applicable to surface atoms where there number of neighbors is about half that found in the bulk[47]. Two steps are involved in our cluster criteria. The first is to identify all solid-like atoms in the cluster based on their local environment. The second is to identify which solid-like atoms belong to the same embryo.

Order Parameter

Steinhardt *et al*[24] suggested that the spherical harmonic functions could be used to determine the local structure around and individual particle. The idea here being that two atoms, i and j, in the crystalline solid should have well defined angular orientation relating to each other, whereas there is no correlation for atoms in the liquid environment.

We start by identifying an order parameter for a single particle by summing the orientational order over all the number of nearest neighbors, $N_{nb}(i)$, and take the average.

$$\hat{q}_{lm}(i) = \frac{1}{N_{nb}(i)} \sum_{j=1}^{N_{nb}(i)} Y_{lm}(\mathbf{r_{ij}}), \tag{2.17}$$

where $Y_{lm}(\mathbf{r}_{ij}) = Y_{lm}(\theta(\hat{r}), \phi(\hat{r}))$ is a spherical harmonic function, the angles θ and ϕ, measured from an arbitrary coordinate reference, are defined by radial vectors between atoms i and j. Next, we define a complex vector of order $l = 6$, where l is chosen such that the average $\tilde{q}_{lm}$ is not vanishing. For Icosahedral, FCC and BCC structures, $l = 6$ is generally chosen as it has a non vanishing value as shown in Table 1.1. This complex vector $\hat{q}_{6m}(i)$ is then divided by its magnitude giving

$$\tilde{q}_{6m}(i) \equiv \frac{\hat{q}_{6m}(i)}{\sqrt{\sum_{m=-6}^{6} |\hat{q}_{6m}(i)|^2}}. \tag{2.18}$$

The dot product, c_{ij}, which is our order parameter is the product of the complex vector and its complex conjugate is given as:

$$c_{ij} = \sum_{m=-6}^{6} \tilde{q}^*_{6m}(i).\tilde{q}_{6m}(j). \tag{2.19}$$

The value of c_{ij} is close to unity when the atoms are in the same environment and very small otherwise. This helps in the identification of ordered atoms in the

embryo. The parameters required to define the dot product order parameter needed to construct a solid embryo distribution are the neighbor distance, r_b, the threshold dot product C_{min} and the threshold number of connection per neighbor, $C_x N_T$. The neighbor distance r_b is defined as the distance to the first local minima of the radial distribution function. Mendez[47] determined the optimal neighbor distance for a gold cluster by observing the distribution of neighbors for various distances in a 3892-atom cluster. It was seen that $r_b = 3.5\mathring{A}$ gave the peak value for $N_{nb} = 12$, which corresponds to the number of neighbors for FCC, HCP and icosahedral structures. This is the cutoff distance we use in this work beyond which atoms are not considered as neighbors.

The threshold dot product C_{min} was determined by considering the distribution of c_{ij} in the liquid and solid phases of 3892-atom gold cluster[47]. Lower values of c_{ij} had higher frequencies within the liquid phase, while in the solid phase high values of c_{ij} had higher frequencies. C_{min} was chosen as the point within the solid phase close enough to the point where the two distribution cross each other (see fig. 2.4) with value of $C_{min} = 0.65$. Atoms i and j are connected if the $c_{ij} \geq C_{min}$.

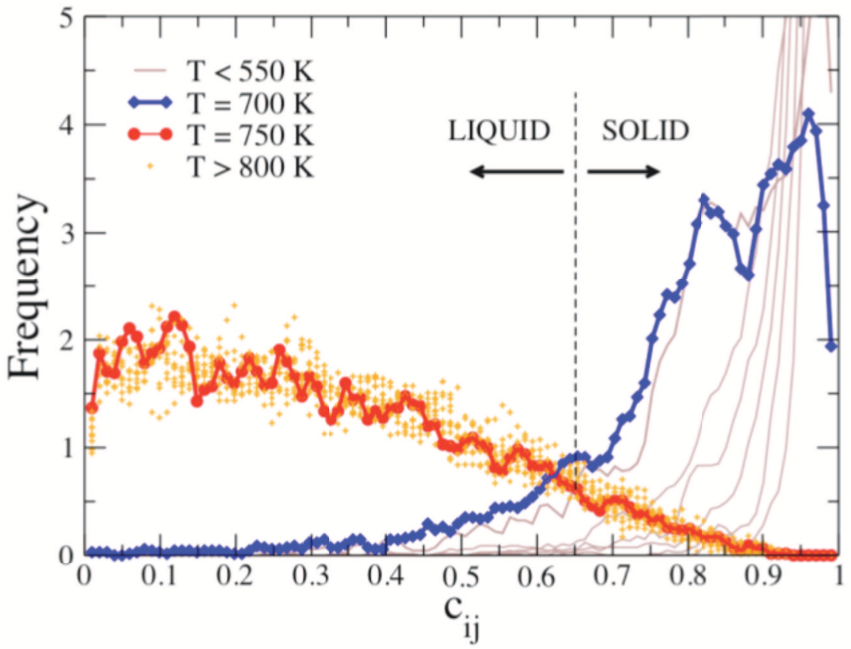

Figure 2.4: A normalized dot product distribution for 456-atom cluster taken from ref.[47].

For a chosen atom i, the number of neighbors to which it is connected to is counted. The number of connected neighbors is divided by total number of neighbors to obtain the number of connections per neighbor, $C_xN(i)$. This criterion takes into consideration that atoms on the surface, with fewer neighbours, can still form part of a solid embryo. To set the threshold for the parameter, the distribution for the number of connections per neighbor was obtained for both core and surface atoms[47] for all the temperature range studied. For temperatures lower than $725K$, higher values of $C_xN(i)$ were observed as compared to lower values seen for higher values temperatures. The threshold C_xN_T was chosen as 0.5 where any atom having a value higher than this is declared as solid-like irrespective of whether it is on the surface or bulk. Since these parameters are dependent on the properties of the system studied and not on the size of the cluster[47], we use the values in our present calculations.

The process of identifying an $n-sized$ embryo of solid-like particle is summarized as follows:

(**a**) We first calculate the distance, $d(i,j)$ between a particular atom i, and a prospective neighbor j. If the distance is less than or equals a minimum neighbor distance, r_b, the atoms i and j are said to be neighbors and share a bond.

(**b**) For all the neighbors of atom i, a dot product c_{ij} is calculated. The value of c_{ij} determines the connected neighbors of atoms i. If $c_{ij} \geq C_{min}$, then the two neighbors are connected.

(**c**) The ratio of the connected neighbors to all neighbors is calculated as $c_{xn}(i) = N_{con}(i)/N_{nb}(i)$. This is compared to the threshold number of connection per neighbor, if this ratio $c_{xn}(i)$ is greater than the threshold value, C_xN_T, then the atom is said to be solid, otherwise, it is regarded as liquid.

(**d**) Finally, two solid atoms are said to belong to the same embryo if they are connected. This criteria is used to count all the solid embryo and therefore identify the largest embryo in the cluster.

2.3.3 Free Energy Barrier to Nucleation for a 276-Atom Cluster

Nucleation is an activated process as it requires a minimum free energy to be overcome before the formation of a stable phase. The appearance of an embryo with

this minimum free energy (critical embryo) is a rare event in a system with mild metastability, therefore the need for a suitable technique to generate reasonable and unbiased statistics. We therefore make use of umbrella sampling together with parallel tempering both discussed in subsections 2.2.3 and 2.2.4

We define a Hamiltonian, H_{EAM}, as the sum of the potential and kinetic energies of the system,

$$H_{EAM} = E_{EAM} + E_K. \tag{2.20}$$

The EAM potential energy is as described in section 2.3 and the kinetic energy E_K of a cluster is given as $E_K = \frac{3}{2}k_B\sum_{i}^{N} T_i$, where N is the number of particles in the system and T_i is the temperature of a given particle "i".

Following our umbrella sampling scheme, a potential which is a function of the maximum embryo, $\phi(n_{max})$, is added to the unconstrained Hamiltonian to produce a constrained Hamiltonian, H_C

$$H_C = H_{EAM} + \phi(n_{max}) \tag{2.21}$$

This biased potential depends on the "umbrella constant",κ, and the umbrella center, n_0.

$$\phi(n_{max}; \kappa, n_0) = \frac{\kappa}{2}(n_{max} - n_0)^2 \tag{2.22}$$

The added harmonic potential forces the system to sample states close to the umbrella center, while the umbrella constant, κ, restricts the system from sampling embryo distribution that are far off the umbrella center. The umbrella centers were chosen with values starting from 0 to 70 in step of 10, i.e, $n_{0,\nu}$=$\{$0, 10, 20, 30, 40, 50, 60, 70$\}$ and the optimal value for the umbrella constant was set at $\kappa = 0.001$. Based on the values of $n_{n_0,\nu}$ and κ, there was a 60% to 70% efficiency in the swapping of the configurations with common temperatures and neighboring umbrella centers, n_0.

We also used the parallel tempering method with eight temperatures, $T_\nu = \{660K, 665K, 670K, 680K, 690K, 700K, 710K, 730K\}$. The choice of the highest temperature (T=730K), was made to satisfy the basic requirement of the parallel tempering technique which demands that at least one of the temperatures be chosen high enough (above the melting temperature of $T = 680K$ for $N = 276$) that the system can move between all potential minima freely. Swapping of configurations

with common umbrella centers and neighboring temperature was observed to be 60% efficient.

Our biased ensemble is given as the product of all the subsystems with a number summing to the product of the number of the temperatures used by the total number of umbrella centers. For our study, we used 8 umbrella centers over the range of 8 different temperatures.

$$Q_C = \prod_{\mu=1}^{8}\prod_{\nu=1}^{8} Q_{N,P,T_\nu,U_C(\mu,\nu)} = \prod_{\mu=1}^{8}\prod_{\nu=1}^{8} \frac{1}{\Lambda_\mu^{3N} N!}\int ... \int dr^N \exp\left[-\beta_\mu U_C(\mu,\nu)\right] \quad (2.23)$$

We obtain the average of the unconstrained embryo distribution $< N_n >$ from the embryo distribution, N_n in the unconstrained system using the relation;

$$\begin{aligned} \langle N_n \rangle &= \frac{\langle N_n \exp[\phi(n_{max})/k_B T]\rangle_C}{\langle \exp[\phi(n_{max})/k_B T]\rangle} \\ &\cong \frac{\sum_{k=1}^{X_{MC}}\sum_{n=0}^{n_{max}} N_n \exp[\phi(n_{max})/k_B T]}{\sum_{k=1}^{X_{MC}}\sum_{n=0}^{n_{max}} \exp[\phi(n_{max})/k_B T} \end{aligned} \quad (2.24)$$

where $\langle . \rangle_C$ represents the average in the constrained ensemble. Equation 2.24 measures the embryo distribution, where N_n denotes the number of embryo with size n in the MC iteration k, and ϕ_k is the biased potential for the k sampling. n_{max} is the largest embryo size.

In the present simulation, a Monte Carlo (MC) move corresponds to a single attempt to move a particle by a magnitude of ΔR. N such moves constitute our Monte Carlo step, where particles are chosen at random. An MC trajectory involves 10 attempted MC steps. We analyze for the largest embryo size after every MC trajectory and then apply the constrained potential. This is chosen to minimize the computational effort required to evaluate the embryo distribution. Our MC cycles involve 10 attempted MC trajectories each followed by sampling under constrained potential. Swapping is attempted in the umbrella centers after 10 MC trajectories (1 MC cycle) and a swapping attempt for every 10 MC trajectories in temperatures for configurations with neighboring temperatures having the same umbrella centers. The simulation was run for a total of 150,000 trajectories for every node, but we

dropped the initial 10,000 trajectories from the statistics used to generate the free energy. This is to ensure that the system was properly equilibrated before using the statistics.

The free energies are obtained using the relationship,

$$\frac{\Delta G(n)}{k_B T} = -\ln P_n + b, \tag{2.25}$$

where b is a constant, and P_n is the probability of observing an $n - sized$ embryo within the system. Reiss *et al*[19] had showed that for a rare event $P_n \approx \langle N_n \rangle$ (cf. section 1.4). Using this approximation, our free energy expression becomes;

$$\frac{\Delta G(n)}{k_B T} = -\ln \langle N_n \rangle + b, \tag{2.26}$$

where $\langle N_n \rangle$ are unique to each node in the system, i.e, $b = b(T_\mu, n_{0,\nu}), T = T_\mu$ and $\langle N_n \rangle = \langle N(n; T_\mu, n_{0,\nu}) \rangle$.

The free energies obtained from eqn. 2.26 for each umbrella window differ from each other by a constant as the sampling occurs under different biasing potentials. To obtain a complete free energy surface, we could use the overlapping distribution method[43]. But due to the additive nature of statistical error inherent in this approach, we obtain an optimal alignment of the common temperature free energy by finding the coefficients of the polynomial[25]:

$$\Gamma(n) = \sum_{k=1}^{k_{max}} a_k n^k + c, \tag{2.27}$$

through the expression

$$\Omega = \sum_{n=0}^{max(n)} \left\{ \sum_{i=1}^{n_w} w_i(n) \left[\frac{\Delta G_i(n)}{k_B T} - \Gamma(n) \right]^2 \right\}. \tag{2.28}$$

Eqn. 2.28 is the squared error of the difference between the simulation measurements and the expected values given by the polynomial $\Gamma(n)$. This difference is weighted by multiplying it with the reciprocal of the standard deviation from the measurement in every simulation window, i.e, $w_i(n) = 1/\sigma^2_{\Delta G_i(n)}$. The summation in eqn. 2.28 is over all embryo sizes, (i.e, $n = 0$ to $n = max(n)$) and for $i = 1$ to n_w where n_w is the number of umbrella windows. The standard deviation σ

was obtained from four independent simulations which were cut down into halves to generate eight sets from which σ could be calculated. The standard error is in the order of $0.5k_BT$ for measurement around the umbrella center and $1.0\ k_BT$ at the extremes of the umbrella regions. To minimize this error, and based on the fact that not enough sampling can be made in the constrained space where the embryos are far from the umbrella center, we only consider statistics within the region $n_0 - 10 \leq n_{max} \leq n_0 + 10$.

2.3.4 Calculation of 2D Free Energy Barrier for a 456-Atom Cluster

One of our goals is to understand the role of the position of the embryo within the nanoparticles during nucleation. Therefore, we aim to capture the relationship between the embryo distance from the center of mass of the system and the nucleation barrier. In calculating the 2-dimensional free energy surfaces, we chose a different temperature set, T_μ=650, 660, 670, 680, 690, 710, 730, 750 in degree Kelvin, but maintained all the other simulation conditions described in subsection 2.2.3. Here, the free energy we desire is a function of the embryo size, n, and the distance, d, from the center of mass of the cluster. The details of this simulation are the same as that described in subsection 2.2.3, but a different set of statistics for the embryo-distance distribution is obtained. The expression for obtaining the 2-dimensional free energy barrier is given as:

$$\frac{\Delta G(n,d)}{k_BT} = -\ln P_{n,d} + b, \tag{2.29}$$

where, $P_{n,d}$ is the probability of having $n - sized$ embryo at a distance d from the center of mass of the whole cluster.

The averaged embryo-distance distribution $\langle N_{n,d}\rangle$in the unconstrained space is obtained as

$$\begin{aligned} < N_{n,d} > &= \frac{\langle N_{n,d} \exp[\phi(n_{max})/k_BT]\rangle_C}{< \exp[\phi(n_{max})/k_BT] >} \\ &\cong \frac{\sum_{k=1}^{X_{MC}} \sum_{n=0}^{n_{max}} \sum_{d=0}^{d_{max}} N_{n,d} \exp[\phi(n_{max})/k_BT]}{\sum_{k=1}^{X_{MC}} \sum_{n=0}^{n_{max}} \sum_{d=0}^{d_{max}} \exp[\phi(n_{max})/k_BT}. \end{aligned} \tag{2.30}$$

where the inner summation is over all possible distance. The distance d, is the distance between the location of the center of mass, r_{cm}, of $n - sized$ embryo and the the center of mass of the whole cluster, R_{cm}

$$d = \sqrt{(R_{cm} - r_{cm})}^2. \tag{2.31}$$

To be sure that the distribution we get with respect to the distance, d, is not a random distribution of particle distance from the center of the cluster, we compare the embryo's distance distribution for the given umbrella center, $n_0 = 20$ with a random partcle distance within the cluster. Fig. 2.5 is the distribution of largest embryo distance at different umbrella distances at a fixed temperature. Fig. 2.6 shows the distribution of the largest embryo distance for all the temperatures while the distribution of atomic distances from the center of mass is shown in fig. 2.7. Due to the continuous nature of the distance, we divide the distances into small bins in order to obtain reasonable statistics. Though the average is calculated with respect to both embryo size and their distance, but our Hamiltonian is constrained only with the maximum embryo size.

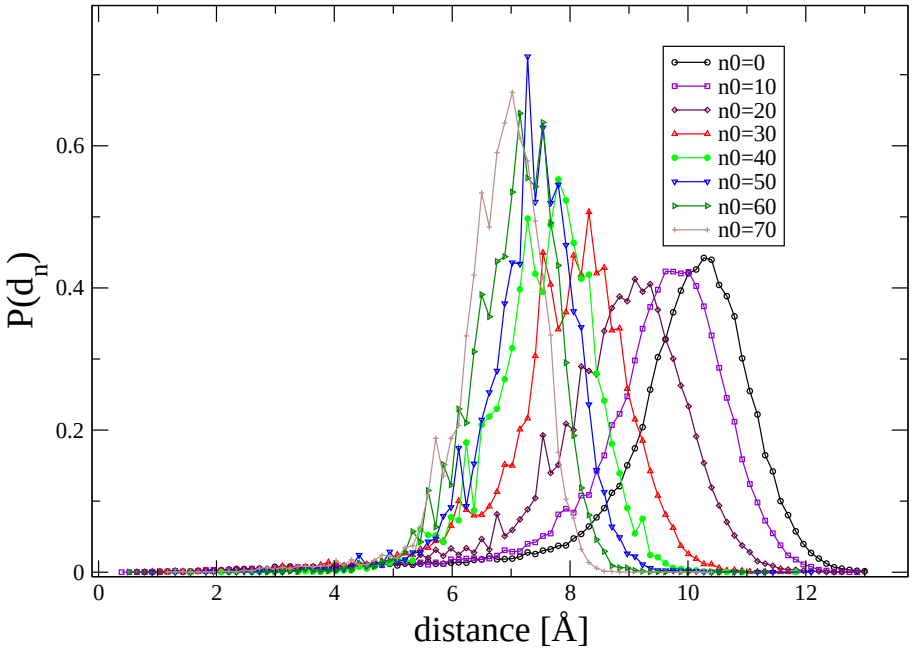

Figure 2.5: The piecewise distribution of largest embryo distance for all the umbrella centers at a temperature of $T = 690K$.

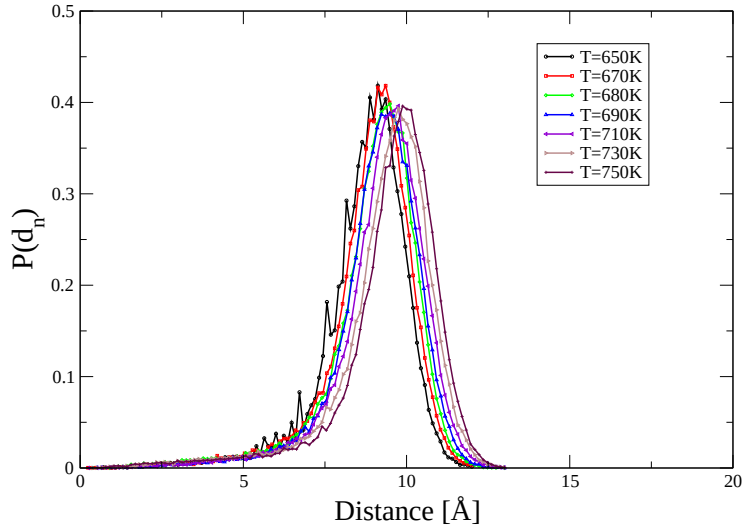

Figure 2.6: Largest embryo distance distribution at umbrella center $n_0 = 20$ for all the temperatures

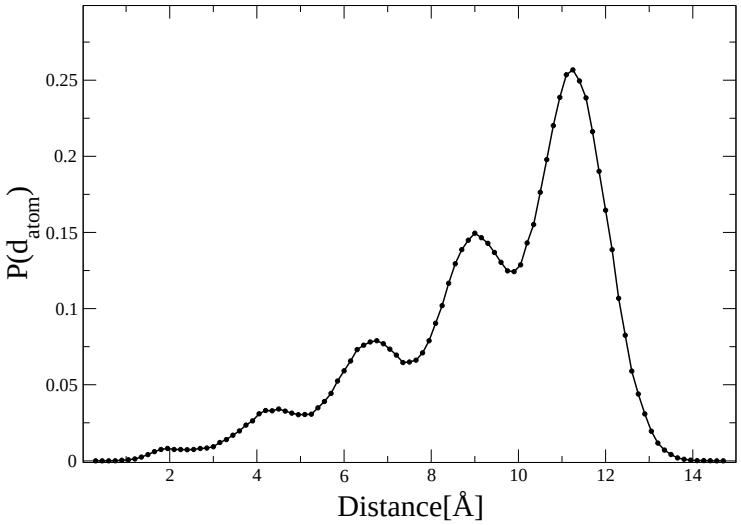

Figure 2.7: The distribution of atom distances from the center of mass within a 456 atom gold cluster.The distance is averaged over all temperature and umbrella centers.

We run the simulations for a total of 120,000 trajectories for each node and drop the initial 10,000 trajectories to take care of the initial equilibration of the system. The piecewise averages $\langle N_{n,d} \rangle$ were abtained and used to extract the free energy surfaces through a relation similar to eqn. 2.26.

$$\frac{\Delta G(n,d)}{k_B T} = -\ln(\langle N_{n,d} \rangle + b \tag{2.32}$$

2.4 Results and Discussions

2.4.1 Free Energy Barriers for a 276-Atom Gold Cluster

Fig.2.8 shows the constrained embryo distribution for all umbrella centers with $T = 680K$ for the 276-atom cluster.

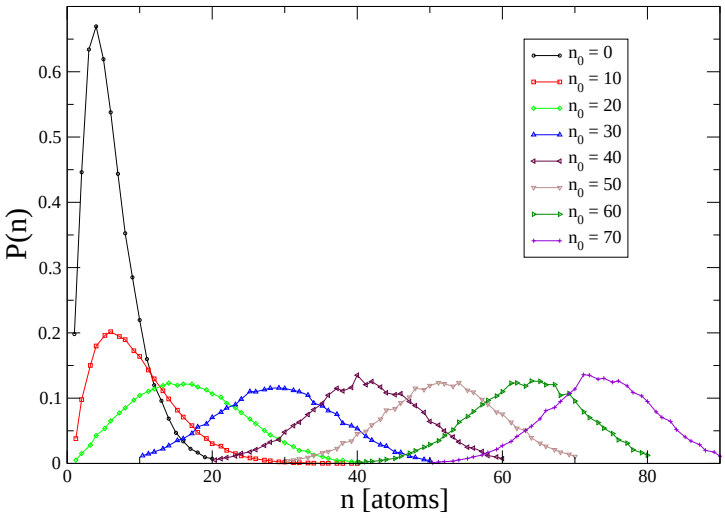

Figure 2.8: Embryo distribution in the constrained ensemble for all the umbrella centers at $T = 680K$.

Fig. 2.9 shows the full free energy curves for all the temperatures considered, while table 2.1 summarizes the critical sizes and the energy barrier for all temperatures for the 276 atom cluster. There is a marked increase in the free energy barrier and the critical embryo size as the temperatures increase. When compared with that

of larger cluster size (see fig. 2.10,left), the energy barriers are within error of each other, but the 276-atom cluster free energy appears to have a sharp temperature dependence. A plot of the critical sizes for our 276 atom cluster shows a relatively higher n^* compared to those of 456 atom cluster (fig. 2.10 right).

Table 2.1: Table showing the critical size and the free energy barrier for 276 atom cluster .

Temp[$^\circ K$]	$n^*[atoms]$	$\Delta G(n^*)/(k_BT)$
660	37	9.71
665	43	9.84
670	44	10.04
680	46	10.38
690	48	10.81
700	51	11.12
710	58	12.71
730	-	-

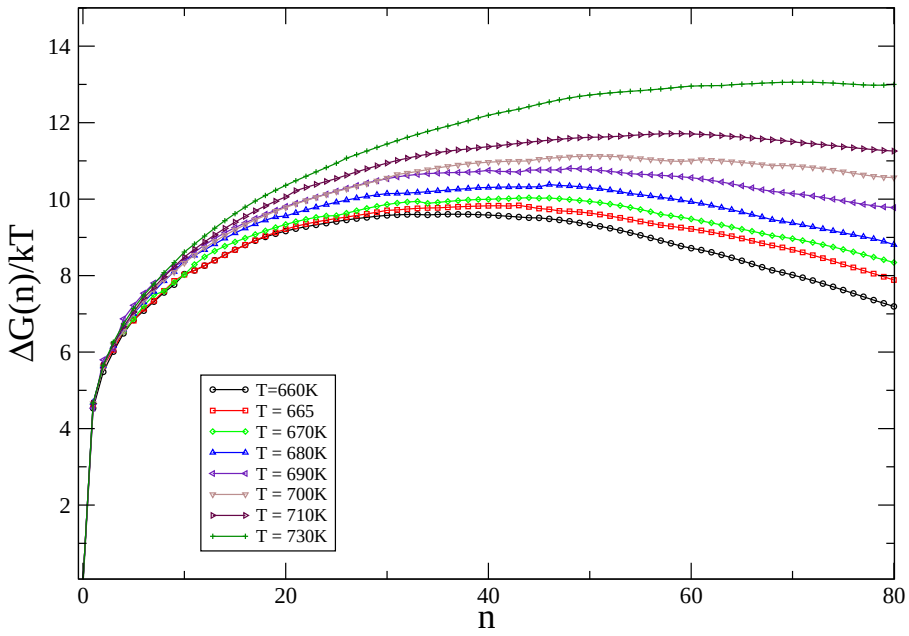

Figure 2.9: Free energy curves calculated from $\langle N_n \rangle$ for 276 atom cluster

.

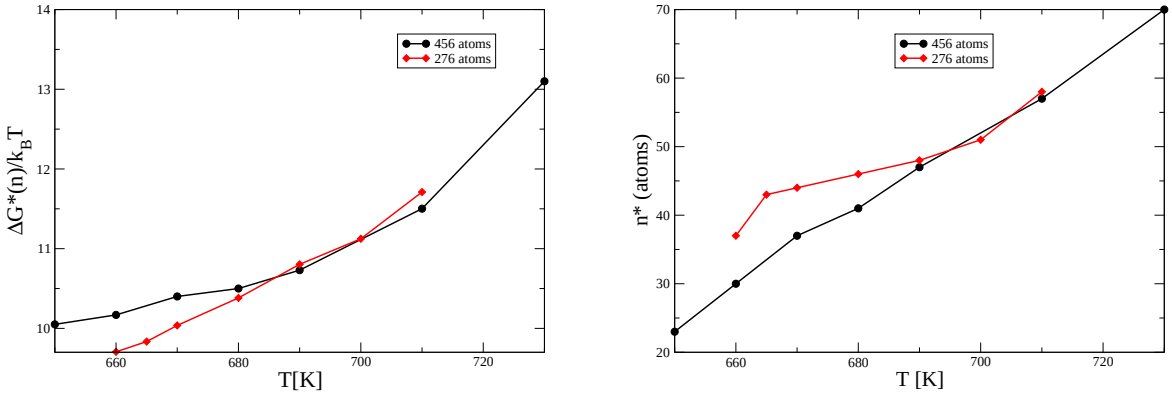

Figure 2.10: Comparison of free energy barriers and critical embryo sizes. Left: Free energy barrier for for 276 atoms cluster compared with 456 atoms cluster at various temperature . Right: Critical embryo sizes as a function of temperature for the different cluster sizes .

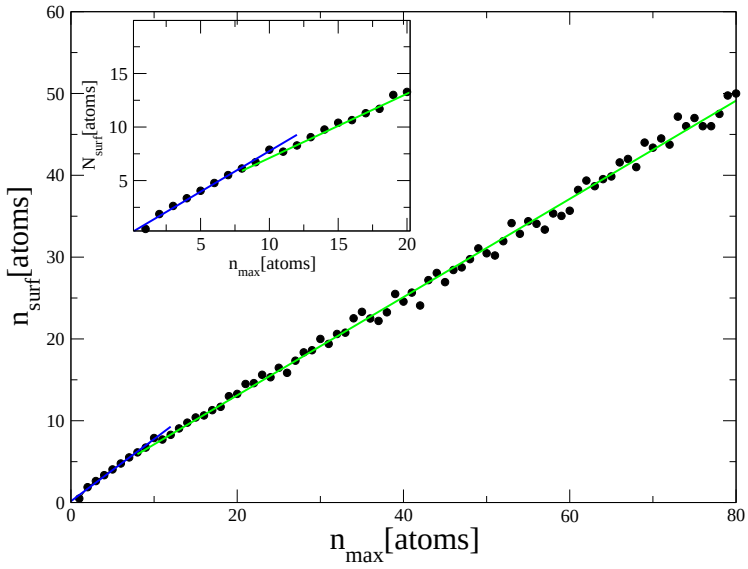

Figure 2.11: Number of atoms on the surface belonging to the maximum embryo size versus N_{max} for the 276 atom cluster.

For a given maximum embryo size in a configuration, we calculated the number of solid-like atoms belonging to the solid-vapor interface. Fig. 2.11 shows a plot of

the number of solid-like atoms on the surface, n_{surf}, against the embryo size. It is observed that for smaller embryos, *i.e* $n_{max} < 11$, 76% of the solid-like atoms belong to the solid-vapor interface. As the embryo grows bigger ($n_{max} > 11$), the number reduces to 60%. For a 456-atoms cluster, Mendez[47] observed that 60% of the solid-like atoms were on the surface for $n_{max} < 18$ and 47% for $n_{max} > 18$. This shows that freezing starts at the surface as a greater percentage of the solid-like atoms in an embryo belong to the surface. The higher percentage of surface atoms in our cluster compared to the larger cluster is expected because because the smaller cluster has an increased total number of surface atoms.

2.4.2 2-Dimensional Free Energy Barrier for a 456-Atom Gold Cluster

The 2-dimensional free energies calculated for the 456-atoms gold cluster show some interesting characteristics. Fig. 2.12 shows the free energy surface at 650 K. It is observed that the evolving embryo starts at the surface as seen by the lower free energy at larger distances from the center of mass of the cluster as the nucleation starts. The channel on this free energy surface corresponds to a minima where a particular embryo size has the highest probability. The position of this "channel" goes down as the embryo size increases, signifying a decrease in the distance at which the embryo forms. This suggests that though nucleation starts at the surface, the growth is inward. Taking the free energy along the channel for all the sizes gives a typical free energy barrier as shown in fig. 2.13. The distance which corresponds to a minimum on the free energy surface as a function of embryo size shows that as the embryo becomes larger, the distance becomes smaller (see fig. 2.14).

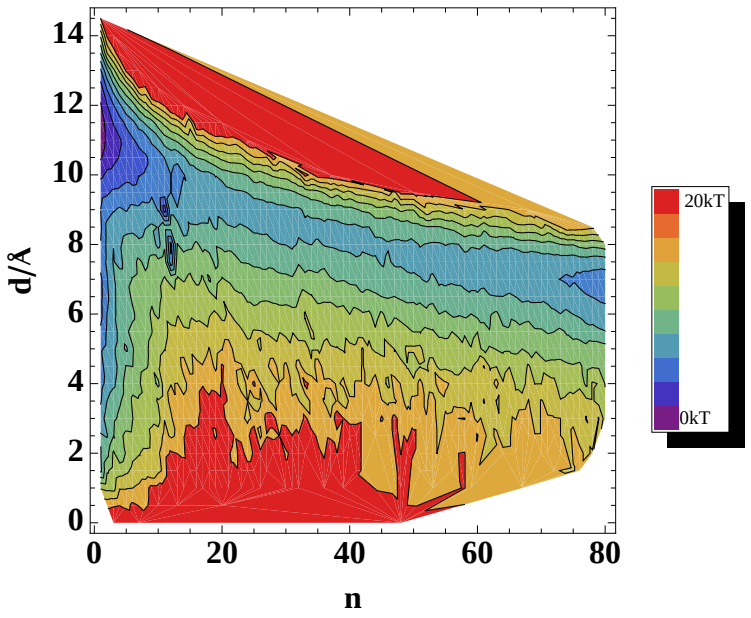

Figure 2.12: Free energy surface for 456 atoms gold cluster at $= 650K$ calculated as a function of embryo size and embryo distance.

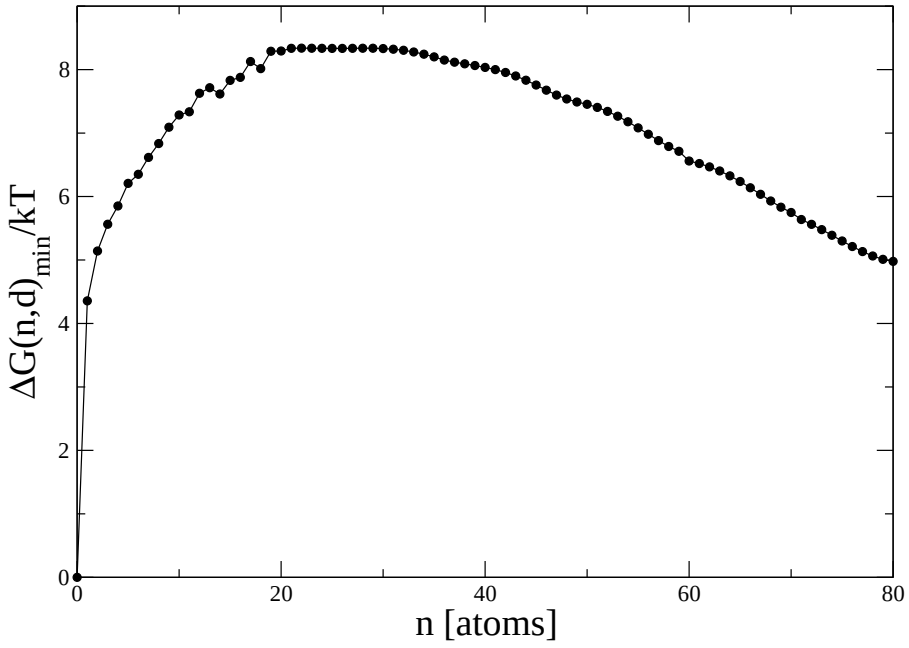

Figure 2.13: Free energy barrier for 456 atom gold cluster at $T = 650\ K$ calculated along the minima in fig. 2.12.

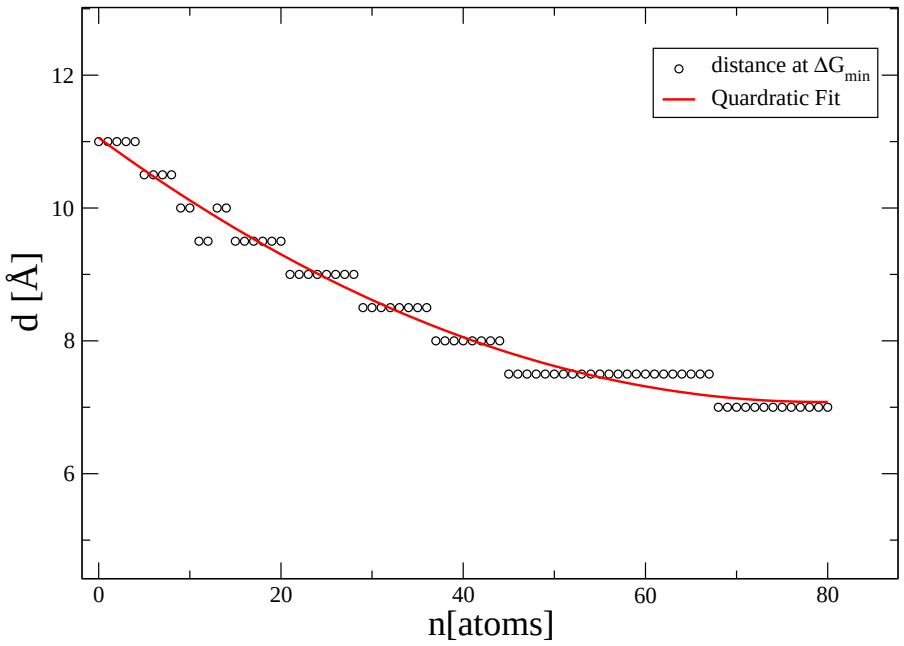

Figure 2.14: The embryo distance at which a minimum occurs for a given embryo size for 456 atoms cluster at 650 K.

Figures 2.15 left and right show ΔG^* and n^* obtained by considering the free energy as a function of n, along the free energy minima. The free energy barriers obtained with their critical sizes show a marked linearity in temperature.

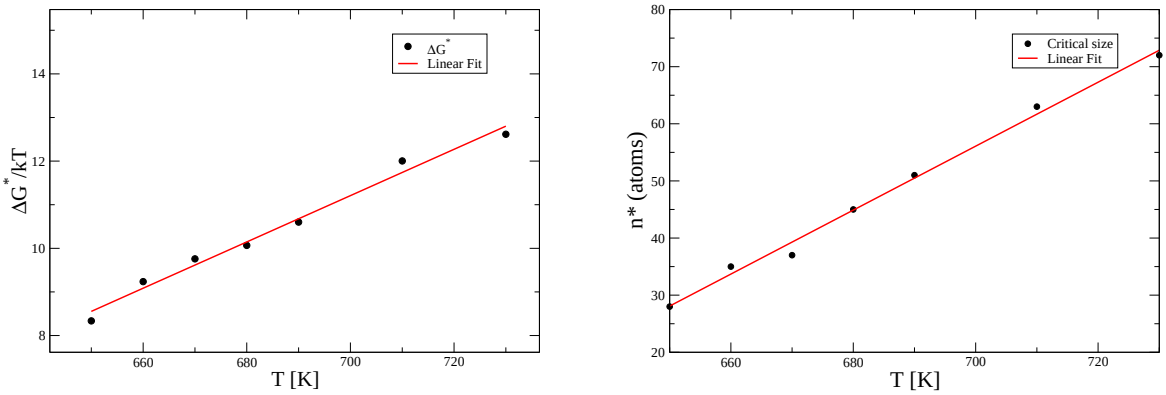

Figure 2.15: Critical free energy (left) and critical size (right) for the two dimensional free energy surface calculated for a 456-atom cluster.

Chapter 3

Phenomenological Models

3.1 Introduction

A basic definition of phenomenological models is that they are representations of observable properties of their target systems without hidden mechanisms[48]. Another interesting though strict definition due to McMullin[49] defines phenomenological models as models that are independent of theories. Though many phenomenological models follow the later definition, many incorporate basic principles and ideas related to theories [48]. For example, the liquid drop model used in the study of the gas-liquid phase transition is characterized as having a liquid core and a sharp interface between the liquid and the vapor phase. While they are not grounded in microscopic theory, phenomenological models have the advantage of being simple and can be used to test our physical intuition.

The goal of this chapter is to develop some simple phenomenological models in the spirit of the capillarity approximation, and use them to fit the free energy curves obtained from our simulation in Chapter 2. The capillarity approximation, which is used extensively in nucleation studies[1, 2, 3, 5, 7, 29, 37], describes the thermodynamic properties of the respective phases in terms of the bulk system properties. Also, the liquids and solids are considered to be incompressible and interfaces between phases as being sharp, having the bulk planar surface tension. This approximation has some inherent limitations which include measuring the thermodynamic variables at equilibrium and as such does not necessarily account for the translational, rotational or vibrational contributions to the energy barrier correctly[19, 28]. Despite the short comings of the capillarity approximation, it is still widely used due to its simplicity and applicability to predicting nucleation rates in terms of the

easily accessible macroscopic properties. It has been successfully used in predicting the limits of metastability down to small sizes ($\sim$ 100 particles) in the form of the Kelvin relation. In the present work, we attempt to model surface nucleation observed in gold nano-particles[7] and therefore seek to explain the shape and height of the observed nucleation barrier.

For the models we study, the minmum work of formation of $n - sized$ embryo is derived using the Gibbs droplet model[11]. As a general model expression and starting point, we represent the change in the free energy as,

$$\Delta G(n) = \sum_i \sigma_i A_i(n) + n\Delta\mu, \tag{3.1}$$

where σ_i and A_i are the surface free energies (surface tensions) and areas of the different interfaces between phases respectively. The summation takes place over the liquid-vapor, liquid-solid and solid-vapor interfaces. In principle, the summation could also include the different anisotropic facets of the crystal ($< 111 >$, $< 110 >$ etc.) but these have been neglected in the current work.

Three models are developed in this chapter, the spherical cap model (section 3.2), the modified spherical cap model (section 3.3) and the sphere to sphere model (section 3.4). The key feature of these models is that they allow for surface induced nucleation as observed in our simulation.

3.2 Spherical Cap Model

A simple model that includes surface effects during nucleation is the "spherical cap" model (hereafter referred to as *Scap model*). This model was used to study surface melting, nonmelting in nanoparticles[50] and the melting of supported metal nanopartcles[51], but it has not been used to directly study the nucleation barrier as a function of size, n, which is the usual reaction coordinate for nucleation.

This model relates the fraction of the solid embryo wetted by the liquid to the surface fraction of the spherical cap. The solid embryo is characterized by the height of the spherical cap, h (See fig.3.1). The cluster is entirely liquid when $h = 0$ and entirely solid when $h = 2R$, where R is the radius of the cluster. We aim to characterize our free energy barrier in terms of the number of molecules in the solid

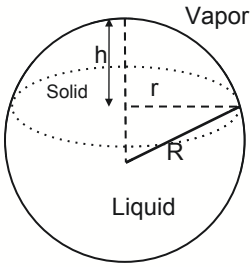

Figure 3.1: A geometric sketch of the spherical cap model r is the radius of the base of the cap.

phase, so it is intuitive to relate the volume of the embryo to that of the morphology of the model. Using the conservation of mass and assuming that there is no change in density upon freezing, we obtain R as a function of the total number of particles N in the cluster as:

$$V_{total} = \frac{4}{3}\pi R^3 = Nv, \tag{3.2}$$

where, V_{total} is the total volume of the cluster. Using the equality on the RHS of eqn. 3.2 gives

$$R = \left[\frac{3Nv}{4\pi}\right]^{1/3}. \tag{3.3}$$

The volume per particle in the liquid phase, v_l, and the volume per particle in the solid phase, v_s are the same, i.e $v_l = v_s = v$. The volume of the solid embryo within the liquid is given as the volume of the spherical cap,

$$V_{cap} = \frac{1}{3}\pi h^2(3R - h) = nv, \tag{3.4}$$

where n is the number of solid particles. Solving the resulting cubic equation in h,

$$\pi h^3 - 3\pi R h^2 + 3nv = 0, \tag{3.5}$$

we obtained three real roots, h_1, h_2 and h_3, valid over the following ranges; $h_1 < 0$, $0 < h_2 < 2R$, and $h_3 > 2R$ respectively. A plot of the different roots for a cluster of $N = 456$ (see fig. 3.2), shows that the roots satisfying the second condition depicts the physical meaning of h. We therefore use this as a function of the number of particles $h(n)$ in the solid phase. The spherical section of the cap gives the solid-vapor interface and using $h(n)$, we obtain its area as:

$$A_{sv}(n) = 2\pi R h(n), \tag{3.6}$$

while the solid-liquid interface is the base of the spherical cap (see fig.3.1). Its area, $A_{sl}(n)$ is

$$A_{sl}(n) = \pi r^2. \tag{3.7}$$

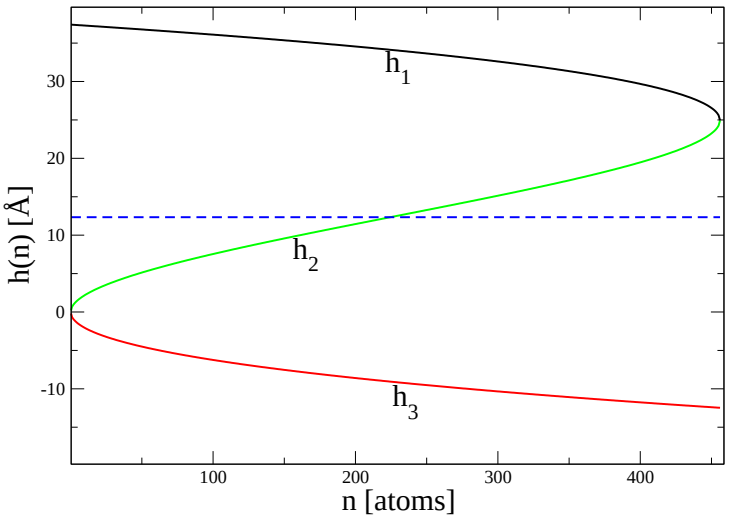

Figure 3.2: Different roots obtained from eqn. 3.5 for a 456-atom cluster using $v = 17.27$ $\mathring{A}$. The plot is the heights of the spherical cap as a function of embryo size.

Using Pythagoras, $r^2 = 2Rh - h^2$, in eqn.3.7 gives

$$A_{sl}(n) = \pi(2Rh(n) - h(n)^2). \tag{3.8}$$

Substituting these surface areas into eqn. 3.1 gives

$$\Delta G(n) = n\Delta\mu + A_{sv}(n)(\sigma_{sv} - \sigma_{lv}) + A_{sl}(n)\sigma_{sl}, \tag{3.9}$$

where we note that the area of the liquid-vapor surface lost as the embryo grows is the same as that gained by the solid-vapor surface. This is the basic model which we shall henceforth refer to as $Scap-1$ in the rest of this work. Our model considers the solid-vapor and liquid-vapor surfaces to be curve portions of a sphere whereas the solid-vapor and liquid-vapor surface tension used are the bulk planar values [52]. More so, at small sizes (2R$\sim$ 100 nm), the correction due to surface curvature [18, 53] is inversely proportional to the radius curvature. The curvature corrected

surface tension is $\sigma_c = \sigma_f(1 - \frac{2\delta}{R})$, where σ_f is the planar surafce tension and δ is the Tolman length[53]. Introducing this correction to the solid-vapor and the liquid-vapor surface tensions, and assuming the Tolman lengths to be equal, yields a second model $Scap-2$, with δ as an additional fit parameter.

$$\Delta G(n) = \Delta\mu n + A_{sv}(n)(\sigma_{sv} - \sigma_{lv})(1 - \frac{2\delta}{R}) + A_{sl}(n)\sigma_{sl}. \tag{3.10}$$

A new physical phenomenon becomes important in the case of surface nucleation in nanosystems associated with the presence of a three phase contact line and its line tension, τ. The line tension is the energy required to increase the length of the three phase contact line as the embryo grows. Auer *et al*[25], found that line tension and its curvature correction play a significant role in the energy barrier during heterogeneous nucleation. Introducing this term gives us a third model, $Scap-3$,

$$\Delta G(n) = \Delta\mu n + A_{sv}(n)(\sigma_{sv} - \sigma_{lv}) + A_{sl}(n)\sigma_{sl} + L_{slv}(n)\tau, \tag{3.11}$$

where $L_{slv}(n)$ is the length of the three phase contact line,

$$L_{slv}(n) = 2\pi r = 2\pi\sqrt{(2Rh(n) - h(n)^2)}. \tag{3.12}$$

Though, the surface-curvature correction and the line tension both go as $n^{1/3}$, they have different n dependencies in the geometric prefactors. Therefore, to understand the combined effect of all the corrections, we obtained a full model termed $Scap-4$ to be

$$\Delta G(n) = \Delta\mu n + A_{sv}(n)(\sigma_{sv} - \sigma_{lv})(1 - \frac{2\delta}{R}) + A_{sl}(n)\sigma_{sl} + L_{slv}n(n)\tau. \tag{3.13}$$

Eqns 3.9, 3.10, 3.11 and 3.13 are fitted in section 3.5 to free energy data obtained from simulations in order to understand the individual or combined effect of the surface terms on the free energy barrier to freezing in nanoparticles.

3.3 Modified Spherical Cap Model

The contact angle, which is the angle that the embryo makes between the vapor phase and the metastable mother phase, represents a state of mechanical equilibrium determined by a balance between the three interfacial tensions: the solid-vapor

surface tension, σ_{sv}, the liquid-vapor surface tension, σ_{lv}, and the solid-liquid interfacial tension, σ_{sl}, (see fig. 3.3). Since the early works of Thomas Young[54] and J. W. Gibbs[14], numerous experiments and theories have been put forward to relate the contact angle and the wetting propensity of materials. The relationship between the contact angle, Φ, and the surface tensions for a liquid droplet on a flat surface, is given by Young's equation,

$$\sigma_{lv} \cos \Phi = \sigma_{sv} - \sigma_{sl} \tag{3.14}$$

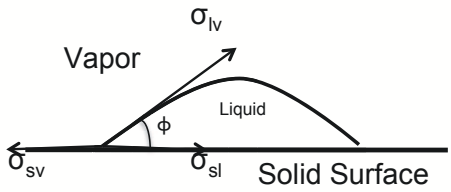

Figure 3.3: Schematic drawing of a liquid droplet forming heterogeneously on a flat solid surface.

The liquid totally wets the solid surface (see fig. 3.3), when the contact angle, Φ, equals to zero. When $\Phi = \pi$, this corresponds to a non-wetting or drying condition. Partial wetting occurs when $0 < \Phi < \pi$.

The *Scap* model, which is based on the requirement of partial wetting as suggested by Dikaev[5] and observed in simulation experiment, has a contact angle that is dependent on the number of solid particles in the embryo. The wettability from this model is based on the condition set forth in ref. [5]. Xu *et al* [55] proposed a nucleation model for melting and freezing in Ge nano-crystals, (NCs), embedded in silica which considers the contact angle. Their deduction that $\theta = \frac{\pi}{2}$ (cf. eqn.5 of ref[55]) is only a coincidence which may be attributed to the properties of the system studied. Caupin[56] generalized the spherical cap model to include the case of an arbitrary contact angle to study the equilibrium melting temperature in embedded NCs using the contact angle as the only independent parameter without the effect of the line tension on the wettability of the solid phase. To study the wettability in the partial wetting regime, we assume the embryo to form a spherical cap but

with the solid-liquid interface making an angle (contact angle) of α, with the solid-vapor interface. See fig. 3.4. Here, as in the spherical cap model, we assume that there is no change in the density upon freezing and therefore the spherical shape of the entire nano-droplet remains unchanged. Balancing the surface tensions at equilibrium gives a relationship between our contact angle and the surface tension analogous to Young's equation:

$$\sigma_{sl} \cos \alpha = \sigma_{lv} - \sigma_{sv} \ . \tag{3.15}$$

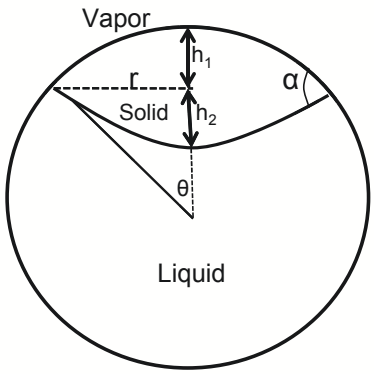

Figure 3.4: A geometric representation of the modified spherical cap model

To characterize the free energy by both the number of particles in the embryo and the contact angle, we need the different surface areas as functions of the number of particles, n and the contact angle α. From geometry (fig. 3.4) and trigonometry, the following relations are obtained:

$$r(\theta) = R \sin \theta, \tag{3.16}$$

$$h_{sv}(\theta) = R(1 - \cos \theta), \tag{3.17}$$

$$h_{sl}(\theta) = R[1 - \cos(\alpha - \theta)] \frac{\sin \theta}{\sin(\alpha - \theta)}. \tag{3.18}$$

The volume of the included lenticular shape is the sum of the volumes of the two spherical caps making the lens.

To relate the geometries to the number of molecules, we equate the volume of the lenticular shape, which is the sum of the volumes of the two spherical caps, to the volume of solid molecules (product of number of molecules and volume per molecules) in the included lens,

$$V_{lens} = \frac{\pi}{6} h_{sv}(\theta)[3r(\theta)^2 + h_{sv}(\theta)^2] + \frac{\pi}{6} h_{lv}(\theta)[3r(\theta)^2 + h_{lv}(\theta)^2] = n\nu. \tag{3.19}$$

Solving eqn. 3.19 for θ produces 20 roots, of which four real roots where obtained. Only one of these have a physical meaning, consistent with our model geometry. The plot of this solution with respect the contact angle, α, is shown in fig. 3.5.

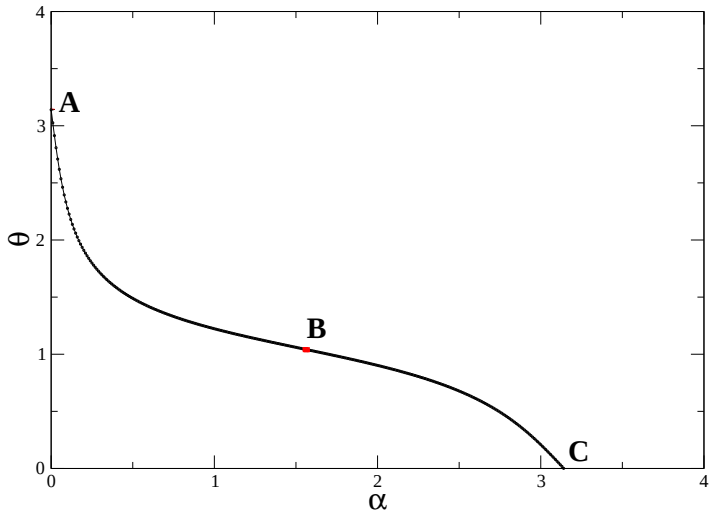

Figure 3.5: A plot of $\theta(n, \alpha)$ against α at $n = 100$, $v = 1.727 \times 10^{-29}/kT\ m^3$. When α approaches zero, θ approaches π and *vice versa*

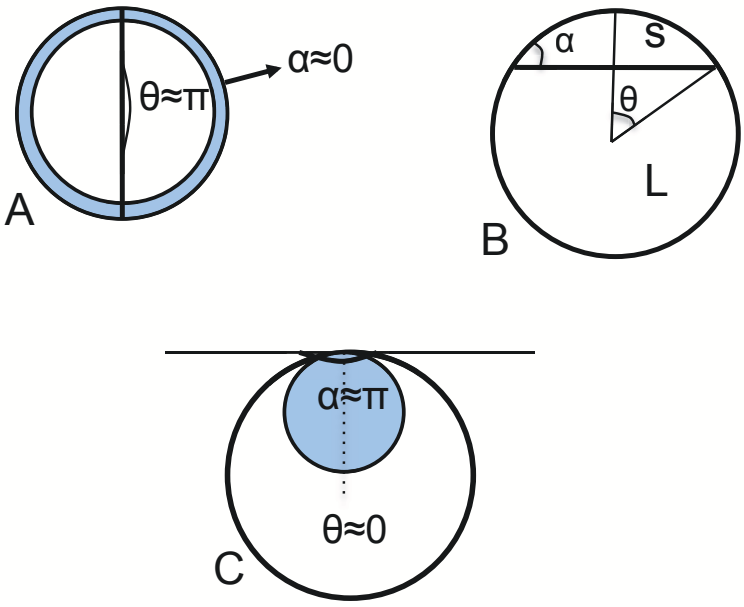

Figure 3.6: An illustration of the relationship between contact angle α and θ at showing different wetting conditions indicating the points A, B and C marked on fig. 3.5.

For complete wetting, $\alpha \approx \pi$, (point C),which corresponds to a state when the liquid forms an inclusion on the solid phase as indicated in fig. 3.6C. Non wetting occurs when $\alpha = 0$, (fig. 3.6A), while partial wetting occurs when $0 < \alpha < \pi$ corresponding to fig. 3.6B respectively . This condition for partial wetting corresponds to $\sigma_{sl} > \sigma_{sv} - \sigma_{lv}$ or $\sigma_{sl} > \sigma_{lv} - \sigma_{sv}$. This θ is a function of number of molecules, n, and the contact angle, α, *i.e.* $\theta(n, \alpha)$. Substituting $\theta(n, \alpha)$ into eqns. 3.16-3.18, we use $h_{sv}(n, \alpha)$, $h_{sl}(n, \alpha)$ and $r(n, \alpha)$ to find the different surface areas and the length of the three phase contact line,

$$A_{sv}(n, \alpha) = \pi[r(n, \alpha)^2 + h_{sv}(n, \alpha)^2], \tag{3.20}$$

$$A_{sl}(n, \alpha) = \pi[r(n, \alpha)^2 + h_{sl}(n, \alpha)^2], \tag{3.21}$$

$$L_{slv}(n, \alpha) = 2\pi r(n, \alpha). \tag{3.22}$$

The free energy expression for model $mscap - 1$ becomes,

$$\Delta G(n, \alpha) = \Delta\mu n + A_{sv}(n, \alpha)(\sigma_{sv} - \sigma_{lv}) + A_{sl}(n, \alpha)\sigma_{sl}. \tag{3.23}$$

We also introduce the correction due to surface curvature. The radii of curvature are different for the solid-liquid and solid-vapor interfaces as seen in fig. 3.4. R is the radius of curvature for the solid-vapor interface, while R' is the radius of curvature for the solid-liquid interface which is obtained by geometry and trigonometry as,

$$R' = \frac{R\sin\theta}{\sin(\alpha-\theta)}. \tag{3.24}$$

With this correction, our model expression $mscap-2$ becomes,

$$\Delta G(n) = \Delta\mu n + A_{sv}(n)(\sigma_{sv}-\sigma_{lv})(1-\frac{2\delta_{sv}}{R}) + A_{sl}(n)\sigma_{sl}(1-\frac{2\delta_{sl}}{R'}), \tag{3.25}$$

where δ_{sv} and δ_{sl} are the Tolman lengths on the solid-vapor and solid-liquid interfaces respectively.

In order to study the effect of the line tension contribution to our model, we introduced the line tension. The free energy expression now becomes, $mscap-3$,

$$\Delta G(n,\alpha) = \Delta\mu n + A_{sv}(n,\alpha)(\sigma_{sv}-\sigma_{lv}) + A_{sl}(n,\alpha)\sigma_{sl} + L_{slv}(n,\alpha)\tau. \tag{3.26}$$

3.4 Sphere to Sphere Model

Nucleation of the solid phase within a cluster can begin at any position in the cluster depending on the wetting propensity[57] of the material. For self-wetting materials such as Lennard-Jones liquids[9], metals[7] and to some degree silicon, the new phase is either totally wetted (core nucleation) or partially wetted (surface nucleation), while for non-self-wetting materials such as alkali metals[18, 57] only non-wetting is expected. To study freezing under these different scenerios, we make use of the "sphere to sphere" model. This model, which is similar to the cluster wetting model used by Cleveland *et al* [57] to study equilibrium coexistence in clusters, considers a spherical solid embryo of fixed volume and density (or volume per particle v_s) in contact with its liquid at fixed volume and density (or volume per particle v_l). See fig. 3.7. To allow for the different wetting regimes (total, partial and non wetting), we consider different positions of the solid-liquid coexistence ranging from a spherical inclusion of the embryo surrounded by a liquid shell (fig. 3.8a) to where the two spheres touching each other at a point (fig. 3.8c).

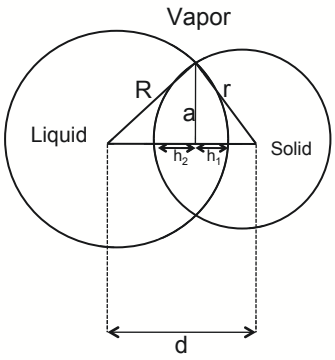

Figure 3.7: A geometric sketch of the sphere-sphere model, R is the radius of the liquid phase, r is the radius of the solid embryo, d is the distance between their centers of mass.

In considering this model, we neglect the interfacial free energy contribution from crystallographic anisotropies of the solid, but rather take the surface free energy as an average over these facets.

To obtain the expression for the free energy barrier, we characterize both the solid embryo and liquid cluster by their radii r and R respectively. We also use the distance between the geometric centers of the spheres representing the two spheres, d. Since the liquid cluster can assume the shape of indented sphere depending on the position of the solid cluster from it, we also characterize R as a function of d. In order to obtain the different surface areas which go into the free energy expression, we consider the region of coexistence which forms a lens shape. The volume of this lenticular shape is the sum of the volumes of the spherical caps belonging to the two spheres as seen in fig. 3.7.

$$\begin{aligned} V_{lens} &= V(R,h_1) + V(r,h_2) \\ &= \frac{(R+r-d)^2(d^2+2dr-3r^3+2dR+6rR-3R^2)}{12d}\,, \end{aligned} \tag{3.27}$$

where h_1 is the height of the spherical cap of the solid phase along the solid-liquid boundary, and h_2 is the height of the spherical cap belonging to the solid, (see fig. 3.7). To obtain R as a function of the number of solid particles and the distance d, we calculate the volume of the homogeneous liquid as

$$V_{liquid} = \frac{4\pi R^3}{3}. \tag{3.28}$$

Since the volume of the liquid phase and the solid phase in the lens shape region is

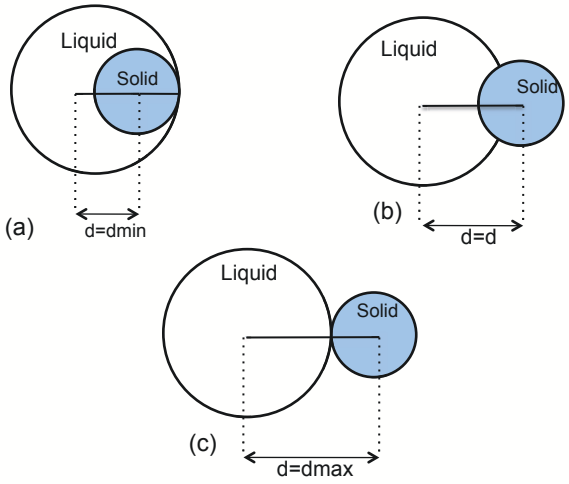

Figure 3.8: Different positions of the solid embryo from liquid phase corresponding to the different wetting conditions, (a) total wetting, (b) partial wetting and (c) nonwetting of the solid by the liquid.

contained within a sphere of radius R, the conservation of mass yields,

$$\frac{4\pi R^3}{3} - V_{lens} - (N-n)v_l = 0. \tag{3.29}$$

Solving this equation gives four roots (R_1, R_2, R_3 and R_4) with R_2 and R_4 being positive. These two roots possess an intriguing characteristic as one is real in the region where the other is imaginary. We therefore take a piecewise of these two positive solution to give the radius of the liquid cluster $R(n,d)$ as:

$$R(n,d) = \begin{cases} R_2(n,d) & R_2(n,d) \in \Re \\ R_4(n,d) & R_4(n,d) \in \Re \end{cases}$$

By geometry, the heights of the spherical caps, h_1, and h_2, which are also characterized by the number of solid particles, n, and the distance, d, are given as

$$h_1(n,d) = R(n,d) - d_1 = \frac{(r - R(n,d) + d)(r + R(n,d) - d)}{2d}, \tag{3.30}$$

and

$$h_2(n,d) = r - d_2 = \frac{(R(n,d) - r + d)(R(n,d) + r - d)}{2d}, \tag{3.31}$$

where $r = [\frac{3nv_s}{4\pi}]^{1/3}$ is the radius of the solid embryo. The interfacial areas which go into eqn. 3.1 are calculated from the areas of the spherical caps:

$$A_{sv} = 4\pi r^2 - 2\pi r h_2(n,d), \tag{3.32}$$

$$A_{lv} = 4\pi R(n,d)^2 - 2\pi R(n,d)h_1(n,d), \tag{3.33}$$

$$A_{sl} = 4\pi r^2 - 2\pi r h_2(n,d). \tag{3.34}$$

Putting these areas in eqn.3.1 and noting that

$$\Delta G(n,d) = G(n,d) - G(0,0), \tag{3.35}$$

and,

$$G(0,0) = A_0\sigma_{lv}, \tag{3.36}$$

where A_0 is the area of the entire liquid phase before the appearance of the solid embryo, the general equation for the model takes the form,

$$\Delta G(n,d) = \Delta\mu n + (A_{lv}(n,d) - A_0)\sigma_{lv} + A_{sv}(n,d)\sigma_{sv} + A_{sl}(n,d)\sigma_{sl}. \tag{3.37}$$

We find the limits for the distance between the geometric centers of the embryo and the whole cluster, d. d_{min}, for a given size, corresponds to d when the solid embryo is total embedded in the liquid cluster (see fig. 3.8a), while a corresponding d_{max} is the value of d when the two spheres just touch each other as shown in fig. 3.8c. d_{min} and d_{max} are both functions of the embryo size. Once the solid embryo is embedded in the liquid, *i.e.* $d < d_{min}$, the work of formation of an embryo is independent of the distance. Also, when $d > d_{max}$, there is no solution to eqn. 3.29, therefore the free energy function between these two limits is:

$$\Delta G(n,d) = \begin{cases} \Delta G(n,dmin) & d \leq dmin \\ \Delta G(n,d) & d = d \\ \Delta G(n,dmax) & d \geq dmax. \end{cases}$$

We also introduce the curvature correction involving δ_1 and δ_2, for the solid-vapor and solid-liquid surfaces respectively. This modifies our model into $sphere-2$,

$$\Delta G(n,d) = \Delta\mu n + (A_{lv}(n,d) - A_0)\sigma_{lv}(1 - \frac{2\delta_1}{R(n,d)}) + A_{sv}(n)\sigma_{sv}(1 - \frac{2\delta_2}{r}) + A_{sl}(n)\sigma_{sl}(1 - \frac{2\delta_2}{r}) \tag{3.38}$$

where we assume the same correction for both solid-vapor and liquid-vapor surface tensions.

We also consider the line tension correction, which according to Seppecher[58] is vital in the equilibrium of the forces of the embryo. The length of the three phase

contact line is the circumference of circular disc with radius a in fig. 3.7.

$$L_{slv}(n,d) = 2\pi a(n,d), \tag{3.39}$$

where

$$a(n,d) = \frac{1}{2d}\sqrt{4d^2R(n,d)^2 - (d^2 - r^2 + R(n,d)^2)^2}. \tag{3.40}$$

The model, $sphere-3$ with the line tension becomes

$$\Delta G(n,d) = \Delta\mu n + (A_{lv}(n,d) - A_0)\sigma_{lv} + A_{sv}(n,d)\sigma_{sv} + A_{sl}(n,d)\sigma_{sl} + L_{slv}(n,d)\tau. \tag{3.41}$$

3.5 Results

We present the results of the fitting of the different models to our simulation data. We use the bulk values of $\sigma_{sv} = 0.90\ J/m^2$ and $\sigma_{lv} = 0.74\ J/m^2$ calculated with the EAM potential[52]. The change in chemical potential, $\Delta\mu$, and the solid-liquid surface tension are used as fit parameters. The values of the line tension,τ, and the curvature correction to the bulk surface tension, δ, are also extracted from the fitting. We use a simple least squares fit in the "Mathematica" software to obtain the fit parameters. For each fit, we calculate the normalized residual as a measure of how good the fit is in comparison to the data. The normalized residual, R_{norm}, is

$$R_{norm} = \sqrt{\sum_n \left(\Delta G(n)_{data} - \Delta G(n)_{fit}\right)^2}. \tag{3.42}$$

3.5.1 Spherical Cap Model

Fitting $Scap-1$, $Scap-2$, and $Scap-3$ to our free energy at 710K for 456 atoms cluster and at 700K for 276 atoms cluster all produce negative solid-liquid surface tensions. Table 3.1 shows the fit parameters obtained at 710K for 456 atoms clusters while table 4.3 show same parameters for 276 atoms clusters at 700K. The introduction of the curvature (δ_{sv} and δ_{lv}) improves the fits as can be seen in fig. 3.21 and fig. 3.10 and reduces the residuals to 2.889 and 2.1924 respectively. With the introduction of the line tension, the fits are further improved with a corresponding reduction in the residuals (see fig. 3.21 and fig. 3.10). The improvements observed in models $Scap-2$ and $Scap-3$ are expected, especially at smaller embryo sizes. This

is due to the fact that both the radius of curvature and the length of the three phase contact line go as a third of the embryo, *i.e* $L_{slv} \sim n^{1/3}$, and therefore dominate at smaller sizes.

Table 3.1: The fit parameters obtained by fitting the different versions of Scap model to simulation data at T = 710K for a 456-atom cluster.

models	$\Delta\mu(k_BT)$	σ_{sl} J/m^2	$\tau(10^{-12}J/m)$	$\delta_{sv}(\mathring{A})$	$\delta_{lv}(\mathring{A})$	res.
Scap-1	-0.467	-0.0924	-	-	-	3.5641
Scap-2	-1.084	-0.417	-	-1.156	1.406	2.889
Scap-3	-0.395	-0.12733	1.163	-	-	1.32339
Scap-4	0.147	0.138	1.885	1.09	-1.328	0.8482

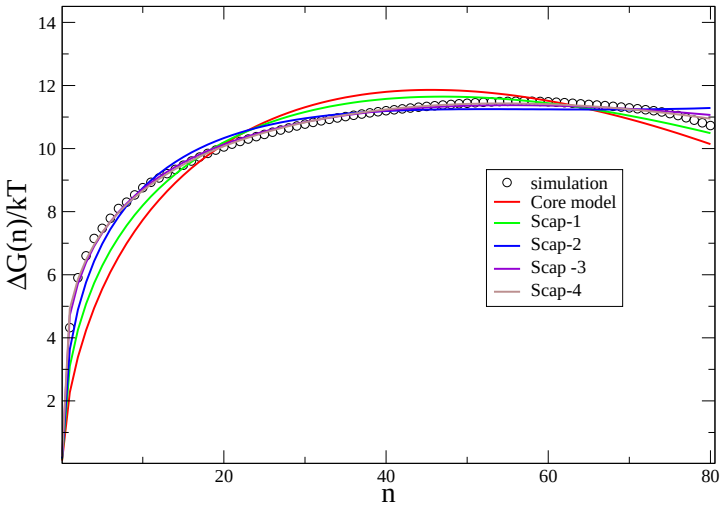

Figure 3.9: A fit of *Scap* model (with all the corrections) to the calculated free energies for a 456-atom cluster at $T = 710K$.

With the introduction of both the curvature correction and line tension, a fit of $Scap-4$ to the data improves the fit (cf fig. 3.21) and reduces the residual to further lower value of 0.6552. The values of the fit parameters are $\Delta\mu = 0.147\ kT$, $\sigma_{sl} = 0.138\ J/m^2$, $\tau = 1.88 \times 10^{-12}\ J/m$, $\delta_{sv} = 1.09 \times 10^{-10}\ m$ and $\delta_{lv} = -1.328 \times 10^{-10}\ m$

Table 3.2: The fit parameters obtained by fitting the different versions of Scap model to simulation data at T = 700K for a 276-atom cluster.

models	$\Delta\mu(k_BT)$	σ_{sl} J/m^2	$\tau(10^{-12}J/m)$	$\delta_{sv}(\mathring{A})$	$\delta_{lv}(\mathring{A})$	res.
Scap-1	-0.525	-0.0865	-	-	-	2.4145
Scap-2	-0.710	-0.1586	-	-0.2249	0.2736	2.1924
Scap-3	-0.490	-0.108	0.707	-	-	1.474
Scap-4	0.1227	0.0805	1.713	1.09	0.6849	0.8339

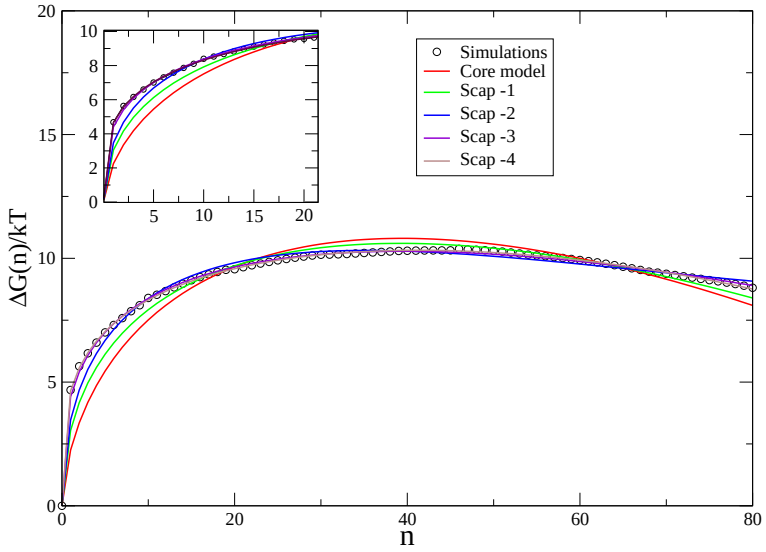

Figure 3.10: Fits of *Scap* models to the calculated free energies for a 276-atom cluster at $T = 700K$. Inset: Shows the fits at smaller embryo size.

were obtained. In all the cases, the residual decreases from $Scap-1$ to $Scap-4$.

Despite the good fits and low values of the residuals, the negative σ_{sl} obtain from $Scap-1$, $Scap-2$ and $Scap-3$ is very unlikely as this will result in a spontaneous increase of the interface thereby causing disintegration of the droplet. It is possible that the fit parameters we have are not those at the global minimum. To eliminate this possibility, we employ a more rigorous method of minimization though the use of the Lipschitz Global Optimizer (LGO)[59]. A comparison of residuals of the two methods show that our initial fits were close to, but not at the global minimum of the fit. However, the trend remains the same (see table 3.3).

Table 3.3: The fit parameters obtained by fitting the different versions of Scap model to simulation data at T = 710K for 456 atoms cluster using the LGO.

models	$\Delta\mu(k_BT)$	σ_{sl} J/m^2	$\tau(10^{-12}J/m)$	$\delta_{sv}(\mathring{A})$	$\delta_{lv}(\mathring{A})$	res.
Scap-1	-0.4665	-0.0924	-	-	-	3.4244
Scap-2	-0.4534	-0.0854	-	0.3665	0.3857	3.4586
Scap-3	-0.3947	-0.1273	1.16	-	-	1.3233
Scap-4	0.2271	0.1543	1.713	1.3104	-1.034	0.339

The fitting of $scap-4$ produces a positive σ_{sl}, but also a positive change in chemical potential, $\Delta\mu$. This too, is unphysical, as this means that work is done in moving an atom from metastable phase into the stable solid phase. In the $Scap$ model, we assume the sold-liquid interface to be flat with the contact angle between the solid-vapor and solid-liquid interfaces depending on the number of the solid-like atoms inside the embryo. Based on the early work of Young[54], experimental[60] and theoretical[61] works have shown that for a homogeneous system at equilibrium, there is an associated contact angle which is independent of the size of the embryo, hence we introduce the "Modified Scap" model.

3.5.2 Modified Spherical Cap Model

As a preliminary study into the behavior of this model, we select some arbitrary values of $\Delta\mu = -0.20\ kT$ and $\sigma_{sl} = 0.22\ J/m^2$, and make a contour plot of the free energy expression (eqn. 3.23). From fig. 3.11, we see a minimum in the free energy

surface corresponding to a constant contact angle for all $n - sized$ embryo. This supports the concept of an equilibrium contact angle, derived from thermodynamics, which is independent of system size[60, 61, 62].

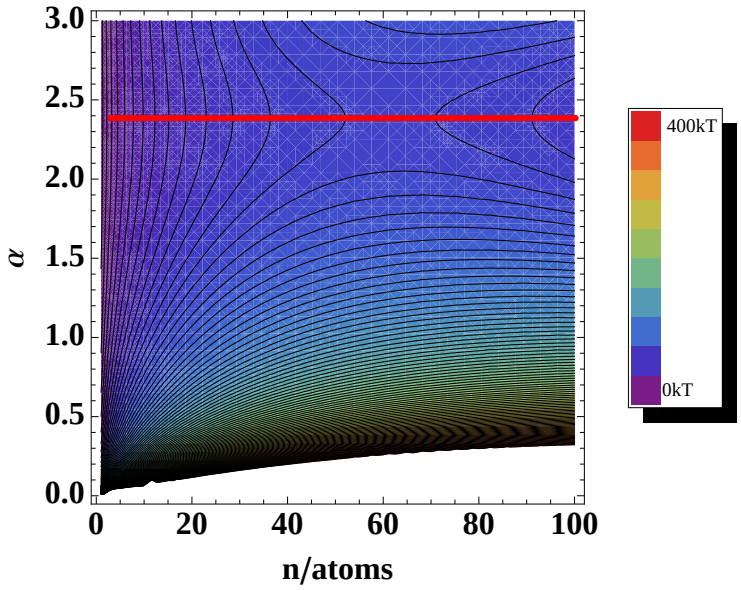

Figure 3.11: A free energy surface showing a constant contact angle independent of the embryo size.

With σ_{sv} and σ_{lv} assuming their bulk values, we make a plot of the contact angle, α, at which the minimum occurs on the free energy surface as a function of σ_{sl}. Fig. 3.12 is a plot of α for different σ_{sl} along free energy minimum using eqn. 3.23. We expect the contact angle obtained from thermodynamics to be the same as that obtained from a balance of forces, (i.e mechanical equilibrium), from eqn. 3.15. This plot shows that prior to the threshold value of σ_{sl}, the equilibrium contact angle is constant and equal to π which corresponds to complete wetting. Using the above values of σ_{sv} and σ_{lv}, the threshold corresponds to $\sigma_{sl} = \sigma_{sv} - \sigma_{lv} = 0.16\ J/m^2$. For σ_{sl} greater than this, we see a decrease in α signifying the onset of partial wetting.

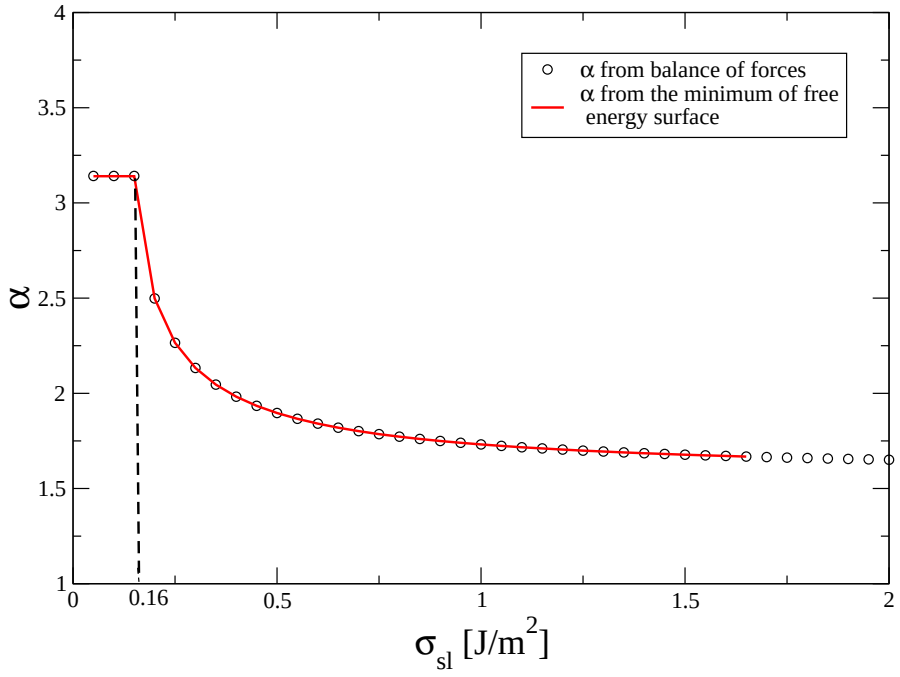

Figure 3.12: A plot of α both from the minimum of the free energy surface and from the balance of surface tensions showing the total wetting and the partial wetting regions.

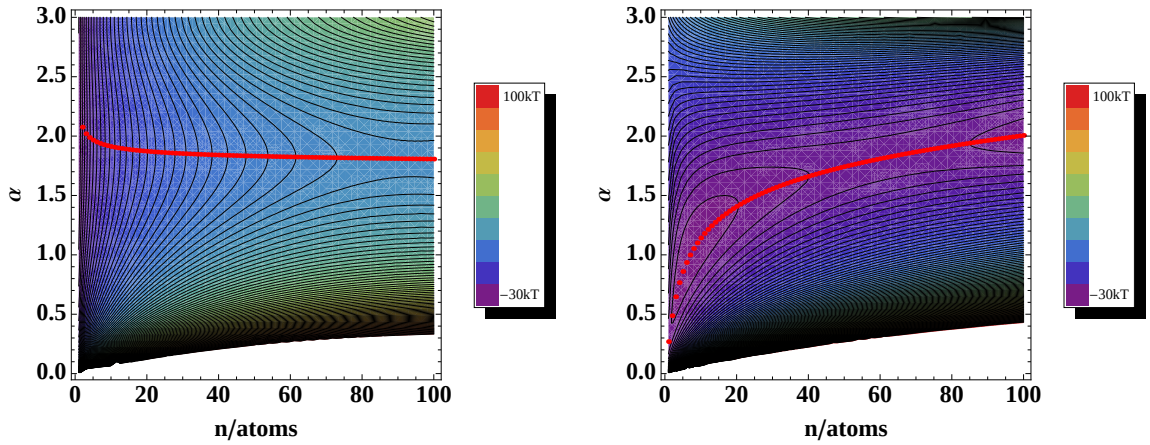

Figure 3.13: Free energy surfaces showing size dependence of the contact angle upon introduction of the line tension effect. Left: The effect of a positive line tension on the contact angle. Right: The effect of a negative line tension on the contact angle.

The line tension contribution to the equilibrium contact angle based on the mechanical balance of the different surface free energy, is inversly proportional to the radius, r, of the three phase contact line[62, 63]. When introduced into the free energy expression, it alters the equilibrium condition of the system causing α to become size dependent[62]. Fig. 3.13 left, shows a free energy surface at chosen values of $\Delta\mu = -2.3\ kT$, $\sigma_{sl} = 0.84\ J/m^2$ and $\tau = 5.0 \times 10^{-12}\ J/m$. At small embryo sizes, the effect of the line tension is large and it attempts to minimize the length of the three phase contact line for a positive line tension. This causes an increase in the contact angle for a fix number of solid-like atoms, relative to the system with no line tension. As n increases, this effect reduces causing a decrease in the contact angle and it approaches the equilibrium contact angle. We chose a negative line tension to see its effect on the contact angle and the free energy surface. Using $\Delta\mu = 0.60\ kT$, $\sigma_{sl} = 0.16\ J/m^2$ and $\tau = -1.5 \times 10^{-12}\ J/m$, we obtained fig. 3.13 (right). Though the effect of negative line tension is opposite that of the positive line tension, we see a very small contact angle at the τ we chose. The negative τ stretches the lenticular shape (see fig. 3.4) outward increasing the length of the three phase contact line. As the embryo increases in size, this effect is reduced resulting in a rapid increase in the contact angle.

We note that this change in contact angle would have some effect on the solid-liquid and solid-vapor surface areas and on the length of the three phase contact line. Fig. 3.14 is the linear plot of the solid-vapor and solid-liquid surface areas along the minimum in fig. 3.13 left (*i.e* using the α along the minimum). A plot of the solid-vapor and solid-liquid surface areas using α from fig. 3.13 right is shown in fig. 3.15. These plots are based on the expectation that the surface area of an embryo is proportional to $n^{2/3}$. Although the areas seems to be linear in $n^{2/3}$, we see a change in slope in all the areas as the embryo size increase. Fig. 3.16 shows a linear plot of the three phase contact line for both the positive and negative line tensions. In both cases, we observe a change in the slope, though more significant for the negative line tension.

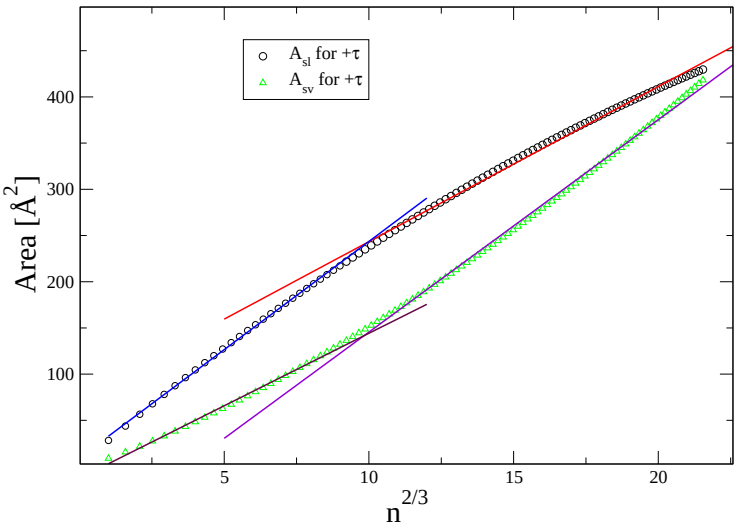

Figure 3.14: A linear plots of the solid-vapor and solid-liquid surface areas for a chosen positive line tension of $\tau = 5.0 \times 10^{-12}\ J/m$.

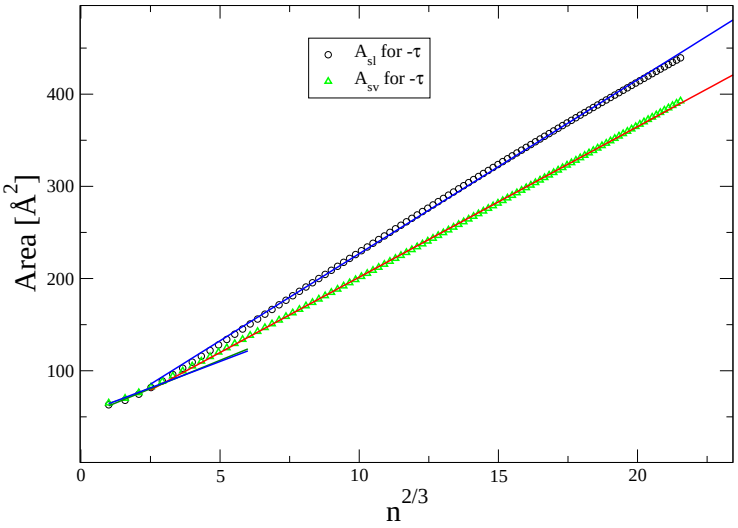

Figure 3.15: A linear plots of the solid-vapor and solid-liquid surface areas for a chosen negative line tension of $\tau = -1.5 \times 10^{-11}\ J/m$.

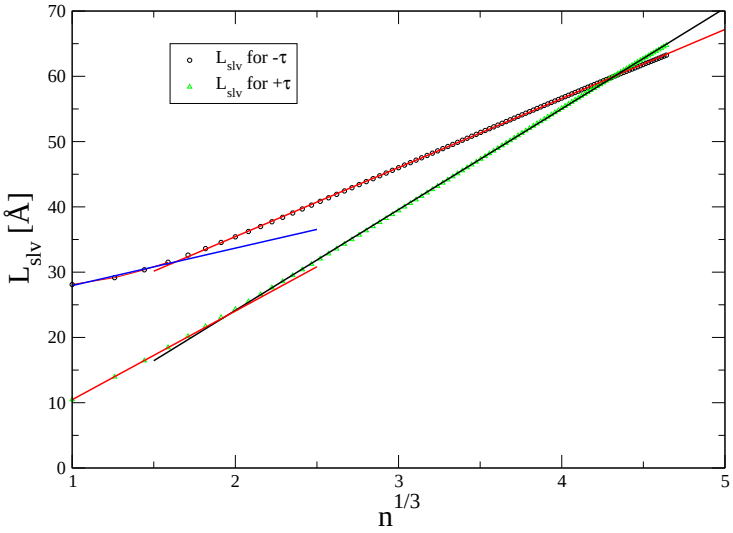

Figure 3.16: A linear plots of the length of the three phase contact line along the minima in fig. 3.13.

To obtain an optimal σ_{sl} by fitting the model to our free energy data, we make use of eqn. 3.15 which results in $\alpha = arccos[(\sigma_{lv} - \sigma_{sv})/\sigma_{sl}$. Introducing the line tension into eqn. 3.15 leads to a complicated relationship which cannot be explicitly solved. As a result of this, we have been unable to obtain numerical fits of this model to our simulation data.

3.5.3 Sphere to Sphere Model

Again, we begin by studying the general features of the sphere-to-sphere model by choosing the solid-liquid surface tension to represent the different wetting regions. Fig. 3.17 shows the free energy contour plots obtained from eqn. 3.37 using $\sigma_{sl} = 0.05\ J/m^2$ (left) and $\sigma_{sl} = 1.65\ J/m^2$ (right), which represent the conditions for total wetting and non wetting respectively. In fig. 3.17 left, we see that the nucleation barrier is lowest, and independent of d, when $d < d_{min}$ and the embryo is contained completely within the liquid phase (red line). In fig. 3.17 right, the minimum free energy barrier occurs at the position of the $d = d_{max}$. It should be noted that beyond d_{max}, the solid and liquid phases stands separated, therefore, the region beyond the

line d_{max} (red) in fig. 3.17(right) is unphysical and can be regarded as numerical noise. With $\sigma_{sv} = 0.18\ Jm^{-2}$, as suggested by the partial wetting condition, we obtained fig. 3.18. There is now a free energy "channel" with the minimum occurring beyond $d_{min} < d < d_{max}$, showing that the embryo prefers to sit in the liquid-vapor interface. Furthermore, a plot of the free energy along the minimum, using the same parameters, but changing the surface free energies gives fig. 3.19 which shows a higher free energy barrier increase with the surface free energy. The sharp rise of these curves at $n < 20$ is a characteristic of the free energies obtained from simulation.

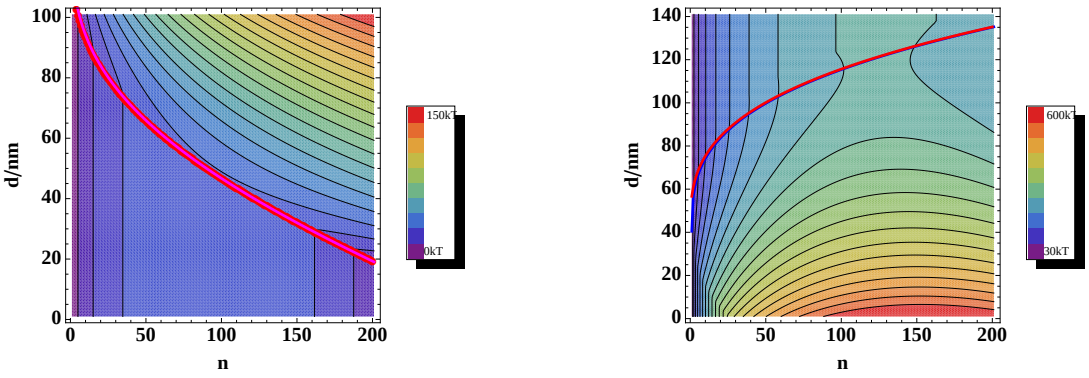

Figure 3.17: Contour plots using surface tension that represent total wetting (left) and non wetting conditions (right).

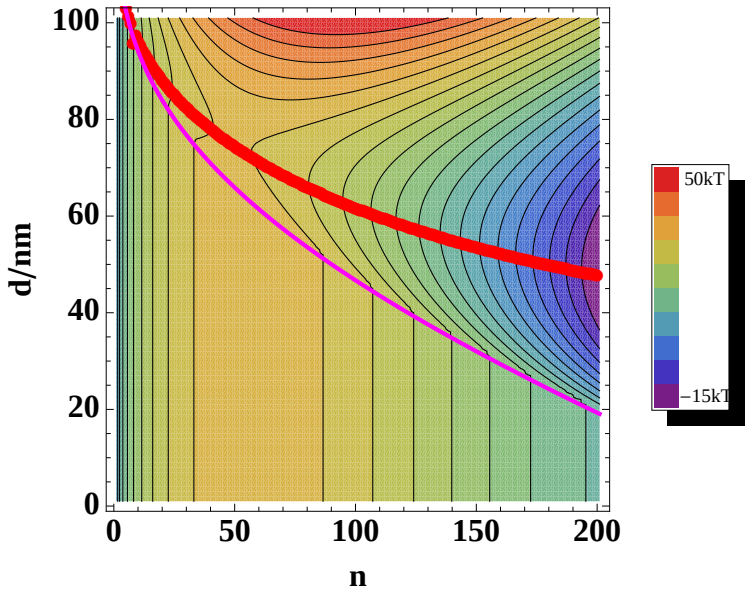

Figure 3.18: A contour plot using a partial wetting surface tension of $\sigma_{sl} = 0.18 Jm^{-2}$

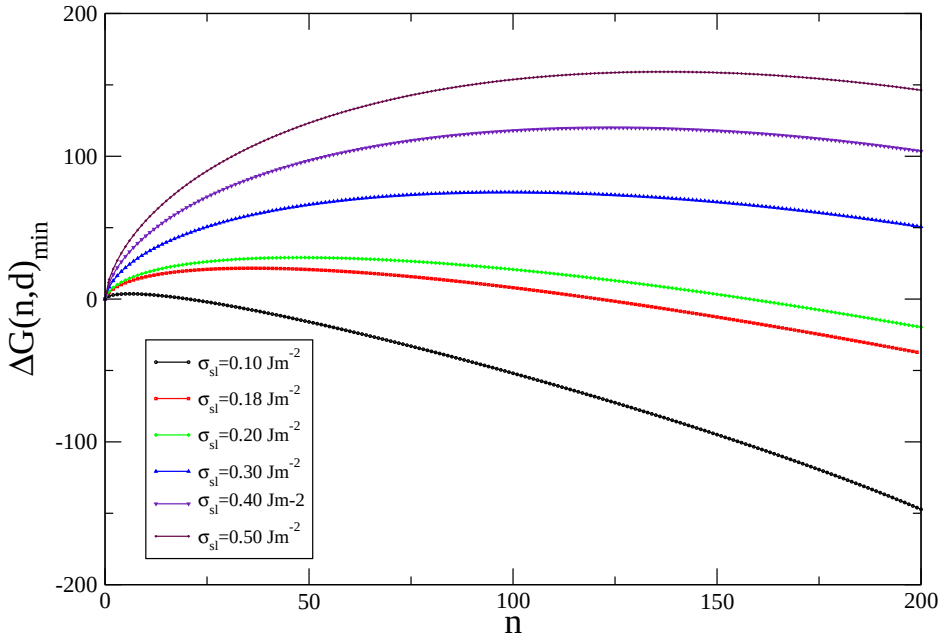

Figure 3.19: A plot of $\Delta G(n, d)$ along the minimum at chosen $\Delta\mu$ and diffrent value of σ_{sl}.

Making a fit of the model to our two dimensional free energy data at $T = 650K$, i.e eqn. 3.37, we obtain $\Delta\mu = -1.0312\ kT$ and $\sigma_{sl} = 0.161\ J/m^2$. With the line tension correction, we obtain $\Delta\mu = -0.592\ kT$, $\sigma_{sl} = 0.112\ J/m^2$ and $\tau = -4.9\times10^{-12}\ J/m$.

Due to the nature of the minimizing function with lots of local minima, we can not guarantee that these parameters are those at global minimum. To further search for a global minimum, we use different starting point for the search, but these result in the same fit parameters. Fig. 3.20 (left and right) shows the contour plot of the fits without and with the line tension correction respectively. We notice that along the free energy minimum, the contours for the fits bear a qualitative resemblance of the data shown in fig. 3.21. Fitting along this minimum should give us a better understanding as this is the more favorable path to nucleation.

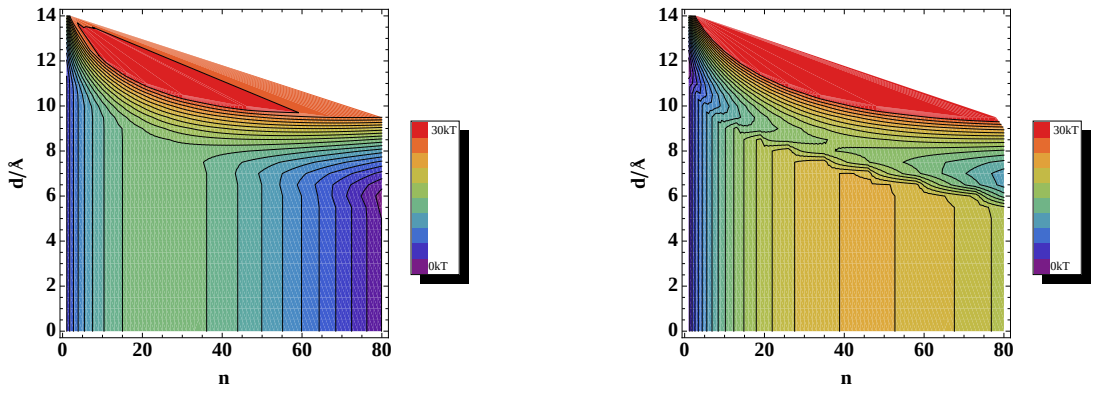

Figure 3.20: A two dimensional fitting to 2 two dimensional free energy surface. Left: A contour plot of the fit of the model to free energy surface at $T = 650K$ without any correction. Right: A contour plot of the fit at $T = 650K$ with the line tension correction.

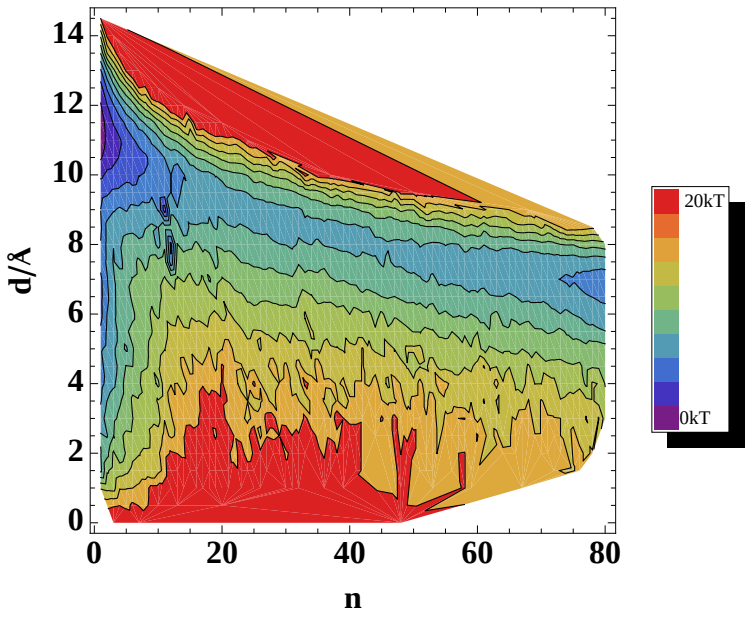

Figure 3.21: Free energy surface at $T = 650K$ calculated from simulations.

A fit along the minimum path at $T = 710K$ produces $\Delta\mu = -0.142$ and $\sigma_{sl} = 0.0709$ which is lower than that obtained from the two dimensional fitting. As can be seen in fig. 3.22, this is not a very good fit and has a high residual of 5.6906. Fig. 3.23 is a plot of all the solid-liquid surface tensions obtained from the fit along the minimum of the free energy surface against temperature. Despite the low values of the solid-liquid surface tensions and relatively high residuals, there is a linear dependence of the surface tension on temperature with $d\sigma_{sl}/dt = -6.276 \times 10^{-5}\ J/m.K$ which compares closely with that reported in ref.[64].

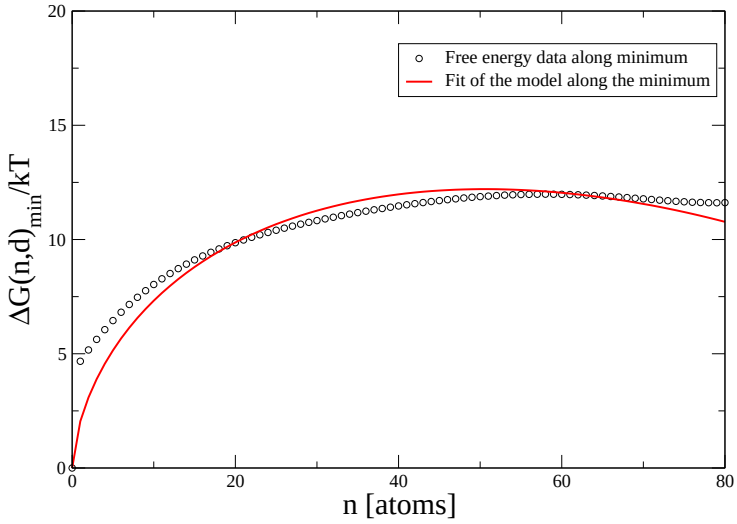

Figure 3.22: A fit of the model to data along the free energy minimum at $T = 710$.

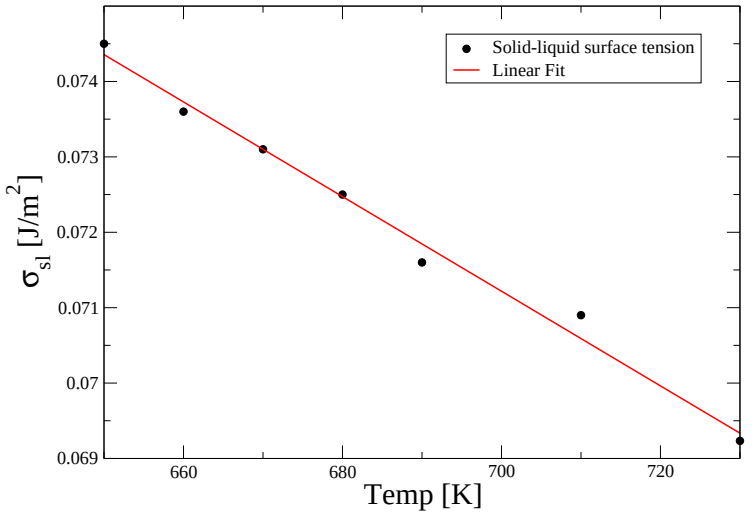

Figure 3.23: A plot of the solid-liquid surface tension obtained by a fit of the model along the minimum showing a an inverse relationship between the surface free energy and temperature.

3.6 Discussions

In using the *Scap* model to study surface nucleation, we assume that the solid-liquid interface is rigid and flat. With this assumption, we see good fits to the data when the line tension was introduced, as evidenced by low residuals of the data fits. But the unphysical parameters we obtain suggest that the assumption of flat interface may not be correct.

The *Mscap* model provides a more realistic description of the embryo geometry by allowing the solid-liquid interface to become curved. While the solid-vapor interface always remains concave, for a fixed n, the solid-liquid interface can be convex when the contact angle, α, is large and concave as α becomes small. For a given σ_{sl}, the contour plot of the free energy as a function of n and α slows that the free energy minimum at a value of α that is independent of n, which is characteristic of the equilibrium thermodynamic definition of a contact angle. Plotting the equilibrium contact angle as a function of σ_{sl}, shows that the model should exhibit a transition between complete wetting and partial wetting at $\sigma_{sl} = 0.16 J.m^2$. The evaluation of the mechanical equilibrium of the surface tensions for this model gives the same result.

As noted by Schimmele *et al*[50] and Yang[60], the effect of line tension on the equilibrium contact angle is large at small system size due to the line tension correction which goes as $1/r$. This inverse relationship introduces a size dependent contact angle when the line tension is considered. The effect of the sign of the line tension gives an explanation for the different curvatures that the solid-liquid interface can take. In general, a positive line tension drives the system to shorten the length of the three phase contact line which for a constant, small n, drives the embryo to adopt a more convex shape with $\alpha > \pi/2$. A negative line tension tends to increase the length of the three phase contact line. Figs. 3.14 and 3.15 suggest that these considerations can have a large influence on the shape adopted by the growing embryo. In the case of a negative line tension, the embryo expands along the solid-vapor interface stretching the solid-liquid interface to form a concave curvature with a smaller α, especially at small embryo size ($n < 10$). As the embryo size increases, there is

a change from the concave solid-liquid interface to form a convex curvature. This is evident in the pronounced change in the solid-liquid and solid-vapor surface areas and also in the length of the three phase contact line. In both cases of positive and negative line tensions, the solid-liquid interface grows faster as a function of n than the solid-vapor surface area, for small n. In the case of a negative τ, the solid-liquid interfacial area is only equal to solid-vapor area in the region $n \leq 5$, where due to the small α, both interfaces are nearly equal as the embryo forms a thin lunar shape. It should be noted that these two cases still belong to the partial wetting regime and both positive and negative line tensions have been reported in literature[25].

The sphere to sphere model also provides a good representation of the partial wetting phenomena in nanoparticles. In particular, the contour plot of the free energy as a function of n and d closely resembles fig. 2.12, obtained from our simulations. Fitting of the model to these simulation data produces reasonable values for σ_{sl} which are consistent with partial wetting. Including the line tension correction produces a negative tension. This negative line tension fit may help to explain why at small size, a high ratio of the solid-like atoms are found on the surface[7, 47].

Qualitatively, these phenomenological models, except the spherical cap model, can be used to study surface nucleation since they allow for both total and partial wetting conditions. For future work, we aim to obtain a quantitative fit of the $Mscap$ model to our simulation data.

Chapter 4

Semi Phenomenological Models

4.1 Motivation

Phenomenological models used in CNT need to make assumptions regarding the shape of the nuclei, and it is often that nuclei are spherical. The failure of the spherical models to explain the shape and height of the free energy barrier observed in experiments have led to several studies using phenomenological models with many different shapes[7, 55, 56, 57]. However it is still necessary to assume that the evolving embryo adopts a perfect geometrical shape whose areas can easily be computed using mathemathical relations.

Computer simulation experiments suggest that the shape of the embryo does not necessarily conform to any single geometrical shape, as seen in fig. 4.1. Our goal in this chapter is to obtain the surface areas and other geometric factors which contribute to the free energy barrier in such a way that is independent of the geometry of any formal shape. A key step in doing this is to define the surfaces, three phase contact line and radius of curvature at a molecular level, and measure their associated surface areas etc from simulations. One approach to achieve this is by dividing the space occupied by the atoms using Voronoi tessellations and then calculating the areas of these Voronoi cells. Voronoi diagrams have been used extensively in studying proteins[65, 66, 67], the analysis of local structure of solid materials[68], and in polymer technology[69, 70].

To implement our analysis, we take a given configuration obtained during the calculation of the free energy barrier in Chapter 2, and carry out the following:

- Identify all particles as liquid-like and solid-like according to the cluster criteria discussed in section 2.2.

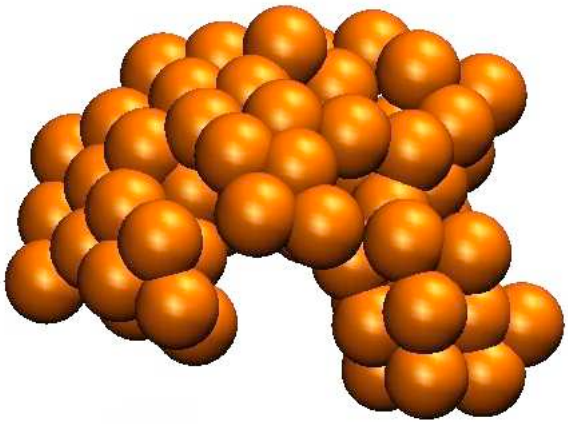

Figure 4.1: A snapshot of n_{max} embryo for 456 atom gold cluster, (taken from [47]).

- Identify the maximum embryo size using the cluster algorithm.
- Identify surface and bulk atoms using the cone algorithm put forward by Wang *et al*[71].
- Divide the space around the atoms into polyhedra by way of Voronoi tessellation.
- Define the solid-liquid interfaces as the plane of the Voronoi polyhedra shared between neighboring liquid-like and solid-like particles.
- Calculate the surface areas and other geometric parameters used in the free energy expression.

4.2 Surface and Core Atoms

In order to obtain the solid-vapor and liquid-vapor surface areas, we need to identify atoms on the surface and in the core of the cluster. We make use of the cone algorithm[71] in identifying the surface and bulk atoms. For a given particle, a *cone region* is define as the region inside a cone of side length, r_b, with azimuthal angle, θ, whose vertex rests on the particle center, (see fig. 4.3). An empty cone is a cone region with no other particle inside it. An atom is said to be a surface atom if there is at least one empty cone associated with it at any orientation, otherwise it is a

core atom. On the basis of earlier work[7, 47], we chose $r_b = 5.7$ $\mathring{A}$ and $\theta = \pi/3$. The solid atoms on the surface form the solid-vapor interface if they belong to the largest embryo while all the liquid-like atoms sitting on the surface form the liquid-vapor interface. In order to reduce the computer time used, we only probe atoms with less than 12 neighbors since a typical bulk atom within an FCC, Ih or BCC structure possesses at least 12 neighbors.

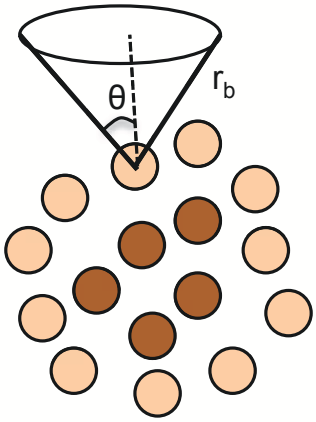

Figure 4.2: A cone defined by an azimuthal angle θ and a probe distance r_v, determines if an atom in a cluster belongs to a surface or core-like environment.

4.3 Voronoi Tessellation

A Voronoi diagram of a set of points is a collection of regions that divides up the volumes between the points. If $P = [p_1, p_2....p_m]$ be a set of m distinct points in real space, a Voronoi diagram of P is the subdivision of the space into m cells, one for each point with the property that a point q lies in the cell corresponding to the point p if and only if the Euclidean distance $d(q, p)$ satisfies the condition that $d(q, p_i) < d(q, p_j)$ for each $p_j \in P$ with $j \neq i$[72], *i.e.* the point q is closer to p_i than any other. The Voronoi cell is formed by a set of points called generating vertices formed by the intersection of planes between the particles. Each of these vertices corresponds to the circumcenter of a Delaunay sphere (circumsphere). A circumsphere is a sphere joining four closest particles and having no other particle center within it. Geometrically, the boundary of the Voronoi diagram is formed by

the planes that form the perpendicular bisector between the two adjacent points representing two neighboring particles. The normal to the plane is parallel to the vector separating the two particles sharing the plane.

In performing this tessellation, the efficiency and speed of the process depends on the number of neighbors that a chosen particle has. A large number of neighbors slows down the tessellation[73] and also produces *degeneracy* error[74], especially in a well ordered system. Degeneracy error occurs when more than three planes meet to form a generating vertex.

To avoid degeneracy error, and reduce the CPU time used in the Voronoi construction, we only consider the nearest neighbors to the chosen particle. This is done by setting a cutoff radius, r_{cut}, beyond which atoms are considered not to be neighbors. This can be done in two ways. In our first estimation of r_{cut}, we use the relationship between the number of particles, N and the size of simulation box: $r_{cut} = size/\sqrt[3]{N}$. This gives $r_{cut} = 3.07\mathring{A}$ for 276 atoms cluster and $r_{cut} = 2.67\mathring{A}$ for 456 atoms gold cluster. The second approach uses the radial distribution function, $g(r)$. To do this, we take 500 different configurations saved during the calculation of the free energy barrier and calculate their $g(r)$. We take the average over all the configurations. r_{cut} is taken as the radius corresponding to the minimum after the first peak in the radial distribution plot as shown in fig. 4.3. This method gives $r_{cut} = 3.7\mathring{A}$ for 276 atoms cluster , $r_{cut} = 3.8\mathring{A}$ for 456 atoms cluster and $r_{cut} = 1.54\ \sigma$ for Lennard-Jones.

The r_{cut} from the cluster size-box size relationship produces a number of neighbors not sufficient to construct the correct Voronoi cell around a particle. The r_{cut} from the $g(r)$ is optimal since it eliminates this error and no degeneracy errors are observed. We therefore use this second r_{cut} in our Voronoi constructions.

Using the Allen algorithm[74] for our tessellation, we take the following steps in our construction;

- For a given atom i, the distances of all other atoms from i are calculated. An atom j is a neighbor of i if the distance between i and j, d_{ij}, is less or equal to r_{cut}, *i.e*, $d_{ij} \leq r_{cut}$.
- The neighbors of i are sorted in order of their increasing distances from the atom i.

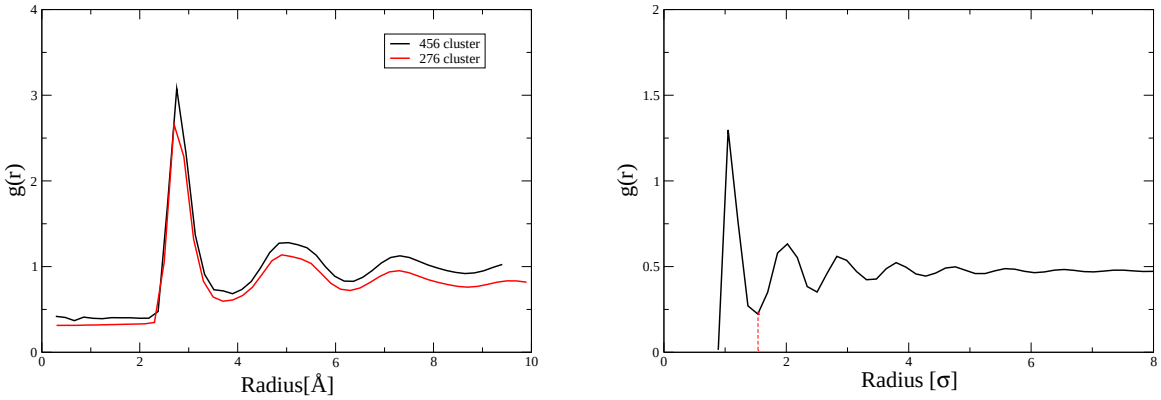

Figure 4.3: The radial distribution function, $g(r)$, used for the location of r_{cut}. Left: The $g(r)$ for 456 atoms cluster and 276 atoms cluster. Right: The $g(r)$ for Lennard-Jones bulk liquid.

- A plane is constructed between atoms i and j, using the midpoint between i and j and the normal vector which is parallel to **ij**. For atoms of different sizes, the plane divides the distance between the neighboring atoms in the ratio of their radii. Since our system has atoms of equal radii, the plane divides the distance, d_{ij}, into two equal parts with the coordinates of i acting as the origin of the plane. The plane is constructed using this midpoint and the vector between i and j as a normal vector $\hat{\mathbf{n}}$ to the required plane (see Appendix A).

- For three planes, l_{i1}, l_{i2}, l_{i3} associated with three atoms being neighbor with i, their point of intersection is obtained by solving the equation of planes simultaneously. This point of intersection corresponds to the center of the circumsphere joining atom i with its neighbors $j = 1, 2, 3$. This is the Voronoi vertex, v_i, as shown in fig. 4.4.

- All the vertices about atom i are joined together to form the Voronoi cell or a convex hull around the atom such that they form the vertices of the Voronoi planes between atom i and its neighbor j.

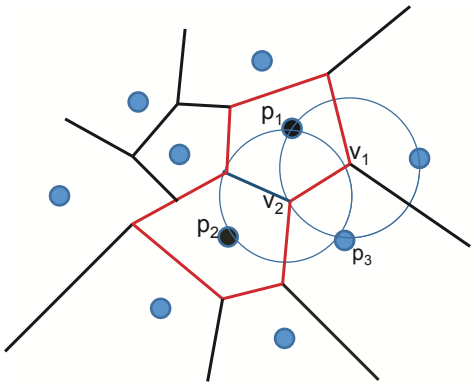

Figure 4.4: Schematic diagram showing the construction of Voronoi cell.

4.4 Calculation of Geometric Parameters

4.4.1 Interfacial Atoms and Interfacial Area

To calculate the solid-liquid interfacial area, it is pertinent to identify the interface. A solid atom is at the interface if it belongs to the largest embryo and has at least a neighbor that belongs to the liquid phase. We only consider atoms in the maximum embryo since we want to calculate the surface areas around the largest embryo. A network of Voronoi planes shared by two atoms identified to be in different phases forms the solid-liquid interface.

The area A_{pi}, of each of the interfacial planes is the sum of all the triangles which the plane can be decomposed[75]:

$$A_{pi} = 1/2 \sum_{i} |(\mathbf{V_{i+1}} - \mathbf{V_i})(\mathbf{V_i} - \mathbf{V_1})|, \tag{4.1}$$

where $\mathbf{V_i}$ is a vector representing the vertices of the planes, p_i. The solid-liquid interfacial area is the sum of all the areas of the planes which defines the interface, *i.e*, $A_{sl} = \sum_{i} A_{pi}$.

4.4.2 Solid-Vapor and Liquid-Vapor Area

To calculate the solid-vapor, A_{sv} and liquid-vapor, A_{lv}, surface areas, we consider the curved surface that is exposed. The curved surface area is taken to be

the area of curve surface of a spherical pyramid and given by

$$Area = \frac{\pi}{2} r(4h + s), \tag{4.2}$$

where r is the radius of curvature, h is the height of the spherical sector, ABC in fig. 4.5, s is the diameter of the base.

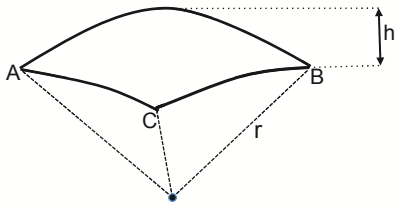

Figure 4.5: A geometric sketch the curved surface area of an atom with vertices ABC.

We take r to be the molecular radius of the atom, which has the value of $1.6\mathring{A}$ for gold. The spherical height is obtained by calculating the midpoint, m, for all the vertices, ABC, shared by other surface atoms. The distance, pm, between m and the position of the atom is calculated with the atomic position as a reference point. The height is given as $h = r - pm$.

We then make use of the three different surface areas to construct the equation relating the free energy barrier to the surface areas and surface tensions and call this model the $Sphen - 1$ model,

$$\Delta G(n) = \Delta\mu n + A_{sv}(n)\sigma_{sv} + (A_{lv}(n) - A_0)\sigma_{lv} + A_{sl}(n)\sigma_{sl}. \tag{4.3}$$

4.4.3 Three Phase Contact Line and Radius of Curvature

In order to understand the effect of line tension on the energy barrier, we calculate the length of the three phase contact line. To do this we identify the atoms sharing the three phases. A solid atom is said to be on the three phase contact line, if it is a surface atom, belonging to the maximum embryo and it shares at least one liquid-like neighbor which is also a surface atom. The distance, l_{ij}, between atoms i and j which are on the contact line is calculated and the

length of the entire line is the sum of the distances,

$$L_{slv} = \sum l_{ij}. \tag{4.4}$$

The free energy function with the effect of the line tension, τ, included is termed the $Sphen - 2$ model,

$$\Delta G(n) = \Delta\mu n + A_{sv}(n)\sigma_{sv} + A_{lv}(n) - A_0)\sigma_{lv} + A_{sl}(n)\sigma_{sl} + L_{slv}(n)\tau. \tag{4.5}$$

To understand the curvature effect using the *Sphen* models, we estimate the radius of curvature of the solid embryo. This is calculated locating the center of mass of the solid embryo, then calculating the distances of all the atoms in the embryo. The radius curvature is taken to be the average distance of the farthest solid atom from the center of mass. This is introduced in eqn. 4.3 with the Tolman lengths to give:

$$\Delta G(n) = \Delta\mu n + A_{sv}(n)\sigma_{sv}(1 - \frac{2\delta_1}{R}) + (A_{lv}(n) - A_0)\sigma_{lv}(1 - \frac{2\delta_1}{R}) + A_{sl}(n)\sigma_{sl}(1 - \frac{2\delta_2}{R}). \tag{4.6}$$

The calculation of the radius of curvature is done only for the Lennard-Jones bulk liquid and therefore eqn. 4.6 is only applied to the Lennard-Jones bulk system. It should be noted that including the curvature correction in this way implicitly assumes a spherical embryo, even though the calculation of the surface areas do not.

4.4.4 Volume and Density

To calculate the density of the largest embryo, we must calculate its volume. For each of the atoms making the maximum embryo, we calculate the volume of the voronoi cell about the atom. The volume of each convex hull is given as,

$$v = \frac{1}{3}\sum_i d_i A_i, \tag{4.7}$$

where A_i is the area of the plane i, d_i is the perpendicular distance from the center of the convex hull (i.e. the position of the atom) to the plane. Since our system is homogeneous with all the atoms having equal size, we define d_i as one half the distance between the atom and the neighbor sharing the same plane. The sum of the volumes of all the atoms of the embryo makes the volume, $V(n)$, of the whole, embryo with size n_{max}. The density of the solid phase is the ratio of the number of atoms present in the embryo to its volume,

$$\rho(n) = \frac{n}{V(n)}. \tag{4.8}$$

4.5 Results

In this section, we report the results of our geometric calculations and the results from fitting our models to the free energy barriers obtained from simulations in section 2.3. The molecular configurations used in the calculation of these parameters where obtained at different temperatures, therefore to test their sensitivity to temperature, we calculate the solid-vapor surface areas for 276 atoms cluster at $T = 660K,\ 670K,\ 690K,\ 730K$. Figs. 4.6 and 4.7 show the A_{sv} for the 276 and 456-atom cluster respectively. From the scatter of the data, we see that the surface areas are independent of temperature. Athough not shown, we see a similar temperature independence in other geometric parameters. For the rest of the calculations, we take the average over all the temperature ranges. For all the geometric factors we calculate, we take the average over all the configurations having the same maximum embyo size. These are the values that we use in the free energy function to estimate the surface free energies.

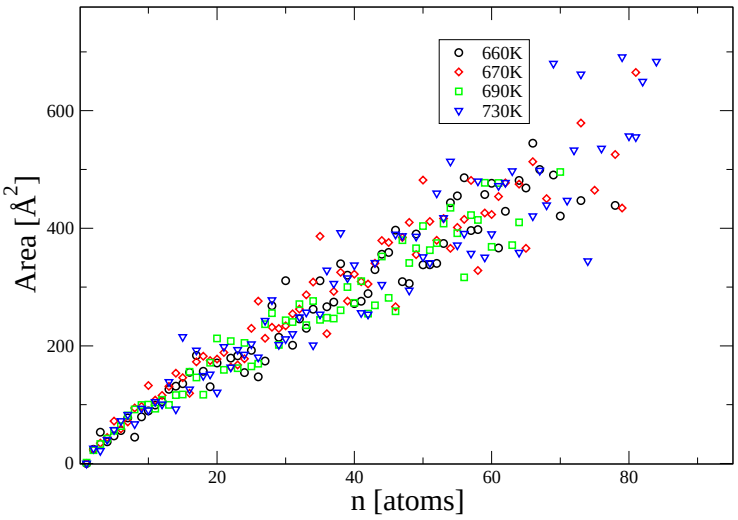

Figure 4.6: A plot of solid-vapor surface areas for different temperatures calculated for 276 atoms cluster. It shows that the surface areas are not temperature dependent.

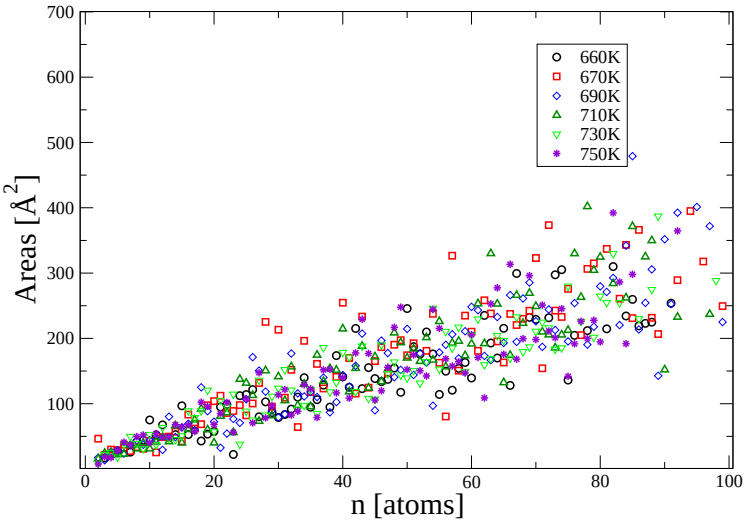

Figure 4.7: A plot of solid-vapor surface areas for different temperatures calculated for 456 atoms cluster.

4.5.1 Gold Clusters

For the two different cluster sizes of gold we are studying, we calculate the different surface and interfacial areas using the atomic positions. We perform the calculations for a total of 3216 configurations of 456 atom gold cluster and 3095 configurations of 276 atom gold cluster. The results of the calculation strongly support that that freezing in gold nanoparticles starts from the surface. Fig. 4.8(right) shows a plot of the solid-vapor surface and solid-liquid interfacial areas for 456 atoms cluster while fig. 4.8 (left) is the same plot for 276 atoms cluster. Following the phenomenological approach to nucleation, the surface term in the free energy expression is in the order of $n^{2/3}$, where n is the solid embryo size, we therefore present this surface area plots as a linear function of $n^{2/3}$. We observe that both the solid-vapor and solid-liquid areas are comparable at a smaller embryo size. As the embryo grows, the solid-liquid interfacial area grows at a faster rate than the corresponding solid-vapor surface area. This suggest that though nucleation starts at the surface, the growth is faster inward than on the solid-vapor interface.

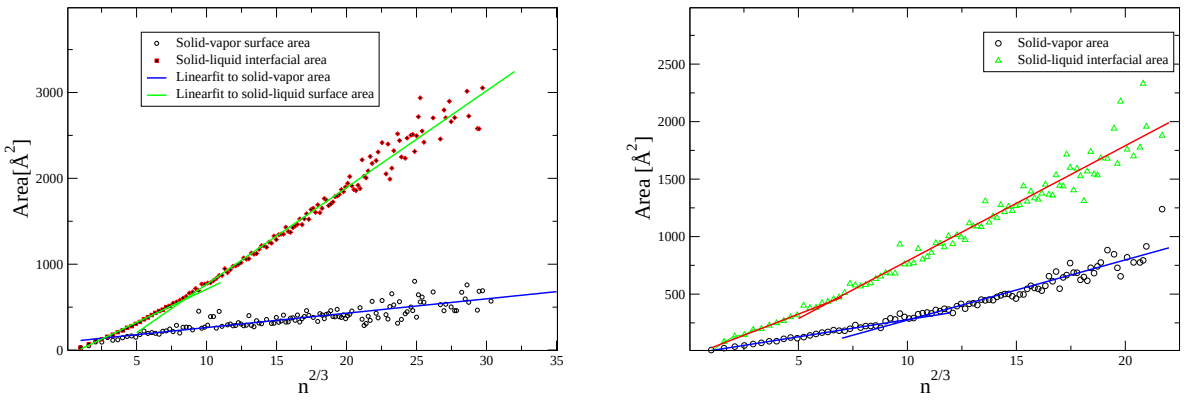

Figure 4.8: Solid-vapor and solid-liquid surface areas calculated for 456-atom cluster(left) and 276-atom cluster(right) plotted as a function of $n^{2/3}$.

Although these surface areas are linear in $n^{2/3}$, we notice a change in the slope of these linear plots at smaller embryo sizes. This change in slope seems to

suggest a change in the shape of the embryo within this region as there is no such change in the slope of the volumes (see fig. 4.9).

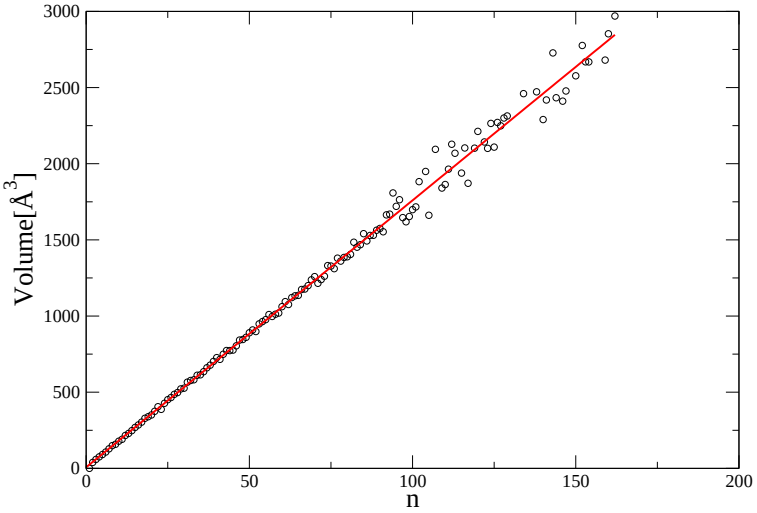

Figure 4.9: A plot of the volumes calculated for solid embryo in 456 atoms gold cluster.

For pseudo-heterogeneous nucleation, another important geometric factor is the three phase contact line. Fig. 4.10 shows that a plot of the three phase contact line for the 456-atom cluster as a function of $n^{1/3}$ is linear. This line also shows a change in the slope at small sizes. This is consistent with the slope changes observed in the surface area data.

In order to use this geometric information, we obtain a functional form of the different surface areas and the three phase contact line. Table 4.1 shows the functional expressions for the geometric coefficients for the different sizes of the clusters that we studied. Using these functional expressions for the areas in eqn. 4.3, we fit the free energy barrier to the resulting $Sphen-1$ model expression. We also fit the free energy barriers for the two cluster sizes to $Sphen-2$ model (with line tension) at various temperature. Fig. 4.11 is the plot of the free energy barrier at 710k for 456 atoms cluster showing the fit of the data to $Sphen-1$ and $Sphen-2$. The corresponding fit for 276 atom

cluster at 700K is shown in fig. 4.12.

Table 4.1: Functional forms of the geometric coefficients for gold clusters.

Geometric parameters	size =276	size =456
A_{sv}(n)	$36.63n^{2/3}$	$15.12n^{2/3}$
$A_{lv}(n)$	$1694.96 - 157.84n^{2/3}$	$2017.55 - 18.66n^{2/3}$
$A_{sl}(n)$	$85.74n^{2/3}$	$94.37n^{2/3}$
$L_{slv}(n)$	$11.68n^{1/3}$	$11.19n^{1/3}$

To compare how good our fits are, we calculate the statistical residuals for the fit of the models. Table 4.2 shows the change in chemical potential, $\Delta\mu$, solid-liquid interfacial tension, σ_{sl}, and line tension,τ obtained at different temperatures with the corresponding residuals for 456 cluster size, while table 4.3 shows the same set of data for 276-atom cluster.

Table 4.2: A table showing the fit parameters from fitting free energy barriers of 456 atoms cluster to $Sphen-1$ and $Sphen-2$ models, and the residuals as a measure of closeness to the data.

T [K]	$Sphen-1$			$Sphen-2$			
	$\Delta\mu[kT]$	$\sigma_{sl}[J/m^2]$	Res.	$\Delta\mu[kT]$	$\sigma_{sl}[J/m^2]$	$\tau \times 10^{-}11[J/m]$	Res.
650	-0.699	0.054	5.947	-0.310	0.026	3.76	0.76766
660	-0.662	0.053	5.908	-0.283	0.025	3.68	1.2106
670	-0.643	0.052	6.87	-0.199	0.021	4.31	1.1738
680	-0.609	0.051	7.14	-0.149	0.019	4.46	1.3537
690	-0.575	0.050	6.84	-0.133	0.019	4.30	1.11556
710	-0.520	0.049	6.88	-0.0789	0.017	4.33	1.067
730	-0.465	0.048	6.015	-0.077	0.02	3.77	1.0925
750	-0.444	0.048	7.28	-0.0154	0.017	4.24	1.057

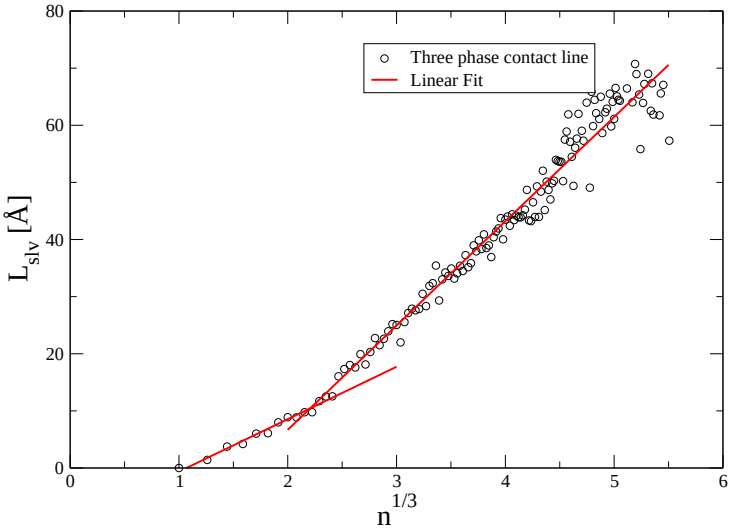

Figure 4.10: The length of the three phase contact line plotted as a function of $n^{1/3}$

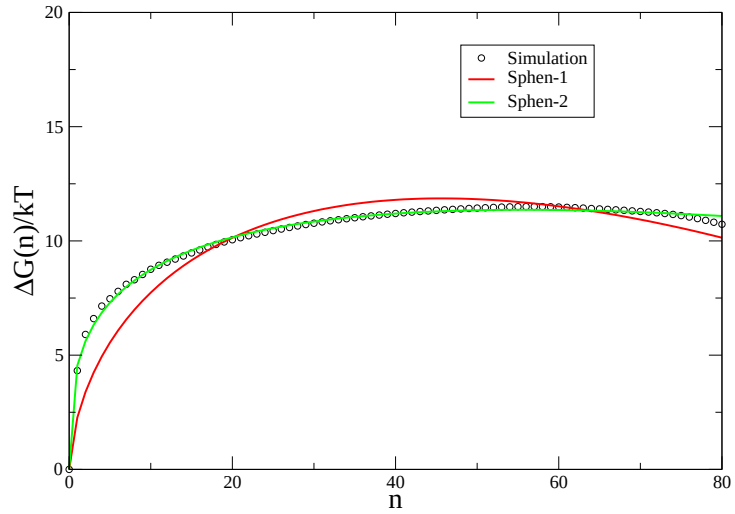

Figure 4.11: A fit of the semi-phenomenological models ($Sphen-1$ and $Sphen-2$) to simulation data at 710 K for 456 atom gold cluster.

Table 4.3: A table showing the fit parameters from fitting free energy barriers of 276 atoms cluster to $Sphen-1$ and $Sphen-2$ models, and the residuals as a measure of closeness to the data.

T [K]	$Sphen-1$			$Sphen-2$			
	$\Delta\mu[kT]$	$\sigma_{sl}[J/m^2]$	Res.	$\Delta\mu[kT]$	$\sigma_{sl}[J/m^2]$	$\tau\times10^{-}11[J/m]$	Res.
660	-0.57	0.0734	5.738	-0.190	0.044	3.64	1.061
665	-0.54	0.0725	5.900	-0.162	0.0425	3.69	1.106
670	-0.542	0.072	6.00	-0.154	0.042	3.75	1.068
680	-0.548	0.073	6.027	-0.155	0.0421	3.8	0.891
690	-0.539	0.073	6.191	-0.136	0.0416	3.89	0.785
700	-0.507	0.072	6.171	-0.052	0.0366	4.36	0.759
710	-0.505	0.072	6.023	-0.011	0.041	3.78	0.804
730	-0.470	0.071	6.0801	-0.027	0.037	4.28	0.948

In fig. 4.13, we compare the barrier heights from the fits of $Sphen-1$ and $Sphen-2$ to the barrier heights from simulation of 276 atom cluster in section 2.2 and that of 456 atoms cluster calculated by Mendez[47]. For both cluster sizes, we observe that $Sphen-2$ estimates the barrier height fairly well as can be seen in the low value of the statistical residuals and from the plots of the critical barriers, ΔG^*

Despite the relatively low values of the residuals, hence a good fit to the data, our model, $Sphen-2$, underestimates the values of the solid-liquid surface tension and our σ_{sl}'s are far lower than the value of $\sigma_{sl}=0.13-0.15$ obtained for 3943 atoms gold cluster in ref.[37] and the experimental value of $\sigma_{sl}=0.27\ J/m^2$[37]. Also, our surface tensions do not satisfy the condition for partial wetting which is a necessary condition for surface initiated nucleation[5].

Fig. 4.14 left and fig. 4.14 right show the values of the solid-liquid surface tension for the 456 and 276 atoms clusters at different temperatures. A linear fit to these values gives the temperatures dependence, $d\sigma_{sl}/dT$. For the 456-atom cluster size we have:

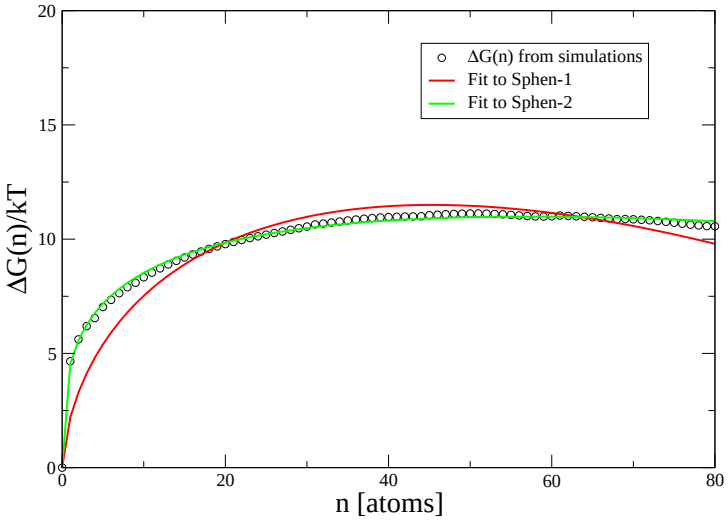

Figure 4.12: A fit of the semi-phenomenological models ($Sphen-1$ and $Sphen-2$) to simulation data at 700 K for 276 atom gold cluster.

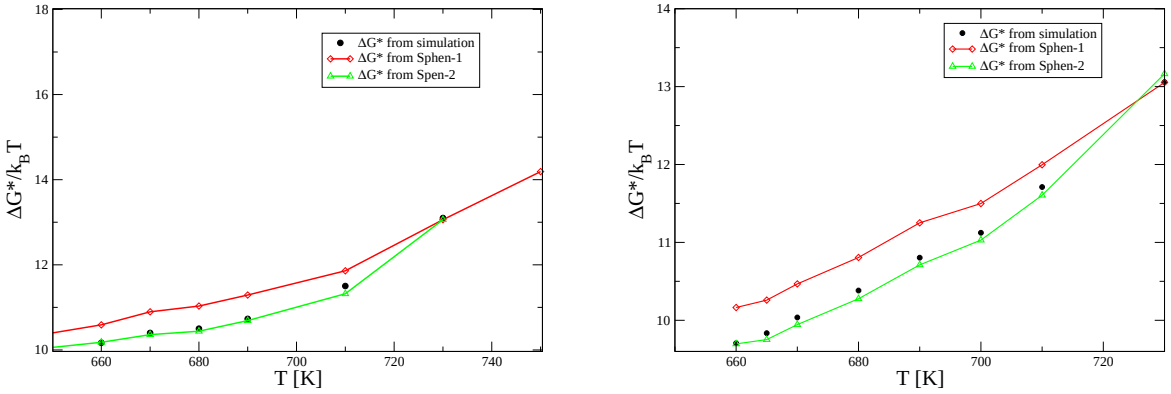

Figure 4.13: Free energy barriers for gold nanoclusters obtained from *Sphen* models. Left: Free energy barriers for 456 atom gold cluster showing the closeness $Sphen-2$ to the experimental data. Right: Free energy barrier for 276 atom gold cluster.

$$Sphen\text{-}1: \quad \frac{d\sigma_{sl}}{dT} = -6.578 \times 10^{-5}\ J/m^2.K$$

$$Sphen\text{-}2: \quad \frac{d\sigma_{sl}}{dT} = -8.026 \times 10^{-5}\ J/m^2.K$$

And for the 276-atom cluster size:

$$Sphen\text{-}1: \quad \frac{d\sigma_{sl}}{dT} = -1.46 \times 10^{-5}\ J/m^2.K$$

$$Sphen\text{-}2: \quad \frac{d\sigma_{sl}}{dT} = -8.9 \times 10^{-5}\ J/m^2.K$$

The temperature dependence, $d\sigma_{sl}/dT$, for $Sphen-2$ compare favorably for the two cluster sizes but differ by a factor of about 10 from the reported experimental value of $d\sigma_{sl}/dT = -5.1 \times 10^{-5}\ J/m^2.K$[64].

4.5.2 Lennard-Jones Bulk Liquid

In order to study bulk nucleation in Lennard-Jones fluid using our semi-phenomenological model, we calculate the solid-liquid interfacial area for solid embryo forming in a bulk liquid system of 4000 atoms at a reduced temperature of $T = 0.57, 0.58$. We study 4180 configurations obtained from Saika-Voivod *et al*[10]. Fig 4.15 shows the interfacial area as a function of the solid embryo size. The inset is a plot of the interfacial area as a function of $n^{2/3}$. This is the area we substitute in eqn. 4.3. In fig. 4.16 left, we show a plot of the volume of the solid embryo while fig. 4.16 right shows the radius of curvature calculated for each embryo size. Though the areas are obtained independent of the shape of the embryo, to calculate its radius of curvature, we make the basic capillarity assumption that the embryo is spherical. It is this radius that we use to study the finite size effect on the free energy barrier of the system.

To study the density profile as one moves from the bulk liquid to the core solid-like atoms through an interface, we calculate the density at different positions, *i.e*, in the bulk liquid, at the solid-liquid interface, and in the core solid. It is

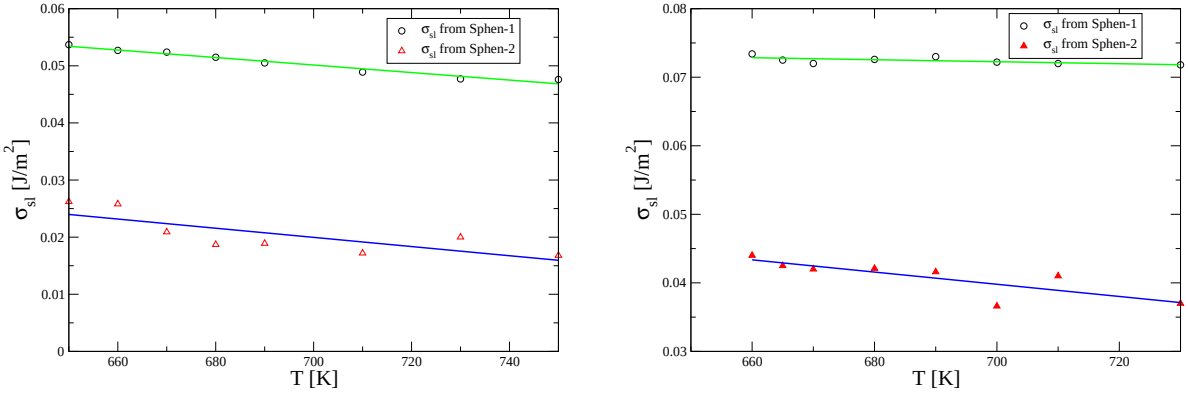

Figure 4.14: A plot of σ_{sl} as function of temperature for the two sizes studied (left:456 atoms cluster, right:276 atoms cluster).

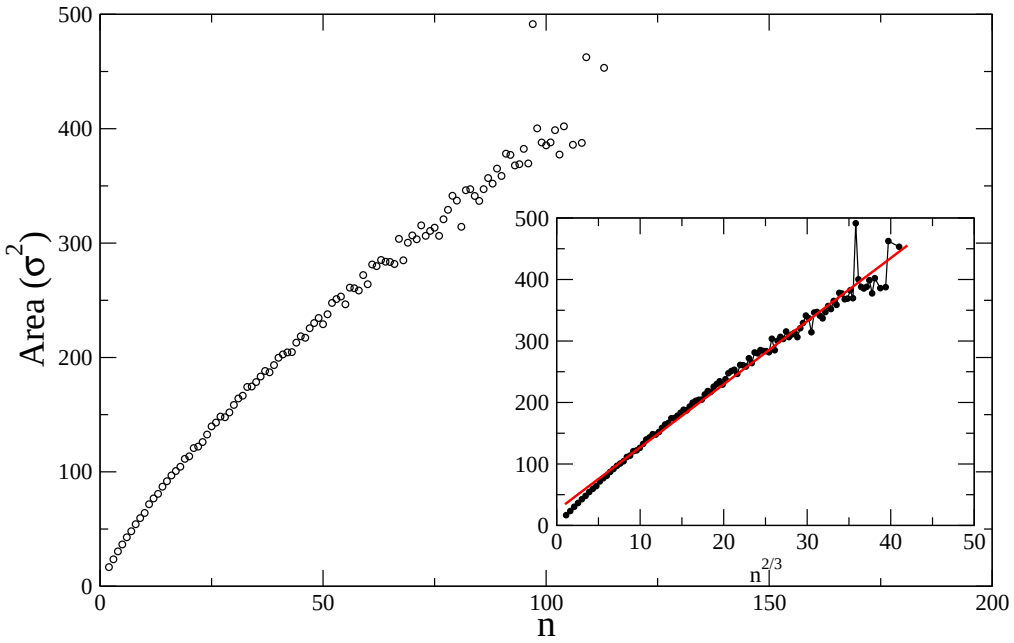

Figure 4.15: A plot of the solid-liquid interfacial area for 4000 atoms bulk Lennard-Jones liquid. Inset is a linear plot to the area.

observed that the densities of the liquid in the bulk and at the interface are different from each other and they remain fairly constant independent of the size of the solid embryo (see fig. 4.17). When compared to the density of Lennard-Jones liquid calculated at $T = 0.61\ \epsilon/kT$ by Ohnesorge *et al*[76] using density functional theory, the density of the liquid in bulk is underestimated while that at the interface is equal to number density of our system ($\rho = 0.95\ \sigma^{-1}$). The densities of the solid-like atoms depend to some degree on the size of the solid embryo. The average of the density in the core of the solid embryo compares with that obtained in ref[76], but the density of the solid at the interface is closer to that of the liquid at the interface, especially at small embryo sizes.

To use our *Sphen* model to study bulk nucleation, the model expression, eqn. 4.3, does not contain the solid-vapor and liquid-vapor surface areas, thus;

$$\Delta G(n) = \Delta\mu n + A_{sl}(n)\sigma_{sl}. \tag{4.9}$$

We then fit eqn. 4.9 to the free energy barrier obtained from Saika-Voivod *et al*[10] at two different reduced temperatures of $T = 0.57\ \epsilon/kT$ and $T = 0.58\ \epsilon/kT$. At $T = 0.58\epsilon/kT$ without any correction, we obtain $\Delta\mu = -0.56\ \epsilon$ and $\sigma_{sl} = 0.30\ \epsilon/\sigma^2$. The high value of residual (10.54) shows it is a poor fit as can also be seen in fig. 4.18.

With a first order curvature correction, the change in chemical potential, $\Delta\mu = -0.123\ \epsilon$, the solid-liquid surface free energy reduces to $\sigma_{sl} = 0.0025\ \epsilon/\sigma^2$ and $\delta = -20.0\ \sigma$ with a residual of 2.28. Introducing a second order correction to the curvature shows no significant improvement in the fit as can be seen from fig. 4.18 or the residual obtained.

Knowing that Lennard-Jones liquid undergoes bulk nucleation[9, 10] gives us the confidence to compare our model with the phenomenological model which follows from the capillarity approximation. Assuming a spherical embryo, and introducing the Tolman correction produces $\Delta\mu = -0.141\ \epsilon$, $\sigma_{sl} = 0.032\ \epsilon/\sigma^2$ and $\delta = -11.10\ \sigma$ with a residual of 2.28. Though this parameters are different from that of our *Sphen* model with correction, the residual are the same and the fit lie on each other as can be seen from fig. 4.19. This suggest that the

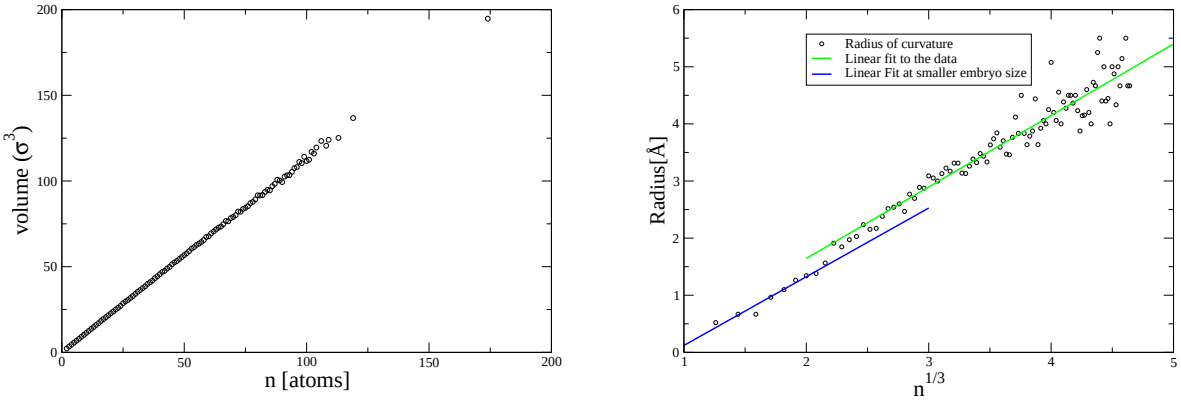

Figure 4.16: A plot of the volume of solid embryo in a Lennard-Jone bulk liquid. Right: A plot of the radius of curvature of the solid embryo.

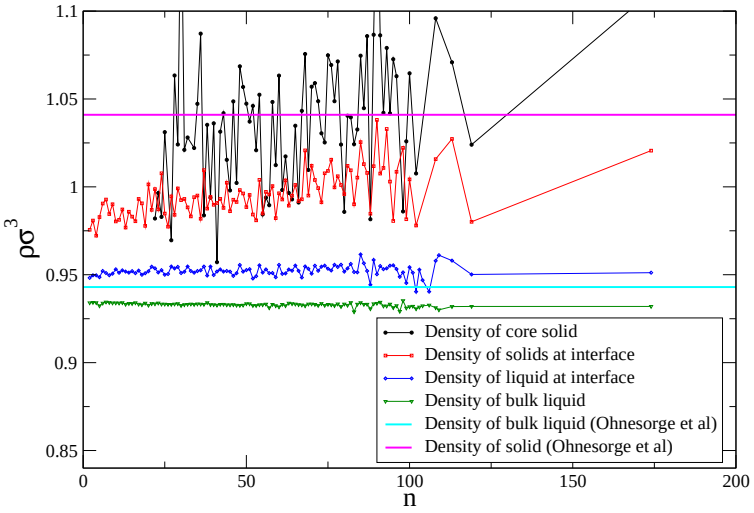

Figure 4.17: The densities of liquidlike and solidlike atoms at different locations in a bulk system plotted against the size of the solid embryo.

geometric coefficient are of different magnitudes.

Some studies[77] have suggested that the embryo may be an ellipsoid. The fit obtained using the present data under this assumption is not good, as can be seen in fig 4.19, and gives a high residual of 12.52. The curvature correction was not applied here.

4.6 Discussions

In this chapter, we take the advantage of computational geometry to divide up the space occupied by the atoms, thereby calculating the surface areas which does not depend on any geometric shape of the embryo. The independence of the geometric factors on temperature supports a previous result by Mendez[47] and also reported in ref.[7], where it was observed that the number of solid atoms in the maximum embryo which reside on the solid-vapor interface is independent of temperature. This is also supported by the distance of the solid embryo from the cluster which is independent of temperature as seen during the calculation of the $2D$ free energy surface in section 2.2.

Though surface ordering is the basic mode of freezing in gold nanopartcles[7, 37, 47], the rapid rise in the slope of the solid-liquid interfacial area plot indicate a faster growth inward rather than spreading on the solid-vapor interface. This appears to be in contradiction of some earlier studies[31] that suggested the entire surface orders first during freezing. The change in the slopes of the solid-vapor, and solid-liquid surface areas and the length of the three phase contact line can be related to the change in the number of solid-like atoms. Mendez *et al*[7] observed that, for 456 atoms cluster a higher percentage of solid-like atoms in the maximum embryo size was on the solid-vapor interface for smaller embryo size *i.e.* $n < 20$ appearing on the surface. For this which we also observe for 276-atom cluster, we strongly suggest that the is a change in the shape of the embryo around $n = 20$.

To test the accuracy of our area calculations, we calculate the surface area of the entire 276 cluster and compare it to the surface area of same size assuming

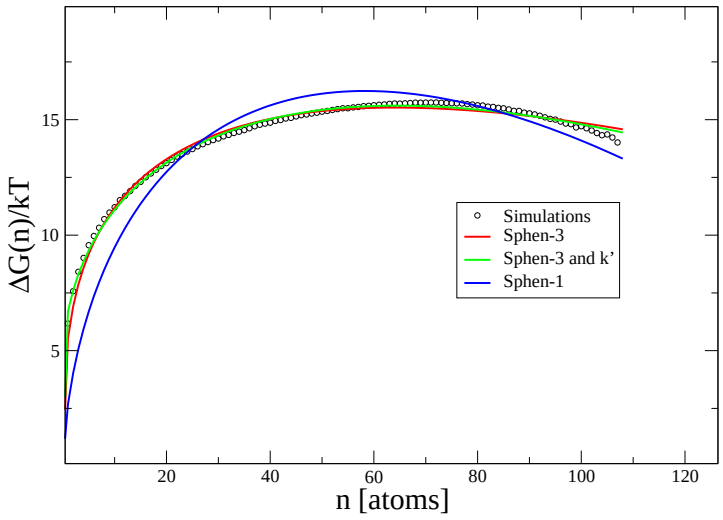

Figure 4.18: A fit of free energy data at $T = 0.58$ to *Sphen* model for Lennard-Jones bulk liquid showing the effect of different correction.

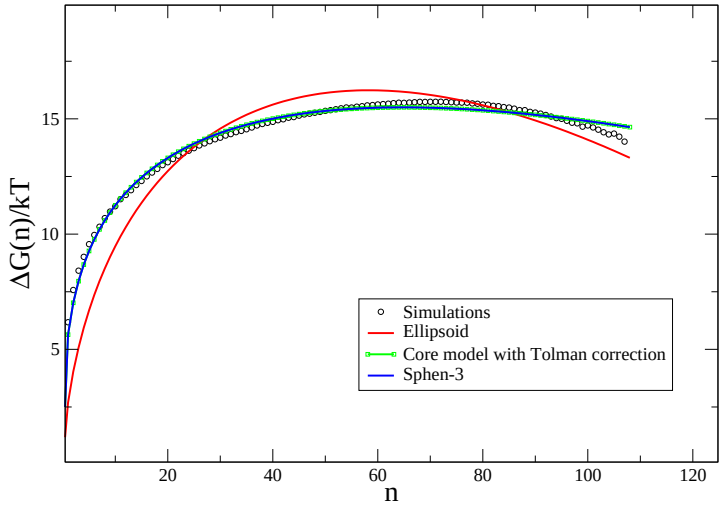

Figure 4.19: Comparison of the fit of the free energy at $T = 0.58$ to our $Sphen - 3$, core and ellipsoid models.

a spherical shape. Our method is within 3.8% error which gives a fair hope of estimating an appropriate solid-liquid surface free energy density from our model. But the values of σ_{sl} we obtain are significantly below the value which satisfy the condition of partial wetting or values reported in the literature[37]. In our calculations, we did not account for the curvature correction for the σ_{sv} and σ_{lv}. This was done to avoid the assumption of a spherical embryo, and may have resulted in the low values of the σ_{sl}. The values of σ_{sl} have been documented in very few places in literature, hence we do not have broad comparison. Also, there is the need to calculate σ_{sv}, σ_{lv} and σ_{sl} for gold nanocluster directly.

The density profile for the Lennard-Jones bulk liquid shows the density fluctuation as one moves across the liquid-solid interface. The density of the particles in the bulk liquid which we obtained for $T = 0.58\ \epsilon/kT$ is 1.6% off the density of the whole system ($\rho = 0.95\ \sigma^{-1}$) and $< 1\%$ different from the calculated in ref.[76]. The difference between the liquid density in the bulk and at the interface suggest that the interface is diffuse contrary to the sharp interface assumed while invoking the capillarity approximations. This can also be seen from the density of the solid-like particle at the interface. Though with a high fluctuation in the values, the density of the solid-like particles inside the embryo seems to depend on the embryo size. The unavailability of a core solid-like particle at embryo size less that 25 points to the fractal nature of the embryo. At larger embryo size, the core solid-like particles are rare leading to the poor statistics observed for the solid-like density which supports the idea of fractal irregular embryo.

Accounting for the curvature of the interface produced a better fit (cf. fig. 4.18) with a low residual. Our radius of curvature goes as $n^{1/3}$ and therefore has a correcting effect especially at small embryo size. This has the same effect as the curvature term used in ref.[10], though they did not explicitly measure the Tolman length. When compared to the coefficients obtained in ref[10] by fitting the $n^{2/3}$ and $n^{1/3}$ terms directly to the free energy barriers, our σ_{sl} and δ reproduced the same values. This points to the importance of the curvature correction. Compared to the values when a spherical shape is assumed for the

embryo, we obtained the same values of the residual and both fits lie on each other (cf. fig. 4.19), but the fit parameters are different. This suggest that the embryo is not spherical as the geometrical coefficient is not the same for the spherical shape.

Chapter 5

Discussions and Conclusions

5.1 Discussions

In this thesis, we aim to understand the contributions of various surface phenomena, such as surface tension, line tension, contact angle and radius of curvature, on the free energy barrier to freezing in nanoparticles. We do this in three ways: First, by calculating the free energy of forming an $n - sized$ embryo in a gold nano-cluster using molecular simulation. We then develop three phenomenological models that allow for the possibility of solid nucleation occurring at the liquid-vapor interface. Within each of these models, we are able to introduce the various correction terms that account for the different surface phenomena. Finally, we introduce the idea of a semi-phenomenological model that uses computational geometry to obtain the necessary geometric parameters required in a phenomenological model.

In our molecular free energy calculation for a 276-atom gold cluster, it is noticed that 76% of the solid-like atoms in the largest embryo sit on the solid-vapor interface for $n_{max} < 11$ and about 60% for $n_{max} > 11$. This is an increase in the number of solid-like atoms on the surface from what was observed in larger (456 atoms) system[7, 47]. This supports the earlier findings[7, 31, 47] that nucleation occurs at the surface for gold nanoparticles. Though freezing starts at the surface, the embryo grows inwards, along the solid-liquid interface, as observed in the rapid increase of the solid-liquid interfacial areas. The free energy surface as a function of size and distance, d, sheds more light on the phenomenon of surface nucleation. It supports our findings of inward growth of the embryo after the freezing is initiated at the surafce. This is seen in the

decrease of the distance, d, between the center of mass of the embryo and that of the whole cluster as the size of the embryo increases. Furthermore, our geomety studies show that the solid-liquid surface area grows faster as a function of n than the solid-vapor surafce area.

The first of our phenomenological models was the spherical cap model, which represented the solid embryo as a spherical cap region of a spherical liquid drop. The solid-vapor interface is the spherical part of the cap and the solid-liquid interface is the flat base of the cap. While the *Scap* model, with its corrected versions, fit to the data well, the resulting parameters were unphysical. The major constraint on this model is the assumption of a flat solid-liquid interface. This assumption results in a higher solid-vapor surface area than solid-liquid interfacial area for all sizes, which is inconsistent with our computational geometry studies. However, for systems which may allow for a higher solid-vapor surface area, the *Scap* model could be a useful model in studying surface nucleation.

The modified spherical cap model has many of the same basic assumptions of the *Scap* model except the solid-liquid interface becomes curved and gives rise to the *Mscap* model with a characteristic contact angle. The thermodynamic contact angle, which is independent of embryo size, is a major measure of the wettability of the embryo by the liquid phase. This is observed in the plot of α as a function of σ_{sl} (cf. fig. 3.12), where for $\sigma_{sl} \leq 0.16\ J/m^2$, $\alpha = \pi$ which denotes total wetting for this model. When $\sigma_{sl} > 0.16\ J/m^2$, there is partial wetting as $0 < \alpha < \pi$. This strongly agrees with the partial wetting condition[5, 61] which is a prerequisite for surface induced nucleation. The mechanical equilibrium, using the balance of the different surface tensions, produces the same result, showing the suitability of *Mscap* model to predict the wetting conditions.

The sign of the equilibrium line tension, τ, has been reported as both positive and negative[60, 63]. Using the *Mscap* model, we were able to explore the consequences of both positive and negative line tensions. A line tension leads to a size dependent contact angle. A positive line tension leads to an increase in α, corresponding to a convex solid-liquid interface. This produces a larger solid-

liquid interfacial area when compared to solid-vapor surface area. A negative line tension which makes the contact angle smaller, than the equilibrium contact angle causes the solid-liquid interface to be concave for small embryo sizes. For the *Mscap* model, the solid-liquid interface is approximately equal to the solid-vapor surface area at about $n \leq 5$ where solid-liquid interface is concave. At $n > 5$, we see a rapid rise in solid-liquid interfacial area, which is also observed in our molecular calculation.

The qualitative studies using the *Mscap* models have provided considerable insight to the effect of different surface phenomena on freeing in a nanoparticle system exhibiting surface nucleation. However, we were unable to obtain numerical fits of the models to the simulation data due to the technical difficulties of developing a fitting scheme.

The sphere to sphere model captures the intuition that the evolving solid embryo will always appear on the surface of the cluster at a distance, d, from the center of the entire cluster. This has the advantage of being able to exhibit total wetting, partial wetting and nonwetting conditions. In the partial wetting case, the $2D$ free energy surface show the position with the highest probability of locating an $n - sized$ embryo corresponds to a "channel" on the free energy surface. Qualitatively, the sphere to sphere model is consistent with the $2D$ free energy surface obtained from simulations for the 456-atom gold cluster. Also, the fit obtained for data at $T = 650\ K$ compares well with the data especially along the minima with the σ_{sl} being very close to the value expected for the partial wetting in gold nanocluster. But on either sides of the "channel", the fit is not good, likely due to poor statistics in this region during the free energy calculations.

Using a molecular approach to obtain the surface areas and other geometric coefficients appearing in the free energy expression helps in the understanding of the growth of the embryo compared to the different phenomenological models. Although we have not explicitly examined the shape of the embryo in our molecular calculations, our results strongly suggest that there is a change in the shape of the embryo. This is due to the change in the slopes of the solid-liquid

surface area, the solid-vapor surface area and the length of three phase contact line as a function of n at an embryo size of approximately $n = 11$. There is no corresponding change in the slope of the volume. The changes in the slope of these geometric coefficients are also observed in our theoretical studies of $Mscap$ model when the line tension is introduced. The changes in the slopes observed in our $Sphen$ calculations are similar to the case of negative line tension in $Mscap$ model. This may point to the presence of a concave solid-liquid interface at small embryo sizes. However, we note that the concave embryo results from a negative line tension in the $Mscap$ model, while fitting the $Sphen - 2$ model produces a positive line tension. We expect a numerical fit of $Mscap$ model to provide a quantitative proof or comparison with the $Sphen$ model. Irrespective of the sign of the line tension, it has a major effect in the free energy barrier for systems undergoing surface nucleation.

Despite the ability of the molecular calculations to help us understand the growth of the embryo, the fits from resulting $Sphen$ model appear to underestimate the σ_{sl} expected for gold under the partial wetting regime, with the given bulk σ_{sv} and σ_{lv}. All our fits rely on the values of the σ_{sv} and σ_{lv} which were obtained for bulk at the bulk melting point[52]. The finite size correction could not be applied to this model without assuming a spherical embryo, therefore, these bulk values were used directly. Further, we would expect the σ_{sl} value obtained by from nanoclusters to be smaller than the bulk because of curvature corrections. Also, the temperature dependence of these bulk surface tensions is not known[52]. Reiss *et al*[5] suggested that the reason why the σ_{sl} obtained from fitting models to simulation data cannot be used to test the partial wetting inequality is the unreliable values of σ_{sv} and σ_{lv} which is always obtained from Young's equation while assuming complete wetting. Also, σ_{sl} obtained by fitting is an average over all facets of the crystal, whereas the inequality in expression 1.46 was derived for different facets of the crystal.

For a solid embryo, the atoms in the bulk and the surface belong to different environment. The bulk atoms can be considered as applying a form of stress on the surface or the interface. The importance of the surface stress in evaluating

the surface free energy has been noted by Shuttleworth[78] especially for faceted systems. Accounting for the the contribution of the surface stress rather than surface tension alone may be help improve our models.

A comparison of the fit for $Sphen-3$ model to free energy barriers for bulk Lennard-Jones with that of the phenomenological model (assuming spherical embryo), shows the two fits lie on each other and produce the same residual, but the fit parameters obtained are different for each of them. This strongly suggest that the geometric coefficients (solid-liquid area and radius of curvature) are different. This suggests the embryo may not be spherical.

5.2 Conclusions

Phenomenological models and a semi-empirical approach are used to study the different effects of surface phenomena on the nucleation barriers to nucleation. The $2D$ free energy calculation for gold nanocluster show that although freezing is initiated at the surface, the growth is inward and this is confirmed by our molecular calculations.

We propose different phenomenological models which help in the understanding of surface nucleation. The $Mscap$ model shows a nontrivial contribution of the line tension and contact angle to the nucleation barrier and how the contact angle can be used as a measure of wettability. The semi-phenomenological calculations show the structural changes taking place in the embryo as it grows. It also gives an accurate method of obtaining the geometric coefficients used in the free energy expression independent of any formal geometry. Although bulk nucleation is favorable in the case of Lennard-Jones liquid, our semi-phenomenological approach is able to prove that the evolving embryo is not spherical.

Future work will seek to obtain the solid-liquid surface tension from our $Mscap$ model in addition to calculating solid-vapor and liquid-vapor surface tensions. The change in shape as nuclei in gold nanoparticles grow will also be studied. A more detailed study will help in the understanding of the actual shape of

embryo during the freezing of Lennard-Jones.

Bibliography

[1] A. Laaksonen, V. Talanquer and D.W. Oxtoby , *Annu. Rev. Phys. Chem.* **46**, 489 (1995)

[2] D. W. Oxtoby, *J. Phys.: Condens Matter,* **4**, 7627,(1992)

[3] D. Reguara, R. K. Bowles, Y. Djikaev , and H. Reiss, *JCP* **118**,1,(2003)

[4] Y.S. Djikaev, A. Tabazadeh, P. Hamil and H. J. Reiss. *Phys. Chem. A* **106**, 10238 (2002)

[5] Y.S. Djikaev, A. Tabazadeh, P. Hamil and H. J. Reiss. *Phys. Chem. A* **106**,10253(2002)

[6] H-S Nam, N. M Hwang, B. D. Yu, D.-Y Kim and J.-K Yoon, *Phys. Rev. Lett*, **89**, 2755021 (2002)

[7] E. Mendez-Villuendas and R. K. Bowles, *Phys. Rev. Lett.*,**98**,185505 (2007)

[8] G. W. Turner and L. S. Bartell, *J. Phys. Chem. A*, **109** , 6877 (2005)

[9] M.Sekine, K. Yasuoka, T. Kinjo, and M. Matsumoto, *Fluid Dynamics Res.*, **40**, 597 (2008)

[10] S. E. M Lundrigan and I. Saika-Voivod, textitJ. Chem. Phys., **131**, 104503 (2009)

[11] P. G. Debenedetti, *Metastable Liquids*, Princeton University Press, Printon (1996)

[12] M. Berveiller, and F . D.Fischer, *Mechanics of Solids with Phase Changes*, Springer Wien, New York (1997)

[13] L. D. Landau and E. M. Lifshitz, *Statistical Physics Part 1,*, Pergamon, 3rd Ed. (1994)

[14] J. W. Gibbs, *The Collected Works of J. W. Gibbs*, New Haven, Yale University Press, (1957)

[15] P. G. Debenedetti and H. Reiss, *J. Chem. Phys.*, **108** 13 (1998)

[16] A. Laaksonen, R. McGraw, and H. Vehkamaki, *J. Chem. Phys*, **111**, 2019 (1999)

[17] G. Wulff,*Z. Kristallogr. Min.*, **34**, 449 (1901)

[18] T. Zykova-Timan, C. Valeriani , E. Sanz , D. Frenkel , and E. Tosatti, *Phys. Rev. Lett.* **100**, 036103 (2008)

[19] H. Reiss and R. K. Bowles, *J. Chem. Phys.*, **111**, 7501 (1999)

[20] G. K. Schenter, S. M. Kathmann, and B. C. Garrett, *Phys. Rev. Lett.*, **82** (1999)

[21] T. L. Hill,*J. Chem. Phys.*, **23**, 617 (1955)

[22] J. K. Lee, J. A. Barker and F. F. Abraham, *J. Chem. Phys.*, **61**, 1221 (1974)

[23] F. H. Stillinger, *J. Chem. Phys.*, **38**, 1486 (1963)

[24] P. J. Steinhardt, D. R. Nelson, and M. Ronchetti, *Phys. Rev, Lett. B*, **28**, 784 (1983)

[25] S. Auer and D. Frenkel, *J. Chem. Phys*, **120**,3015 (2004)

[26] S. Auer and D. Frenkel, *Nature*, **409**, 1020 (2001)

[27] P.R. ten Wolde and D. J. Frenkel, *J. Chem. Phys.*, **109**, 9919 (1998)

[28] D. R. Lopez, *Mesoscopic Nonequilibrium Kinetics Nucleation Processes*, PhD thesis

[29] Y. S. Djikaev and E. Ruckenstain, *J. Phys. Chem. B*, **124**, 194709 (2007)

[30] R. E. Lee, G. J. Warren, and L. V. Gusta, *Biological Ice Nucleation and Its Applications*, APS Press (1995)

[31] H-S Nam, N. M Hwang, B. D. Yu, D.-Y Kim and J.-K Yoon, *Phys. Rev. B*, **71**, 2334001 (2005)

[32] J. G. Allpress and J. V. Sanders, *Surf. Sci* **7**, 1 (1967)

[33] P.A Buffat, M. Flueli, R Spycher, P.Stadelmann and J-P Borel, *Faraday Discuss.* **92**, 173 (1991)

[34] L. D. Marks, *Rep. Prog. Phys.*, **57**, 603 (1994)

[35] C. L. Cleveland, U. Landman, T. G. Schaaff, M. N. Shafigullin, P. W. Stephens, and R. L Whetten, *Phys. Rev. Lett.*, **79**, 1873 (1997)

[36] S. C. Hendy and J. P. K. Doye, *Phys. Rev. B*, **66**235402 (2002)

[37] Y. Chushak and L.S. Bartell, *J. Phys. Chem. A*, **104**, 9328 (2000)

[38] S. Iijima and T. Ichihashi, *Phys. Rev. Lett*, **56**, 616 (1986)

[39] G. A. Merry and H. Reiss, *Acta. Metall*,**32**, 1447 (1984)

[40] A. C. Pan, T. J. Rappl, D. Chandler and N. P Balsara, *J. Phys. Chem. B*, **110**, (2006)

[41] N. Metropolis, A.W. Rosenbluth, M. N. Rosenbluth, A. H. Teller and E. Teller, *J. Chem. Phys.*, **21**, 1087 (1953)

[42] G. M. Torrie and J. P. Valleau, *J. Comput. Phys*, **23** (1977)

[43] D. Frenkel and B. Smit,*Understanding Molecular Simulations: From Algorithms to Applications*, Academic Press (2002)

[44] M. Falcioni and M. W. Deem, *J. Chem. Phys.*, **110**, 1754 (1999)

[45] J. E. Jones and A. E. Ingham, *Proc. R. Soc. A*, **107**, 686 (1925)

[46] M. S. Daw, S. M. Foiles, and M. I. Baskes, *Mat. Sci. Rep.*, **9**, 251 (1993)

[47] Mendez, E. (2007). *Nucleation in Gold Nanoclusters*. Unpublished Master's Thesis, University of Saskatchewan, Saskatoon, Saskatchewan, Canada.

[48] Stanford Encyclopedia of Philosophy, http://plato.stanford.edu/entries/models-science/, accessed on 09/08/2009

[49] E. McMullin, *Logic, Methodology and Science III*, edited by B. van Rootselaar and J. F. Staal, (Amsterdam : North Holland,1968) 385-396

[50] D. Schebarchov and S. C. Hendy, *Phys. Rev. Lett.*,**96**, 256101 (2006)

[51] S. C. Hendy,*Nanotechnology*,**18**,175703 (2007)

[52] L. J. Lewis, P. Jensen and J. L. Barrat, *Phys. Rev. B*, **56** 2248 (1997)

[53] M. P. A. Fisher and M. Wotis, *Phys. Rev. B*,**29**, 11(1984)

[54] T. Young, *Phil. Trans.*, **95** (1805)

[55] Q. Xu, I. D. Sharp, C. W. Yuan, D. O. Yi, C. Y. Liao, A. M. Glaeser, A. M. Minor, J. W. Beeman, M. C. Ridgway, P. Kluth, J. W. Ager III, D. C. Chrzan, and E. E. Haller, *Phys Rev. Lett.* **97**, 155701 (2006)

[56] F. Caupin, *Physical Review B*, **77**, 184108 (2008)

[57] C .L. Cleveland, U. Landman, and W. D. Luedtke, *J. Phys. Chem.*, **98** (1994)

[58] P. Seppecher, *Oil & Gas and Tech.* **56**, 77 (2001)

[59] J. D. Pinter, *J. Glob. Optim*, **38**, 79 (2007)

[60] X. F. Yang, *Appl. Phys. Lett.*,**67**, 2249 (1995)

[61] R. E. Johnson, and R. H Dettre, *in Surface and Colloid Science*, edited by E. Matijevic (Wiley- Interscience, New York, 1969) Vol. 2

[62] P. Letellier, A. Mayaffre, and M. Turmine, *J. Coloid Interface Sci.*, **314**, (2007)

[63] L. Schimmele, M. Napiorkowski, and S. Dietrich, *J. Chem. Phys*, **127**, 164715 (2007)

[64] S. Iarlori, P. Carnevali, F. Ercolessi, and E. Tosatti, *Surf. Sc.*, **211-212** (1989)

[65] J. Ryu, D. Kim, Y. Cho, R. Pam and D. S. Kim, *Comput. Aided Design and Appl.*,**2** (2005)

[66] N. R. Voss and M. Gerstein, *J. Mol. Biol.*, **346** (2005)

[67] F. M. Richards,*J. Mol. Biol.*, **82**, 1 (1974)

[68] I. Stankori, M. Kroger, and S. Hess, Comput. Phys. Comm., **145** (2002)

[69] L. J. M. Jacobs, K.C.H Danem, M. F. Kemmere and J. T. F Keurenjes, *Comput. Mat. Science*,**38** (2007)

[70] D. Kim, C. H. Cho, Y. Cho, J. Ryu, J. Bhak and D-S Kim, *J. Mol. Graphics and Modelling*,**26** (2008)

[71] Y. Wang, S. Teitel and C. Dellago, *J. Chem. Phys*, **122**, 214722(2005)

[72] Okabe A, Boots B, Sugihara K, and Chiu S.N *Spatial Tessellations: Concepts and Applications of Voronoi Diagrams* John Wiley and Sons Ltd (2000)

[73] J. C. Gil Montoro and J. L. F Abascal, *J. Phys. Chem*,**97**, 4211 (1993)

[74] M. P. Allen and D. J. Tildesley, *Computer Simulations of Liquids*, Oxford Science, UK (1990)

[75] D. C. Rapaport *The Art of Molecular Dynamics Simulation* Cambridge-University Press (2004)

[76] R. Ohnesorge, H. Lowen, and H. Wagner, *Phys. Rev. E*, **50**, 4801 (1994)

[77] A. C. Pan and D. Chandler, *J. Phys. Chem. B*, **108**, 19681 (2004)

[78] R. Shuttleworth, *Proc. Phys. Soc.*, **63**, 444 (1950)

Appendix A

Generating Voronoi Vertex

The plane between a chosen particle i and its neighbor j is obtained by constructing an equation of a plane using a given point and a normal to that required plane. The following steps are taken:

– Locate the midpoint $\mathbf{M}_{ij}$ between i and j such that

$$\begin{aligned} \mathbf{M}_{ij} &= \left(\frac{x_i + x_j}{2}, \frac{y_i + y_j}{2}, \frac{z_i + z_j}{2}\right) \\ &= (x_{ij}, y_{ij}, z_{ij}) \end{aligned} \tag{A.1}$$

– The vector $\vec{\mathbf{D}}_{ij}$ between i and j and perpendicular to the desired plane is by

$$\begin{aligned} \vec{\mathbf{D}}_{ij} &= (x_i - x_j)\mathbf{i} + (y_i - y_j)\mathbf{j} + (z_i - z_j)\mathbf{k} \\ &= A_{ij}\mathbf{i} + B_{ij}\mathbf{j} + C_{ij}\mathbf{k} \end{aligned} \tag{A.2}$$

– The plane p_{ij} is given by the equation

$$p_{ij} = A_{ij}(x - x_{ij}) + B_{ij}(y - y_{ij}) + C_{ij}(z - z_{ij}) \tag{A.3}$$

For a Voronoi vertex to be formed, exactly three planes must intersect at a point, and the point of intersection becomes the Voronoi vertex.

Fig. A.1 shows a simplified 2D form of the Voronoi tessellation used in this work. $\mathbf{M}_{ij}$ is the midpoint while $\mathbf{D}_{ij}$ is the normal vector to the planes.

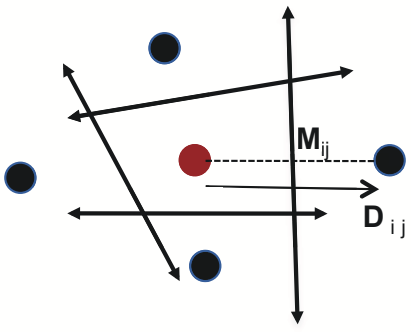

Figure A.1: Schematic diagram showing how a plane is constructed between two neighboring particles using the midpoint between them and the normal to the plane.

If three planes are represented by triple point, $p_{ij} = (X_{ij}, Y_{ij}, Z_{ij})$, where $j = 1, 2, 3$, the the point of intersection (*i.e* Voronoi vertex) is obatained by simultaneously solving the three equations arising from the fact each of the planes is coplanar with the point (x,y,z). Using Cramer's rule we have

$$\begin{vmatrix} x & y & z & 1 \\ X_{i1} & Y_{i1} & Z_{i1} & 1 \\ X_{i2} & Y_{i2} & Z_{i2} & 1 \\ X_{i3} & Y_{i3} & Z_{i3} & 1 \end{vmatrix} = 0.$$

The vertices are thus obtained as

$$x = \frac{det_x}{Det}; \qquad y = \frac{det_y}{Det}; \qquad z = \frac{det_z}{Det}, \tag{A.4}$$

where

$$\det_x = \begin{vmatrix} Y_{i2} & Z_{i2} \\ Y_{i3} & Z_{i3} \end{vmatrix},$$

$$\det_y = \begin{vmatrix} X_{i2} & Z_{i2} \\ X_{i3} & Z_{i3} \end{vmatrix},$$

$$\det_z = \begin{vmatrix} X_{i2} & Y_{i2} \\ X_{i3} & Y_{i3} \end{vmatrix},$$

and

$$\text{Det}= \begin{vmatrix} X_{i1} & Y_{i1} & Z_{i1} \\ X_{i2} & Y_{i2} & Z_{i2} \\ X_{i3} & Y_{i3} & Z_{i3} \end{vmatrix}.$$

Appendix B

Detailed Balance

The general approach used to validate the a MC algorithm under the principle of detailed balancing is outlined as follows:

- A distribution function, π, which depends on the thermodynamic constants of the system is defined.
- The detailed balance condition is invoked. This condition states that the probability of a system to evolve from an initial state, $q = o$, to a final state, $q = n$, must be equal to that from similar system evolving from state n to state o.

$$\Phi(o \to n) = \Phi(n \to o), \tag{B.1}$$

  when Φ is the flow of configuration o to n given by the products of the probability $\pi(o)$ to be in a given configuration o. Given the probability α of generating the configuration n, and $acc(o \to n)$ as the probability of accepting the move, the

$$\Phi(o \to n) = \pi(o) \times \alpha(o \to n) \times acc(on). \tag{B.2}$$

- The probabilities of generating a configuration is determined.
- The acceptance rule condition is evaluated until optimal statistics are accumulated. From a canonical ensemble, the distribution function is given by,

$$\pi(\mathbf{r}^N) = \frac{\exp\left[-\beta U(\mathbf{r}^N)\right]}{\int \exp\left[-\beta U(\mathbf{r}^N)\right] d\mathbf{r}^N}. \tag{B.3}$$

  The probability of generating a particular configuration should b independent of the conformation of the system, hence, by applying the detailed equilibrium condition, we have:

$$\alpha(o \to n) = \alpha(n \to o) = \alpha. \tag{B.4}$$

  Substituting eqn. B.4 into eqn. B.1 and also eqn. B.3 into eqn. B.2 yields the acceptance rule condition for NVT ensemble introduced in section 2.2:

$$\frac{acc(o \to n)}{acc(n \to o)} = \exp\left\{-\beta\left[U(n) - U(o)\right]\right\}. \tag{B.5}$$

The detail balance condition implies that enough sampling steps must be carried out once there is an interchange of two configurations equilibrated at different thermodynamic conditions. This is to ensure that the embryo is sampled under equilibrium condition.

The umbrella sampling combined with parallel tempering scheme used in our calculation consists of 64 nodes, each with its umbrella center and temperature, and an associated partition function is given by

$$Q_C = \prod_{\mu=1}^{8} \prod_{\nu=1}^{8} Q_{N,V,T_\mu} U(\mu, \nu). \tag{B.6}$$

Let us denote the configuration of node i by$\mathbf{i} = \mathbf{r}_i^N$, and its associated constrained potential by $U_{(i)} = U_{(i)o} + \phi_i$, where $U_{(i)o}$ is the unconstrained potential and ϕ_i is the bias potential having a Boltzmann parameter $\beta_i = \frac{1}{k_B T_i}$.

The acceptance rule fora swap between ensembles i, and j, follows from the condition of detailed balance and is given by the expression;

$$\begin{aligned} \pi(i,\beta_i)\pi(j,\beta_j) &\times \alpha\left[(\mathbf{i},\beta_i),(\mathbf{j},\beta_j)\rightarrow(\mathbf{j},\beta_i),(\mathbf{i},\beta_j)\right] \\ &\times acc\left[((\mathbf{i},\beta_i),(\mathbf{j},\beta_j)\rightarrow(\mathbf{j},\beta_i),(\mathbf{i},\beta_j)\right] \\ = \pi(i,\beta_j)\pi(j,\beta_i) &\times \alpha\left[(\mathbf{i},\beta_j),(\mathbf{j},\beta_i)\rightarrow(\mathbf{i},\beta_i),(\mathbf{j},\beta_j)\right] \\ &\times acc\left[((\mathbf{i},\beta_j),(\mathbf{j},\beta_i)\rightarrow(\mathbf{i},\beta_i),(\mathbf{j},\beta_j)\right] \end{aligned} \tag{B.7}$$

If the simulations are performed in such a way that the probability of swapping umbrella centers and temperatures occurs witha probability α, we obtain an acceptance rule:

$$\frac{acc\left[((\mathbf{i},\beta_i),(\mathbf{j},\beta_j)\rightarrow(\mathbf{j},\beta_i),(\mathbf{i},\beta_j)\right]}{acc\left[((\mathbf{i},\beta_j),(\mathbf{j},\beta_i)\rightarrow(\mathbf{i},\beta_i),(\mathbf{j},\beta_j)\right]} \tag{B.8}$$

$$= \frac{\left[-\beta_i U(j)-\beta_j U(i)\right]}{\left[-\beta_j U(j)-\beta_i U(i)\right]}$$

$$= \exp\left\{(\beta_i-\beta_j)\left[U_{(i)}-U_{(j)}\right]\right\}. \tag{B.9}$$

The rates of exchange of umbrella centers and temperatures are not the same in the course of the simulations, we set different rules for swapping umbrella centers (umbrella sampling) and for exchanging temperatures (parallel tempering).